The Magnetized Steel and Scintillator Calorimeters of the MINOS Experiment

Citation

Michael, D.G., P. Adamson, T. Alexopoulos, W.W.M. Allison, G.J. Alner, K. Anderson, C. Andreopoulos et al. 2008. The magnetized steel and scintillator calorimeters of the MINOS experiment. Nuclear Instruments and Methods in Physics Research Section A: Accelerators, Spectrometers, Detectors and Associated Equipment 596(2): 190-228.

Published Version

Permanent link

http://nrs.harvard.edu/urn-3:HUL.InstRepos:2350494

Terms of Use

Share Your Story

Accessibility

The magnetized steel and scintillator calorimeters of the MINOS experiment

The MINOS Collaboration

D.G. Michael [e,3], P. Adamson [k,u,ad], T. Alexopoulos [ak,4],
W.W.M. Allison [x], G.J. Alner [z], K. Anderson [k], C. Andreopoulos [z,b],
M. Andrews [k], R. Andrews [k], C. Arroyo [ac], S. Avvakumov [ac],
D.S. Ayres [a], B. Baller [k], B. Barish [e], M.A. Barker [x], P.D.Barnes Jr. [t],
G. Barr [x], W.L. Barrett [ah], E. Beall [a,v,5], K. Bechtol [ai], B.R. Becker [v],
A. Belias [z], T. Bergfeld [ab,6], R.H. Bernstein [k], D. Bhattacharya [y],
M. Bishai [d], A. Blake [f], V. Bocean [k], B. Bock [w], G.J. Bock [k],
J. Boehm [ℓ], D.J. Boehnlein [k], D. Bogert [k], P.M. Border [v], C. Bower [n],
S. Boyd [y], E. Buckley-Geer [k], A. Byon-Wagner [k], A. Cabrera [x,7],
J.D. Chapman [f], T.R. Chase [v], S.K. Chernichenko [o], S. Childress [k],
B.C. Choudhary [k,e,8], J.H. Cobb [x], S.J. Coleman [ai], J.D. Cossairt [k],
H. Courant [v], D.A. Crane [a], A.J. Culling [f], D. Damiani [ai],
J.W. Dawson [a], J.K. de Jong [m], D.M. DeMuth [v,9], A. De Santo [x,10],
M. Dierckxsens [d], M.V. Diwan [d], M. Dorman [u,z], G. Drake [a],
R. Ducar [k,3], T. Durkin [z], A.R. Erwin [ak], C.O. Escobar [g],
J.J. Evans [u,x], O.D. Fackler [t], E. Falk Harris [ad], G.J. Feldman [ℓ],
N. Felt [ℓ], T.H. Fields [a], R. Ford [k], M.V. Frohne [c,11],
H.R. Gallagher [ag,x,a,v], M. Gebhard [n], A. Godley [ab], J. Gogos [v],
M.C. Goodman [a], Yu. Gornushkin [r], P. Gouffon [aa],
E.W. Grashorn [v,w], N. Grossman [k], J.J. Grudzinski [a], K. Grzelak [aj,x],
V. Guarino [a], A. Habig [w,2], R. Halsall [z], J. Hanson [e], D. Harris [k],
P.G. Harris [ad], J. Hartnell [ad,z,x], E.P. Hartouni [t], R. Hatcher [k],
K. Heller [v], N. Hill [a], Y. Ho [j,12], C. Howcroft [e,f], J. Hylen [k],
M. Ignatenko [r], D. Indurthy [af], G.M. Irwin [ac], C. James [k], L. Jenner [u],
D. Jensen [k], T. Joffe-Minor [a], T. Kafka [ag], H.J. Kang [ac],
S.M.S. Kasahara [v], J. Kilmer [k], H. Kim [e], M.S. Kim [y,13],
G. Koizumi [k], S. Kopp [af], M. Kordosky [ai,u,af], D.J. Koskinen [u,w],

M. Kostin [af,14], S.K. Kotelnikov [s], D.A. Krakauer [a],
S. Kumaratunga [v], A.S. Ladran [t], K. Lang [af], C. Laughton [k],
A. Lebedev [ℓ], R. Lee [ℓ,15], W.Y. Lee [j,16], M.A. Libkind [t], J. Liu [af],
P.J. Litchfield [v,z], R.P. Litchfield [x], N.P. Longley [v], P. Lucas [k],
W. Luebke [m], S. Madani [z], E. Maher [v], V. Makeev [k,o], W.A. Mann [ag],
A. Marchionni [k], A.D. Marino [k], M.L. Marshak [v], J.S. Marshall [f],
J. McDonald [y], A.M. McGowan [a,v,17], J.R. Meier [v], G.I. Merzon [s],
M.D. Messier [n,ℓ], R.H. Milburn [ag], J.L. Miller [q,n,3], W.H. Miller [v],
S.R. Mishra [ab,ℓ], P.S. Miyagawa [x], C.D. Moore [k], J. Morfín [k],
R. Morse [ad], L. Mualem [e,v], S. Mufson [n], S. Murgia [ac],
M.J. Murtagh [d,3], J. Musser [n], D. Naples [y], C. Nelson [k],
J.K. Nelson [ai,k,v], H.B. Newman [e], F. Nezrick [k], R.J. Nichol [u],
T.C. Nicholls [z], J.P. Ochoa-Ricoux [e], J. Oliver [ℓ], W.P. Oliver [ag],
V.A. Onuchin [o], T. Osiecki [af], R. Ospanov [af], J. Paley [n], V. Paolone [y],
A. Para [k], T. Patzak [i,ag], Ž. Pavlović [af], G.F. Pearce [z], N. Pearson [v],
C. W. Peck [e], C. Perry [x], E.A. Peterson [v], D.A. Petyt [v,z,x], H. Ping [ak],
R. Piteira [i], A. Pla-Dalmau [k], R.K. Plunkett [k,1], L.E. Price [a],
M. Proga [af], D.R. Pushka [k], D. Rahman [v], R.A. Rameika [k],
T.M. Raufer [z,x], A.L. Read [k], B. Rebel [k,n], D.E. Reyna [a,18],
C. Rosenfeld [ab], H.A. Rubin [m], K. Ruddick [v], V.A. Ryabov [s],
R. Saakyan [u], M.C. Sanchez [a,ℓ,ag], N. Saoulidou [k,b], J. Schneps [ag],
P.V. Schoessow [a,19], P. Schreiner [c], R. Schwienhorst [v],
V.K. Semenov [o], S. -M. Seun [ℓ], P. Shanahan [k], P.D. Shield [x],
R. Shivane [v], W. Smart [k], V. Smirnitsky [p], C. Smith [u,ad,e],
P.N. Smith [ad], A. Sousa [x,ag], B. Speakman [v], P. Stamoulis [b],
A. Stefanik [k], P. Sullivan [x], J.M. Swan [t], P.A. Symes [ad], N. Tagg [ag,x],
R.L. Talaga [a], A. Terekhov [s], E. Tetteh-Lartey [ae], J. Thomas [u,x,k],
J. Thompson [y,3], M.A. Thomson [f], J.L. Thron [a,20], R. Trendler [k],
J. Trevor [e], I. Trostin [p], V.A. Tsarev [s], G. Tzanakos [b], J. Urheim [n,v],
P. Vahle [ai,u,af], M. Vakili [ae], K. Vaziri [k], C. Velissaris [ak],
V. Verebryusov [p], B. Viren [d], L. Wai [ac], C.P. Ward [f], D.R. Ward [f],
M. Watabe [ae], A. Weber [x,z], R.C. Webb [ae], A. Wehmann [k], N. West [x],
C. White [m], R.F. White [ad], S.G. Wojcicki [ac,1], D.M. Wright [t],
Q.K. Wu [ab], W.G. Yan [h], T. Yang [ac], F.X. Yumiceva [ai,14], J.C. Yun [k],
H. Zheng [e], M. Zois [b], R. Zwaska [k,af]

[a]*Argonne National Laboratory, Argonne, IL 60439, USA*

[b]*Department of Physics, University of Athens, GR-15771 Athens, Greece*

[c]*Physics Dept., Benedictine University, Lisle, IL 60532, USA*

[d]*Brookhaven National Laboratory, Upton, NY 11973, USA*

[e]*Lauritsen Lab, California Institute of Technology, Pasadena, CA 91125, USA*

[f]*Cavendish Laboratory, Univ. of Cambridge, Madingley Road, Cambridge CB3 0HE, UK*

[g]*Univ. Estadual de Campinas, IF-UNICAMP, CP 6165, 13083-970, Campinas, SP, Brazil*

[h]*Inst. of High Energy Physics, Chinese Academy of Sciences, Beijing 100039, China*

[i]*APC – Université Paris 7 Denis Diderot, F-75205 Paris Cedex 13, France*

[j]*Physics Department, Columbia University, New York, NY 10027, USA*

[k]*Fermi National Accelerator Laboratory, Batavia, IL 60510, USA*

[ℓ]*Department of Physics, Harvard University, Cambridge, MA 02138, USA*

[m]*Physics Division, Illinois Institute of Technology, Chicago, IL 60616, USA*

[n]*Indiana University, Bloomington, IN 47405, USA*

[o]*Inst. for High Energy Physics, Protvino, Moscow Region RU-140284, Russia*

[p]*High Energy Exp. Physics Dept., ITEP, 117218 Moscow, Russia*

[q]*Physics Dept., James Madison University, Harrisonburg, VA 22807, USA*

[r]*Joint Inst. for Nucl. Research, Dubna, Moscow Region, RU-141980, Russia*

[s]*Nuclear Physics Dept., Lebedev Physical Inst., 117924 Moscow, Russia*

[t]*Lawrence Livermore National Laboratory, Livermore, CA 94550, USA*

[u]*Dept. of Physics and Astronomy, University College London, London WC1E 6BT, UK*

[v]*University of Minnesota, Minneapolis, MN 55455, USA*

[w]*Dept. of Physics, Univ. of Minnesota – Duluth, Duluth, MN 55812, USA*

[x]*Sub-department of Particle Physics, Univ. of Oxford, Oxford OX1 3RH, UK*

[y]*Dept. of Physics and Astronomy, Univ. of Pittsburgh, Pittsburgh, PA 15260, USA*

[z]*Rutherford Appleton Laboratory, Chilton, Didcot, Oxfordshire, OX11 0QX, UK*

[aa]*Inst. de Física, Univ. de São Paulo, CP 66318, 05315-970, São Paulo, SP, Brazil*

[ab]*Dept. of Physics and Astronomy, Univ. of South Carolina, Columbia, SC 29208, USA*

[ac]*Department of Physics, Stanford University, Stanford, CA 94305, USA*

[ad]*Dept. of Physics and Astronomy, University of Sussex, Falmer, Brighton BN1 9QH, UK*

[ae]*Physics Dept., Texas A&M Univ., College Station, TX 77843, USA*

[af]*Dept. of Physics, Univ. of Texas, 1 University Station, Austin, TX 78712, USA*

[ag]*Physics Dept., Tufts University, Medford, MA 02155, USA*

[ah]*Physics Dept., Western Washington Univ., Bellingham, WA 98225, USA*

[ai]*Dept. of Physics, College of William & Mary, Williamsburg, VA 23187, USA*

[aj]*Faculty of Physics, Warsaw University, Hoza 69, PL-00-681 Warsaw, Poland*

$^{\mathrm{ak}}$*Physics Dept., Univ. of Wisconsin, Madison, WI 53706, USA*

Abstract

The Main Injector Neutrino Oscillation Search (MINOS) experiment uses an accelerator-produced neutrino beam to perform precision measurements of the neutrino oscillation parameters in the "atmospheric neutrino" sector associated with muon neutrino disappearance. This long-baseline experiment measures neutrino interactions in Fermilab's NuMI neutrino beam with a near detector at Fermilab and again 735 km downstream with a far detector in the Soudan Underground Laboratory in northern Minnesota. The two detectors are magnetized steel-scintillator tracking calorimeters. They are designed to be as similar as possible in order to ensure that differences in detector response have minimal impact on the comparisons of event rates, energy spectra and topologies that are essential to MINOS measurements of oscillation parameters. The design, construction, calibration and performance of the far and near detectors are described in this paper.

1 Introduction

The Main Injector Neutrino Oscillation Search (MINOS) experiment is designed to perform precise measurements of neutrino oscillation parameters from ν_μ disappearance using an accelerator-produced muon neutrino beam. MINOS uses two detectors, called "near" and "far," to measure the characteristics of an intense Fermilab neutrino beam over a baseline distance of 735 km. The two detectors are designed to be as similar as possible so that many details of their responses will cancel in comparisons of neutrino event characteristics between the near and far ends of the baseline. The purpose of this paper is to describe the design, construction, calibration and performance of the detector systems used in the MINOS experiment. Brief overviews of the neutrino beam and the detectors are given below, concluding with an outline of the detector system presentations which constitute the core of this paper.

MINOS utilizes 120 GeV protons from the Fermilab Main Injector to create the high-intensity NuMI (Neutrinos at the Main Injector) neutrino beam [1]. The beam-

[1] Co-Spokesperson

[2] Corresponding author. *Email address:* ahabig@umn.edu (A. Habig)

[3] Deceased

[4] Now at Dept. of Physics, National Tech. Univ. of Athens, GR-15780 Athens, Greece

[5] Now at Cleveland Clinic, Cleveland, OH 44195, USA

[6] Now at GE Healthcare, Florence SC 29501, USA

[7] Now at APC – Université Paris 7 Denis Diderot, 10, rue Alice Domon et Léonie Duquet, F-75205 Paris Cedex 13, France

[8] Now at Dept. of Physics & Astrophysics, Univ. of Delhi, Delhi 110007, India

[9] Now at Math, Science and Technology Dept., Univ. of Minnesota – Crookston, Crookston, MN 56716, USA

[10] Now at Physics Dept., Royal Holloway, Univ. of London, Egham, Surrey, TW20 0EX, UK

[11] Now at Holy Cross College, Notre Dame, IN 46556, USA

[12] Now at Dept. of Rad. Oncology, Beth Israel Med. Center, New York, NY 10003, USA

[13] Now at Centre for Particle Physics, Univ. of Alberta, Edmonton, Alberta T6G 2G7 Canada

[14] Now at Fermi National Accelerator Laboratory, Batavia, IL 60510, USA

[15] Now at Lincoln Laboratory, Massachusetts Institute of Technology, Lexington, MA 02420, USA

[16] Now at Physics Div., Lawrence Berkeley National Laboratory, Berkeley, CA 94720, USA

[17] Now at Physics Department, St. John Fisher College, Rochester, NY 14618, USA

[18] Now at Radiation and Nuclear Detection Systems, Sandia National Laboratories, Livermore, CA 94551, USA

[19] Now at Euclid Techlabs LLC, Solon, OH 44139, USA

[20] Now at Nucl. Nonprolif. Div., Threat Reduc. Dir., Los Alamos National Laboratory, Los Alamos, NM 87545, USA

line is precisely aimed in the direction of the Soudan Underground Laboratory in northern Minnesota. The NuMI beam provides a high flux of neutrinos at the end of the decay volume in the energy range $1 < E_\nu < 30\,\mathrm{GeV}$, but the flux at Soudan is reduced by a factor of about 10^6 due to the intrinsic divergence of the beam. The relative rates of neutrino charged-current interactions in the MINOS near detector at Fermilab are approximately 92.9% ν_μ, 5.8% $\overline{\nu}_\mu$, 1.2% ν_e and 0.1% $\overline{\nu}_e$ for the low-energy beam configuration. With the parameters for ν_μ to ν_τ oscillations measured by Super-Kamiokande [2] and other experiments ($\Delta m_{32}^2 \simeq 2.5 \times 10^{-3}\,\mathrm{eV}^2$ and $\sin^2 2\theta_{23} \simeq 1.0$), the Fermilab-to-Soudan distance implies that the neutrino interactions of most interest will be in the $1 < E_\nu < 5\,\mathrm{GeV}$ range. Details of this experiment's measurements are published elsewhere [3,4].

The MINOS experiment uses two detectors to record the interactions of neutrinos in the NuMI beam. A third detector, called the calibration detector, was exposed to CERN test beams in order to determine detector response. The near detector at Fermilab is used to characterize the neutrino beam and its interactions and is located about 1 km from the primary proton beam target, the source of the neutrino parent particles. The far detector performs similar measurements 735 km downstream. The essence of the experiment is to compare the rates, energies and topologies of events at the far detector with those at the near detector, and from those comparisons determine the relevant oscillation parameters. The energy spectra and rates are determined separately for ν_μ and ν_e charged-current (CC) events and for neutral current (NC) events.

All three MINOS detectors are steel-scintillator sampling calorimeters with tracking, energy and topology measurement capabilities. This is achieved by alternate planes of plastic scintillator strips and 2.54 cm thick steel plates. The near and far detectors have magnetized steel planes. The calibration detector was not magnetized as the particle momenta were selected a priori. The 1 cm thick by 4.1 cm wide extruded polystyrene scintillator strips are read out with wavelength-shifting fibers and multi-anode photomultiplier tubes. All detectors provide the same transverse and longitudinal sampling for fiducial beam-induced events.

The far detector, shown in Fig. 1, is located in Soudan, MN (47.8° N latitude, and 92.2° W longitude), 735.3 km from the NuMI beam production target at Fermilab, in an inactive iron mine currently operated as a State Park by the Department of Natural Resources of the State of Minnesota. Much of the infrastructure used in the mining days is still in service and is used to support the operation of the experiment. The detector is housed in a specially excavated cavern, 705 m underground (2070 meters-water-equivalent), 210 m below sea level. The far detector consists of 486 octagonal steel planes, with edge to edge dimension of 8 m, interleaved with planes of plastic scintillator strips. This 5,400 metric ton detector is constructed as two "supermodules" axially separated by a 1.15 m gap. Each supermodule has its own independently controlled magnet coil. The first (southernmost) supermodule contains 249 planes and is 14.78 m in length while the second supermodule is com-

prised of 237 planes and has a length of 14.10 m. The most upstream planes in each supermodule (planes 0 and 249) are uninstrumented. The north end view of the second supermodule is shown in Fig. 1.
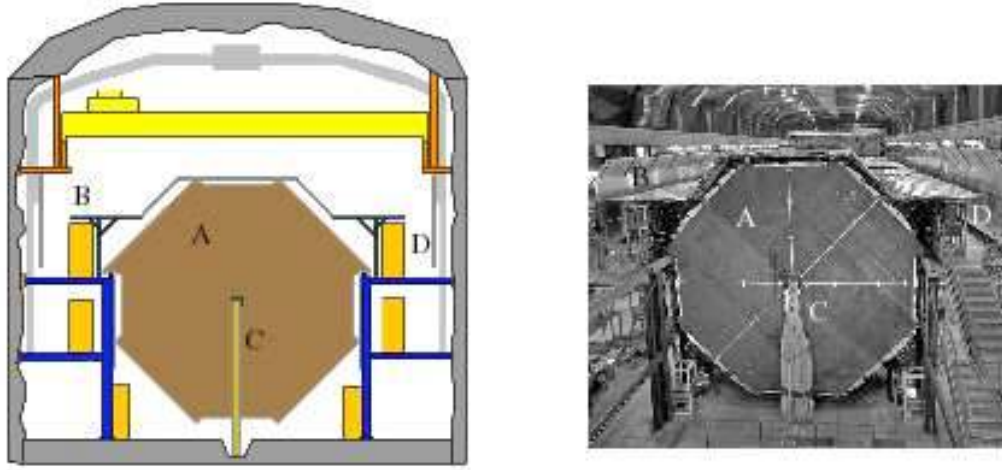

Fig. 1. End views of the second far detector supermodule, looking toward Fermilab. The drawing (left) identifies detector elements shown in the photograph (right): 'A' is the furthest downstream steel plane, 'B' is the cosmic ray veto shield, 'C' is the end of the magnet coil and 'D' is an electronics rack on one of the elevated walkways alongside the detector. The horizontal structure above the detector is the overhead crane bridge.
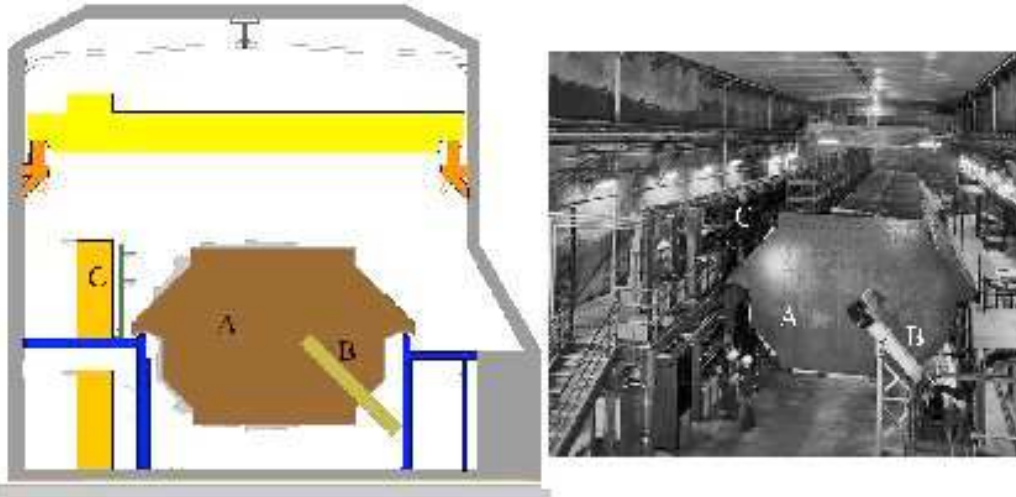

Fig. 2. End view of the near detector, looking toward Soudan. The drawing (left) identifies detector elements shown in the photograph (right): 'A' is the furthest upstream steel plane, 'B' is the magnet coil, and 'C' is an electronics rack on the elevated walkway. Above the detector is the overhead crane bridge. The NuMI beam intersects the near detector near the "A" label.

The 282 plane, 980 metric ton MINOS near detector, shown in Fig. 2, is located at the end of the NuMI beam facility at Fermilab in a 100 m deep underground cavern, under a 225 mwe overburden. The design of the near detector takes advantage of the high neutrino flux at this location to define a relatively small target fiducial volume

for selection of events for the near/far comparison. The upstream part of the detector, the calorimeter section, contains the target fiducial volume in which every plane is instrumented. The downstream part, the spectrometer section, is used to measure the momenta of energetic muons and has only every fifth plane instrumented with scintillator.

The much smaller calibration detector was used to measure the detailed responses of the MINOS detectors in a charged-particle test beam. This 12 ton detector consisted of 60 planes of unmagnetized steel and scintillator, each 1×1 m^2. It was exposed to protons, pions, electrons and muons in test beams at the CERN PS [5] to measure the energy and topological responses expected in the the near and far detectors. In order to include response variations due to the different electronics used in the detectors, the calibration detector acquired data with both near and far detector electronics. The energy responses of the three MINOS detectors were normalized to each other by calibrating with cosmic-ray muons.

The choice of solid scintillator as the MINOS detectors' active system was the result of a three year research and development process which also evaluated the possibility of liquid scintillator, Iarocci tubes (or their variants) and RPCs [6, 7]. Solid scintillator was chosen for a number of reasons (not all unique to this technology): good energy resolution, excellent hermiticity, good transverse segmentation, flexibility in readout, fast timing, simple and robust construction, potential for distributed production, long-term stability, ease of calibration, low maintenance, and reliability. The MINOS Detectors Technical Design Report [8] summarizes the decision making process as follows:

> The development program has included extensive laboratory tests of different active detector technologies, test beam work, Monte Carlo simulations of reactions of interest to MINOS, and evaluation of the costs of different options. We believe that this baseline design represents the best experimental approach, in light of the current knowledge of neutrino oscillation physics, and also offers a high probability of being able to react effectively to potential future physics developments.

Safety and practicality of construction were also important criteria. After the solid scintillator decision was made, a second phase of design optimization occurred, where parameters such as steel thickness, width of scintillator strips, and degree of readout multiplexing were set based on Monte Carlo studies [8]. These were trade-offs between cost and performance. The channel that is most sensitive to these choices is $\nu_\mu \rightarrow \nu_e$ appearance. Narrower strips and thinner steel plates would improve e identification ability, however that gain was counterbalanced by the loss in statistics (for the same construction cost). Another consideration for strip width was muon energy resolution; but that was dominated by Coulomb scattering (or range measurement) and not very sensitive to the strip width. The steel thickness is also relevant for shower energy resolution but 2.5 cm was adequate. Note that

the ability to react to developments in the field was tested when the high Δm^2 value hinted at by the original Kamiokande measurements [9] was superseded by the current low Δm^2 [10] after the civil construction had begun and these design decisions had already been made.

The MINOS detectors required a significant scale-up in size from previous fine-grained scintillator sampling calorimeters, hence creative reductions in costs per unit of the scintillator and electronics systems resulted. The final design includes advances in detector technology which will be of interest to future detector applications requiring large areas of plastic scintillator.

The MINOS near and far detectors have now been been operating for several years, both with cosmic-ray events and with the accelerator neutrino beam. The far detector started commissioning data collection in September 2002, and has been fully operational for cosmic-ray and atmospheric-neutrino data since July 2003. The near detector has been operating since January 2005. The NuMI beam started providing neutrinos to the MINOS experiment in March 2005.

This paper summarizes the considerations that have driven the detector designs, provides details of individual subsystems, describes the construction and installation issues, and presents performance data from operational experience and from bench measurements of subsystems. It also provides a framework for more detailed publications, either already in print or in preparation, which discuss specific detector subsystems.

The remainder of this paper is organized as follows: Section 2 describes the steel detector planes, the magnetic coils, and the resulting detector magnetization. Section 3 contains a detailed description of the scintillator system that is the heart of the MINOS detectors. It includes the design and fabrication of the scintillator strips and the characteristics of the wavelength-shifting fibers and photomultiplier tubes that read them out. It describes the assembly of extruded plastic scintillator strips into modules and the performance of those modules. Section 4 covers the electronics and data acquisition systems for the near and far detectors; these require different front-end designs because of the very different counting rates at the two detector locations. Section 5 gives detailed descriptions of the calibrations of the two detectors and their electronic readout systems. Section 6 describes the facilities of the underground laboratories in which the near and far detectors are located. It also covers the installation of the detectors and the survey techniques used to determine the direction of the far detector from Fermilab as required for the precise aiming of the neutrino beam. Section 7 documents the overall performance of the detector systems in the MINOS experiment and also includes a brief description of the computer software used to measure performance and analyze MINOS data. Section 8 concludes with a brief summary of detector performance as observed in data-taking currently underway.

2 Steel Planes, Magnet Coils and Magnetic Fields

The MINOS near and far detectors are sampling calorimeters that utilize toroidally magnetized, 2.54 cm thick steel planes [11] as the passive absorber material. The differences in beam sizes and neutrino interaction rates at the near and far detector sites led to substantially different magnetic designs for the two detectors and allowed the near detector to be much smaller and less costly than the far detector. This section summarizes the specifications, designs, and performance of the steel and coils.

2.1 Magnet design

The MINOS magnets are designed to provide a measurement of muon momentum based on curvature with resolution of $\sigma_P/P \sim 12\%$ for muons with energies greater than 2 GeV, and to facilitate the containment of negatively charged muons. The average fields in the near and far detectors were required to have similar strengths to minimize systematic uncertainties arising from near/far detector differences. The field strength averaged over the fiducial volume in the near detector 1.28 T, compared to 1.42 T in the far detector. One of the design goals of the magnet system is that the average magnetic field in each toroid be known to better than 3%. Monte Carlo studies indicate that uncertainties in the magnetic field strength at this level result in detector acceptance uncertainties of significantly less than 1% at all muon energies of interest, and an average uncertainty in the energy of exiting tracks of less than 2%. The magnetic calibration specifications require that stochastic variations in field strength between different steel planes not significantly degrade the overall momentum resolution. Monte Carlo studies of the effect of plane-to-plane field variations on momentum resolution provide a specification of stochastic residual variations (after global calibration) of less than 15%.

2.2 Steel planes

2.2.1 Far detector configuration

The MINOS far detector has 486 steel planes, each one constructed of eight component plates. All detector components were moved underground through the existing mineshaft, which limited dimensions to $9 \times 2 \times 1 \, \text{m}^3$ and weights to 5.5 metric tons or less. Each 8 m wide octagonal steel plane was constructed underground by plug-welding together eight 2 m wide, 1.27 cm thick plates. After attaching scintillator-strip modules to one side, the planes were mounted vertically with a 5.95 cm center-to-center spacing. The basic far detector steel plane construction is shown in Fig. 3.
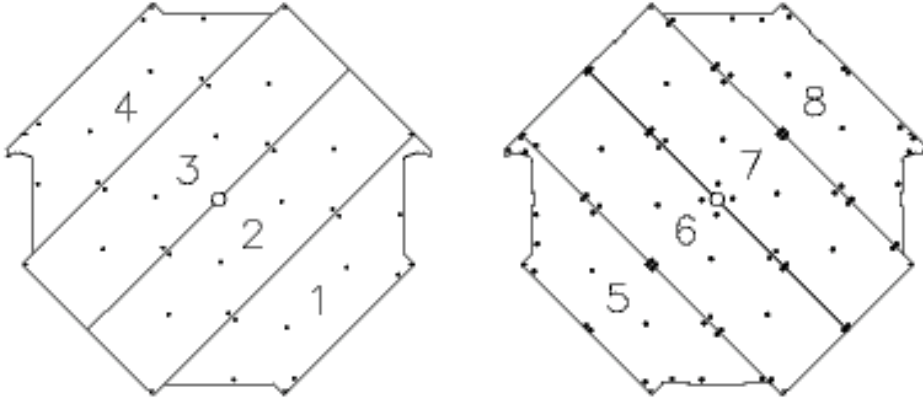
Fig. 3. Arrangement of steel plates in the two layers of a far detector plane, showing the plate numbering scheme. A drawing of the bottom (downstream) layer is on the left and the top (upstream) layer is on the right, both seen looking toward Fermilab. "Top" and "Bottom" refer to how they were stacked when being assembled. The dots indicate holes for the plug welds or handling fixtures. Numbering is along the U (left) and V (right) axes. The installed planes are supported by the "ears" on plates 1, 4, 5 and 8.

2.2.2 Steel plane construction

Each plane was assembled on a steel lift frame (called a "strongback"), which was used to lift the completed plane onto the support structure. Each plate is identified by a part number specifying where it fits in the octagon, a "heat number" specifying the batch of steel from which it is made, and a serial number unique to that plate.

The construction of each of the 486 detector planes began with the placement and alignment of four steel sheets on a strongback to form the bottom of two layers. The top layer was then placed and aligned in the orthogonal direction. The plates were placed to minimize gaps between sheets. The eight sheets of a complete plane were then welded together via seventy-two 2.5 cm diameter plug-weld holes in the top set of sheets (Fig. 3). Surviving gaps of greater than 2 mm were measured and recorded. Most of these gaps were in the range of 2–4 mm and at most 9 mm. Fewer than half of the seams had recordable gaps, typically located at the outer edge of the seam and about 30 cm to 50 cm long. Following the assembly of the steel planes, the scintillator detectors were mounted on the plane and the full assembly lifted into place.

The assembled planes are supported on two rails, one on each side of the detector. Each plane is bolted to the previously-installed plane with 8 axial bolts around the periphery and 8 additional bolts around the central coil hole. The steel planes are magnetically isolated from the steel support structure by 1 cm thick stainless steel strips between the plates and the support rails. Plumbness and plane to plane alignment were obtained by checking each plane as it was installed using a laser survey device (Ref. [12] and Sec. 6.6), occasionally adding shims as needed when new planes were bolted to a supermodule to maintain the specification of 6.4 mm

plumbness.

2.2.3 Steel characteristics

The steel plates were made from low-carbon (AISI 1006 designation) hot-rolled steel. They were required to have flatness to better than 1.5 cm – half the ASTM A-6 specification [13]. The carbon content was specified to be (0.04±0.01)%. Samples from each of the 45 foundry runs (called "heats") were tested to ensure that their radioactivity was less than 0.15 γ/kg/sec for γ-rays above 0.5 MeV. From block samples of the various heats, the average steel density is found to be 7.85±0.03 g/cm^3.

As steel was delivered over the course of construction, each plate was individually weighed using a scale with a least count of 0.9 kg, and this value was compared to a nominal weight for that part number. The scale calibration was checked and verified to be stable during construction. An uncertainty of 1 kg in the plate masses implies a plane-mass uncertainty of $\sqrt{8}$ kg $\simeq$ 3 kg. Deviations from the nominal weight were found to be correlated with variations in the thickness of the steel. The first 190 (upstream) planes had an average mass of 10,831 kg and the remaining 296 (downstream) planes had an average mass of 10,718 kg. The rms mass variation within each group of planes is 0.35%, which grows to 0.62% if the detector is considered as a whole.

Requirements on the accuracy of the target mass and on muon range measurements imposed the specification that the fiducial masses of the near and far detectors be known to 1%. The average thickness of the near detector planes was measured to be 2.563±0.002 cm, compared to 2.558±0.005 cm for the far detector.

2.2.4 Near detector steel

The near detector was assembled from 282 steel planes, fabricated as single plates of 2.54 cm thickness from a subset of the same foundry heats used for the far detector steel. The near detector target (fiducial) region was chosen to be 2 m in diameter to give a high rate of fully contained neutrino interaction events in the central region of the beam. The magnet coil hole in the steel plates was located outside this area.

Plate thickness variations in the near detector planes were found to be ∼0.3% by surveying with an ultrasound probe. No systematic difference in steel density was found between the two detectors. As was required for the far detector steel, the flatness specification for the near detector plates was set at half of the ASTM A-6 flatness standard, or 1.5 cm.

2.3 Magnet coils

The near and far detector steel geometries place somewhat different requirements on their respective magnet coil designs. The coil designs were optimized separately, taking into account differing detector geometry as well as differences in the laboratory infrastructures available at Fermilab and Soudan.

2.3.1 Far detector coil

Each supermodule is independently magnetized by its own coil [14], as shown by item "C" in Fig. 1. Each coil consists of a central bore leg running through holes at the center of each plane, a single return leg located in a trench beneath the detector, and end legs that connect the bore to the return legs. Figure 4 shows a schematic cross section of the coil in the central bore leg, inside a supermodule. The conductor consists of 190 turns of 1/0 gauge stranded copper wire with Teflon insulation (National Electrical Code designation TGGT). The bore leg is housed inside a 25 cm diameter, water-cooled copper jacket. The return leg is also water cooled and the end legs are air-cooled. An 80 A power supply gives a 15.2 kA-turn total current that provides an average toroidal magnetic field of 1.27 T. Each coil dissipates 20 kW.
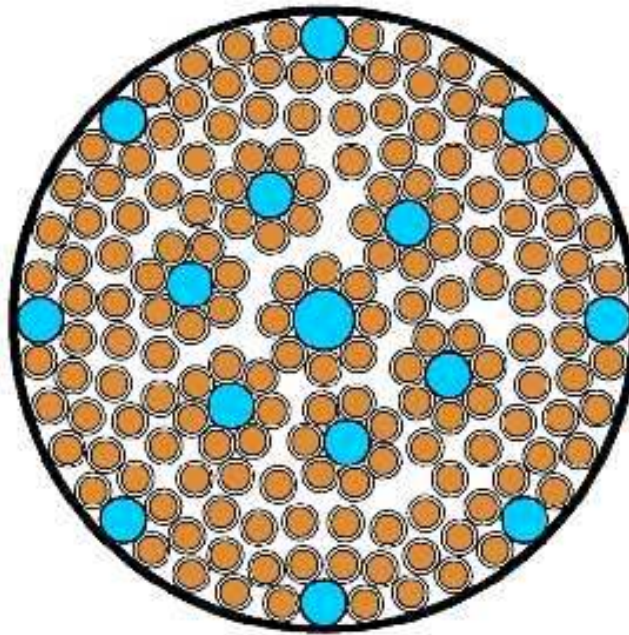

Fig. 4. Cross section schematic of one of the far detector supermodule coils. The larger diameter circles represent the copper cooling tubes and the smaller circles are the 190 turns of 1/0 gauge stranded copper wire. The outlines of these conductors are to-scale representations of the insulator thickness. The outer circumference of the assembly is a copper-sheet jacket cooled by eight cooling tubes.

In order to minimize temperature induced aging of nearby scintillator, the outer jacket characteristics were designed to ensure a worst case maximum temperature of 150° C. Each coil's cooling-water system carries 72 l/min and was designed to remove up to 25 kW of heat per supermodule. A secondary heat-exchange system removes the heat from the underground laboratory. Fixtures along the air-cooled end legs of the coil provide a 15 cm separation between the coil and the steel planes to allow air circulation and to reduce distortion of the field in supermodule end planes by the current in the end-legs of the coil.

2.3.2 Near detector coil

The near detector coil hole is offset 55.8 cm from the center of the plane and the detector is placed so that beam is centered halfway between the hole and the left vertical edge of the plane, as shown in Fig. 2. Because of the squashed-octagon geometry, a 40 kA-turn current is required to achieve sufficient fields. Figures 5 and 6 show the cross section and the geometry of the near detector coil, respectively. The coil [15] consists of eight turns, each with 18.76 m-long bore and return legs and two 2.89 m-long end legs that connect the bore and return. The return leg is routed along the lower east 45° face of the steel plane. The high current carried by the coil requires substantial cooling, provided by a closed loop low-conductivity water system that transfers the heat out of the underground enclosure. There are no photodetectors on the coil-return side of the near detector by design, so the fringe fields from the return do not affect detector operation.

The coil conductor is made from cold conformed aluminum and has a 2.79×3.81 cm^2 rectangular cross section with a 1.65 cm diameter central water channel. The 48 conductors are arranged in a six by eight rectangular pattern, with groups of six conductors formed into "planks." The current runs in parallel through the conductors within a plank. The electrical connections were made with full-penetration aluminum welds at each end. This offers the potential to disassemble the coil for repair or replacement in case of failure. The coil is a single eight-turn 5 kA electrical circuit which dissipates a power of 47 kW. Cooling water of less than 80° C flows through the coil at 380 l/min, limiting conductor temperature.

2.4 Detector plane magnetization

2.4.1 Magnetic field determination

The finite element analyses (FEA) of both the near and far detectors' magnetic fields were performed with the ANSYS [16] general purpose finite element program, using a 3-D scalar magnetic potential approach. The accuracy of the field values depends on the mesh density (discretization) of the model, the input magnetization ("B-H") curve, and the normalization to coil currents set using power-
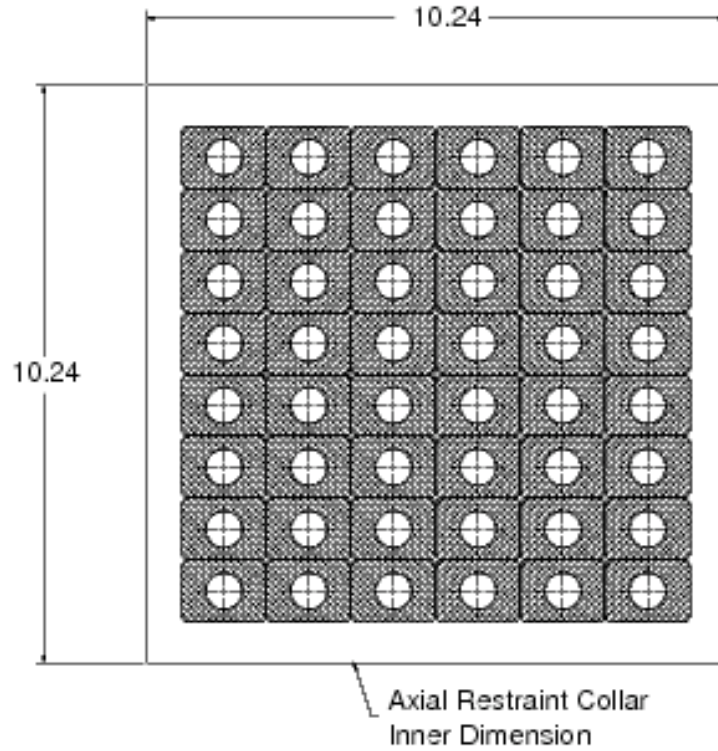
Fig. 5. Cross section schematic of the near detector coil. The dimensions shown are in inches.
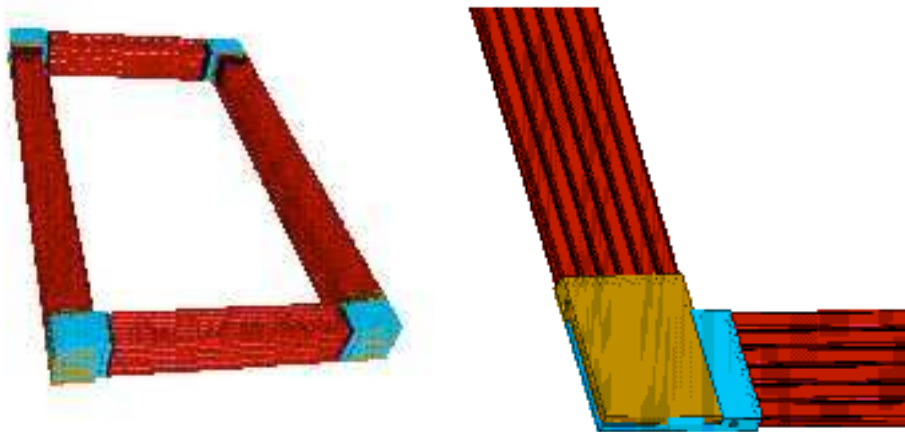

Fig. 6. Sketches of the four legs of the near detector coil assembly (left) and of one lap joint between two coil planks (right).

supply current shunts. Figure 7 shows the results of FEA calculations of the near and far detector magnetic field maps for detector planes near the detector centers.

There are a number of potential sources of plane-to-plane magnetic field variations, including mechanical and chemical nonuniformity and field distortion at the ends of the toroids. The steel for the two detectors was produced in 45 different foundry

heats with slightly different chemical compositions (and hence magnetic proper-
ties). Test toruses were fabricated from the steel in each heat and used to measure
B-H curves by magnetic induction. The variations in these B-H curves between
heats were found to be small, allowing all plane field maps to be based upon a sin-
gle representative B vs H relationship. FEA calculations confirmed that expected
mechanical variations between planes, such as variations in the gap between steel
sheets in the far detector, yield less than 15% field differences. Finally, the presence
of coil end legs introduces field distortion in the end planes of each toroid. These
end effects were shown to have a negligible effect on momentum measurements
at the level required for early MINOS results, and for these studies a single field
map appropriate to the center of the near or far detector was used for all planes. For
subsequent analysis and simulation, the effect of the proximity of the coil return on
the field of planes near a detector or supermodule end is accounted for via interpo-
lation. The FEA generated fields for the end plane, the third plane, and an interior
plane are interpolated to the outer ten planes in each detector. The accuracy of this
interpolation technique was confirmed by comparing its values to actual field maps
of the last 12 planes. The residual RMS field errors from the interpolation procedure
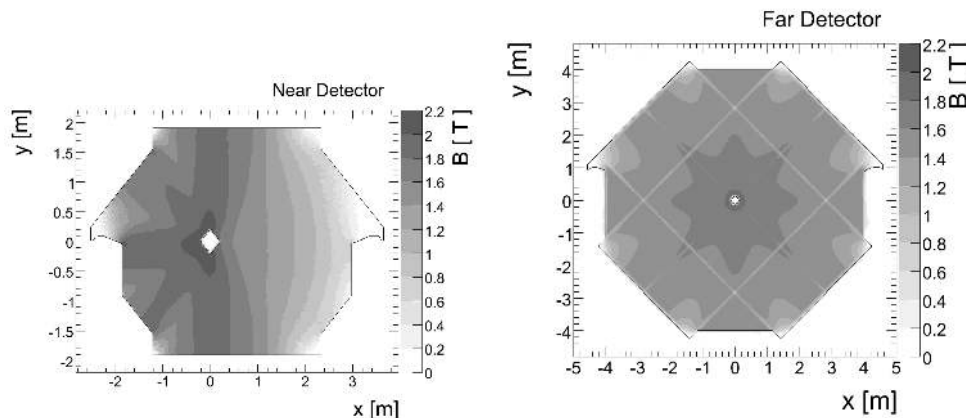have been shown to be less than 5 Gauss for all intermediate planes.

Fig. 7. Magnetic field maps for a typical near (left) and far (right) detector plane. The
greyscale indicates the magnetic field strength B as calculated by finite element analyses
using 3-D models. Note that the near detector plane is shown looking upstream to the
neutrino beam in this figure, whereas in Fig. 2 the view is to the downstream direction. The
effect on the field of joints between the steel pieces used to make the far detector planes is
seen as the straight light grey lines in the lower figure.

To normalize the field maps, each of the near and far detector planes is equipped
with 50-turn magnetic induction coils that measure the average magnetic flux along
a line from the coil to the detector periphery at discrete angles. When instrumented
with precision analog integration readouts, the induction coils provide a measure-
ment of the average magnetic flux through the steel with uncertainties of less than
2%.

A second method of determining the magnetic field map comes from analyzing

17

the trajectories of stopping muons. For this class of events two redundant measurements of muon momentum are available, one based on range (P_{range}), and the other on the measured curvature of the track (P_{fit}). The systematic error in the range-based momentum arises primarily from uncertainty in the detector mass, approximations to the true detector geometry made in the reconstruction software, and uncertainties in the underlying energy loss model used. The combination of these effects results in a 2% systematic error in the track momentum from range. The ratio P_{range}/P_{fit} therefore provides a means of assessing the consistency of the range-based and curvature-based energy scales for contained tracks to the same level of precision.

The comparison of the P_{range}/P_{fit} ratio between the Monte Carlo (MC) simulation, where the magnetic field is known perfectly, and the data gives the estimate of the magnetic field uncertainty in measuring muon momentum from curvature in the actual detector. The double ratio $(P_{range}/P_{fit})_{data}/(P_{range}/P_{fit})_{MC}$ directly compares two methods of determining muon momentum for the data and the simulation and does not depend on reconstruction effects. The well defined muon tracks produced in the neutrino interactions of beam neutrinos in the near detector, when analyzed for the measurement of the magnetic field uncertainty, produce the value $(P_{range}/P_{fit})_{data}/(P_{range}/P_{fit})_{MC} \approx 1.01$ [17]. This result is consistent with both the final measurement of the magnetic field strength and the uncertainty on the range measurement of the stopping muon tracks in the data and the simulation.

3   Scintillator system

The MINOS scintillator system consists of approximately 100,000 extruded polystyrene scintillator strips, each 4.1 cm wide, 1.0 cm thick and up to 8 m long; the total surface area of this system is 28,000 m^2. Fiber readout of extruded scintillator was chosen as opposed to direct readout of cast scintillator because of a nearly 20::1 cost advantage. Most of the cost savings comes from the use of wavelength shifting (WLS) fibers to channel the light to the ends of the strips. WLS fibers minimize self-absorption by absorbing light peaked at 420 nm and re-emitting it at 470 nm. One WLS fiber runs down the center of the wide face of each strip and collects the light from the entire strip, leading to a reduction in photocathode area (compared to direct scintillator readout) by a factor of over 300. Optical summing of the WLS fiber light readout in the far detector led to further cost saving as the result of reductions in the number of PMTs and associated electronics channels.

3.1 General description of the scintillator system

We describe here the specifications that led to the design of the plastic scintillator system. Because of its large size, the far detector drove the design features of the system and we describe it first, then describe how the near detector differs.

(i) **Geometry:** Each steel octagon (8 m across) is covered by a plane of scintillator. Each plane has one "view" of strips, with the next plane having the orthogonal view. The two views are at $\pm 45°$ relative to the vertical in order to avoid having strip readout connections at the bottom of the detector. The 4.1 cm strip width was the result of an optimization that included the response of the detector to simulated neutrino interactions and cost considerations.

(ii) **Modularity:** The planes were built from modules, each consisting of groups of scintillator strips placed side-by-side and sandwiched between aluminum covers. The strips were glued to one another and to the covers to make rigid, mechanically strong, light-tight modules. WLS fibers were routed through manifolds at both ends of the modules to bulk optical connectors. Continuous scintillator planes were formed by placing eight of these modules next to one another on a steel detector plane.

(iii) **Routing of scintillator light:** Light from the end of each WLS fiber is carried by a clear fiber to a Hamamatsu R5900-00-M16 PMT, which has sixteen $4 \times 4 \, mm^2$ pixels. Eight fibers from non-neighboring scintillator strips are mapped onto one pixel, as described in Sec. 3.5.

(iv) **Light output:** In general, strips produce different amounts of light when excited by a normally incident, minimum ionizing particle (MIP). Only events producing a total of at least 4.7 photoelectrons summed over both ends were used in the later analyses. In addition, the average light output for a MIP crossing at the far end of a strip as seen from the other end should be greater than 1.0 photoelectron.

(v) **Uniformity:** After a correction for fiber attenuation, the light output is uniform over all the scintillator strips to within $\pm 30\%$. WLS fiber length is the most important cause of strip-to-strip differences in light output.

(vi) **Calibration:** The absolute response to hadronic energy deposition was calibrated to 6%. In addition, the relative response of the near detector to the far detector and between different locations within the far detector were calibrated to 3%.

(vii) **Short-term stability:** It was required that the average light output should vary by less than 1% per month of operation. This duration is determined by the time required for a complete cosmic-ray muon calibration of the far detector. PMT gains which vary more rapidly than this can be corrected by equalizing the response to hourly LED light injections, and cosmic ray muons are used to correct for drifts on a daily basis.

(viii) **Long-term stability:** Decrease in light output due to the aging of various components is the main effect over the long term. The design goal was that

there should be no more than a 30% decrease in light output over a period of ten years; this will not significantly degrade the detector's physics performance.

(ix) **Linearity:** The response of the system depends linearly on hadronic energy deposition to within 5% up to 30 GeV.

(x) **Time measurement:** Time measurements are primarily useful for studies of atmospheric neutrinos in the far detector because accurate time-of-flight measurements can distinguish upward-going neutrino events from backgrounds induced by downward-going cosmic-ray muons. The detector has a time resolution of better than 5 ns for five observed photoelectrons (assuming that this resolution scales as $1/\sqrt{N_{\mathrm{pe}}}$).

Figure 8 illustrates the light detection and collection for part of one scintillator module. Clear fiber cables connect to the module and transmit light from the edges of the detector to centralized locations where the PMTs and readout electronics are mounted (Sec. 3.5.2). A light injection system illuminates the the WLS fibers near their ends with LED-generated UV light to perform the system's primary calibration (see Fig. 31 in Sec. 5.1).

The primary task of the far detector is the measurement of the properties of neutrinos initiated from the Fermilab beam. A secondary task is the detection and characterization of atmospheric neutrinos. This second measurement, however, must contend with large backgrounds from high energy gammas and neutral hadrons produced by cosmic-ray muon interactions in the rock surrounding the detector. These backgrounds have been strongly reduced by deploying an active veto shield made of MINOS scintillator modules. This anticoincidence layer detects hadron shower remnants emerging from the rock above and beside the detector. The shield's design and performance are described in Section 3.7.

The near detector is designed to have similar physics response to neutrino events as the far detector. However, some differences are unavoidable because the neutrino event rate per unit mass is a factor of 10^6 greater than that in the far detector. The key differences between the scintillator systems of the near detector and far detector are:

(i) The near detector scintillator modules are much shorter, ranging from 2.5 m to 6 m in length.

(ii) The long WLS fibers of the far detector (and their corresponding ∼5 m attenuation lengths) required readout of both ends. In contrast only one end of each near detector WLS fiber is read out. With a mirrored far end, the near detector WLS fiber gives approximately the same light yield as the dual-ended readout in the far detector. Single-ended readout necessitates attaching each Hamamatsu R5900-00-M64 photomultiplier pixel to only one scintillator strip. This PMT has sixty-four $2 \times 2\,\mathrm{mm}^2$ pixels but is otherwise very similar in construction and response to the R5900-00-M16 PMTs used in the far detector.
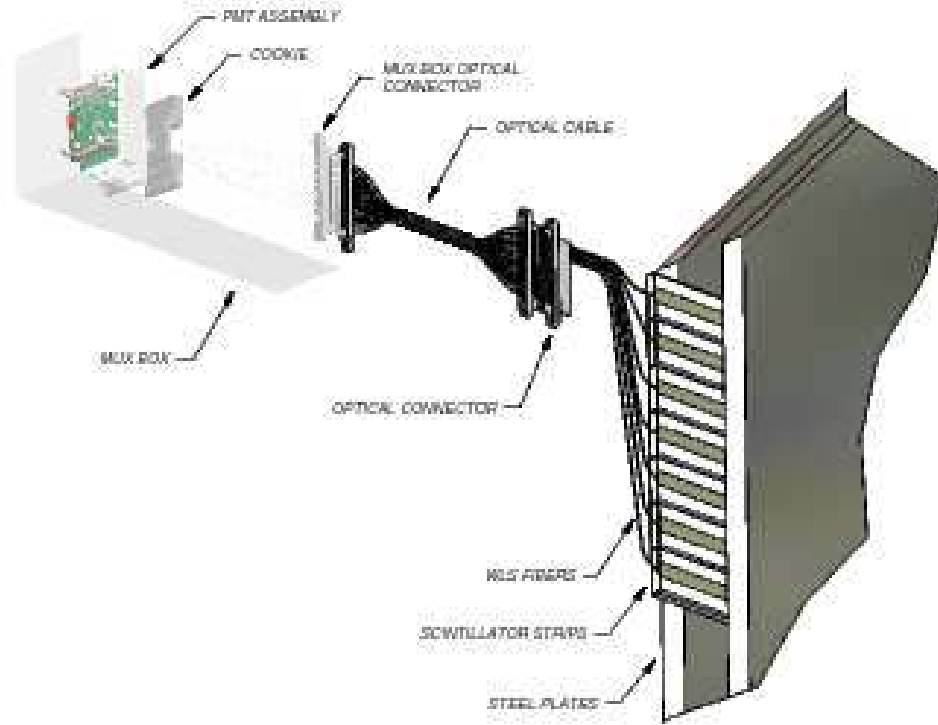
Fig. 8. Schematic drawing of the scintillator system readout for a module. An edge of a detector plane is on the right side of the sketch, showing several strips extending out of a scintillator module and beyond the edge of the plane for clarity. The light produced in a strip (Fig. 9) travels out of the module in a WLS fiber, and is then carried by a clear optical fiber (assembled into a cable) to a multiplexing (MUX) box where it is routed to a pixel of the photomultiplier tube (PMT) assembly.

(iii) Due to its much higher event rate, the near detector requires faster, dead-time free readout electronics.

All other features of the near and far detector scintillator systems are identical, including the strips, the WLS and clear fibers, the light injection systems, and construction techniques of the modules. The resulting physics capabilities are discussed in Sec. 5.3.

3.2 Scintillator strips

Three technologies are crucial to the scintillator system, namely: i) low-cost extruded polystyrene scintillator; ii) high-quality WLS and clear fibers; and iii) multi-pixel PMTs.

Figure 9 shows a MINOS custom developed scintillator strip [18] with its WLS fiber located in a 2.3 mm-deep by 2.0 mm-wide groove in the center of the "top"

21

face. The fiber must be completely contained inside the groove to ensure efficient light collection (Sec. 3.8.1). A specularly reflective strip of aluminized Mylar tape is placed over the groove after the WLS fiber has been glued in place. The scintillator surface is covered by a thin (0.25 mm) co-extruded titanium-dioxide (TiO_2)-loaded polystyrene layer that serves as a diffuse reflector. The scintillator and TiO_2 coating are co-extruded in a single process, a standard technique in the plastics industry. The TiO_2 concentration was chosen to be as high as possible without posing extruding problems. In R&D tests the highest concentration of TiO_2 that did not affect the quality of the extruded product was 12.5% by weight, which coincided with the concentration needed to maximize reflection of scintillator light. A 15% concentration was achieved for scintillator production, performed by a different extruding manufacturer. The thickness of the TiO_2 layer was as thin as could be reliably co-extruded and thick enough that ultraviolet light (comparable to scintillator light) could not shine through. Bench tests of light reflection and propagation were well-matched by models [19], with reflection angles following Lambert's law. Absolute reflectivity measurements, known to 1%, were then tuned in the simulation below that level to match observations.
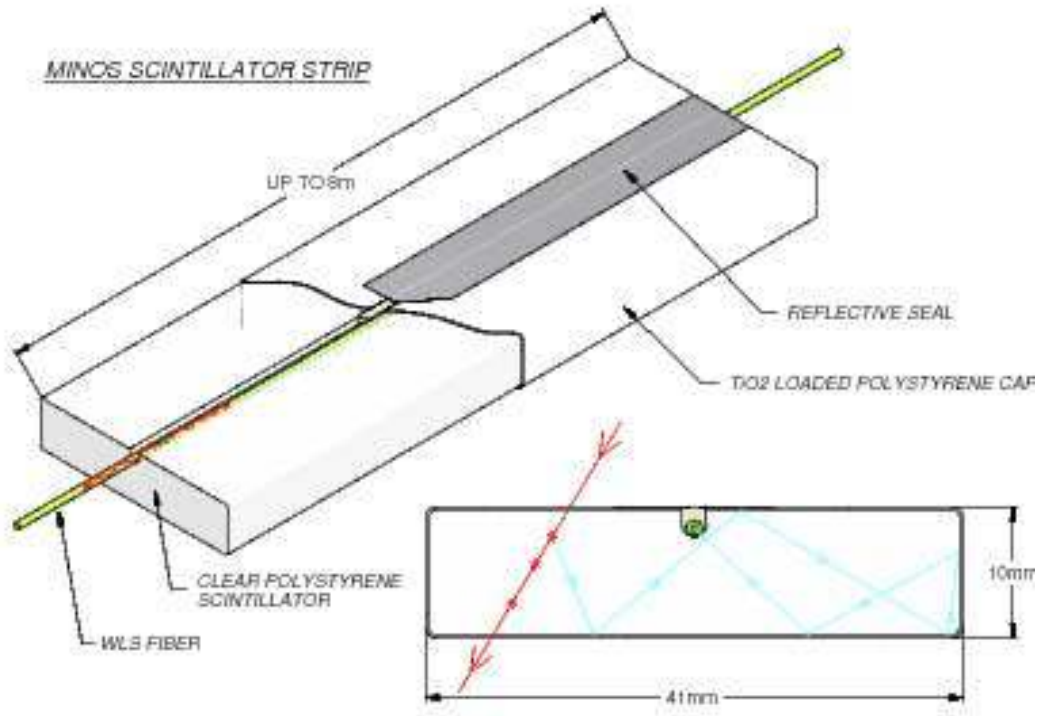

Fig. 9. Cutaway drawing of a single scintillator strip. Light produced by an ionizing particle is multiply reflected inside the strip by the 0.25 mm-thick outer reflective coating (shown in the cross-section view). Light absorbed by a WLS fiber is re-emitted isotropically. Those resulting waveshifted photons whose directions fall within the total internal reflection cones are transported along the fiber to the edges of the detector, subsequently being routed to the photodetectors (Fig. 8).

The procedure used to fabricate the scintillator strips was as follows:

(i) Polystyrene pellets (Dow STYRON 663W) were placed in a nitrogen gas environment to prevent reduction in light yield of the finished product, which would otherwise result from exposure to atmospheric oxygen during the melting process.

(ii) Scintillator fluors PPO (2,5-diphenyloxazole, 1.0% by weight) and POPOP (1,4-bis(5-phenyloxazol-2-yl) benzene, 0.03% by weight) were mixed with polystyrene pellets in a nitrogen gas environment.

(iii) The mixture was loaded into the primary extruding machine, where it was melted and pushed into the main port of the forming die.

(iv) At the same time a mixture of polystyrene pellets and TiO_2 (concentration of 15% TiO_2 by weight) was loaded into a secondary extruding machine where it was melted and pushed into an auxiliary port of the forming die to produce the reflective coating. This material was distributed uniformly around the outer surface area of the strip except for the groove.

(v) A continuous strip, including its reflective coating, exited the die into a sizing and cooling line where its final shape was defined. The strips were then cut to length by a traveling saw.

The diffuse reflector coating is a unique feature developed for MINOS [20]. The co-extruded coating is in intimate contact with the inner clear scintillator; the two are completely fused together, forming a single solid piece. Besides providing the required reflective properties, the coating protects the inner reflective surfaces from mechanical damage, allowing the strips to be shipped with minimal attention to packaging and handling. Two other secondary features of the reflective coating are the protection of the sensitive scintillator from environmental chemical attack and the prevention of deleterious optical coupling by adjoining mechanical epoxies. Tests showed the reflectivity of the TiO_2 loaded coating to be as good as or superior to that of other, labor-intensive candidate reflective materials, such as highly polished surfaces, Bicron TiO_2 paint, or finished surfaces wrapped in Tyvek or Mylar.

Quality assurance feedback is a key component to successful scintillator production. For example, the light output increased by about 20% compared to pre-production test runs when uniform quality-control processes and production extrusion conditions were established. This illustrates that large-scale production runs can help to assure consistent performance for this type of scintillator.

3.3   Wavelength shifting fibers

The WLS fiber is $1.20^{+0.02}_{-0.01}$ mm diameter, double-clad polystyrene fiber with 175 ppm of Y11 (K27) fluor produced by Kuraray, Inc. in Japan. The cladding consists of an inner layer of acrylic and an outer layer of polyfluor. The fiber used in MINOS is "non-S" type, with a nominal S-factor of 25 compared to 75 for some "S-type"

fibers (in which the polystyrene chains are oriented along the fiber direction). The polystyrene core of non-S-type fiber is optically isotropic and more transparent than the core of S-type fiber, resulting in a 10% greater attenuation length. However, the transverse polystyrene chain orientation results in an increased vulnerability to cracking from bending or rough handling.

The fiber was chosen following a series of measurements of light output versus various fiber properties. Fiber from an alternate manufacturer was tested but it did not satisfy our requirements. The final composition of Kuraray fiber was selected to give the highest light output from the far end of the longest scintillator strips (a length of about 9 m of WLS fiber coupled to 3 m of clear fiber). Hence, the long attenuation length properties of the fiber were of particular importance. The fiber diameter was chosen to maximize the coverage of the 4×4 mm^2 PMT pixel by eight fibers.

The fiber was flexible enough to allow delivery on spools of 1 km each, making automated use of the fiber particularly easy. Testing of the fiber was done using blue LEDs in an apparatus that illuminated different points along a fiber wrapped around a cylinder. Production quality assurance tests were done relative to a set of "reference fibers" which had been previously shown to satisfy our requirements. Two fiber samples from each spool, one from the beginning and the other from the end, were taken for testing. Kuraray made similar measurements prior to shipping. In addition, Kuraray provided data on the fiber diameter every 10 cm along its length, automatically recorded during production. A spool of fiber was considered to be acceptable as long as both test fibers had light output of at least 85% of the reference fiber at all locations along it and the spool had only a small (<10) number of spots with diameter variations outside the nominal specifications. MINOS rejected only 3 km out of 730 km of WLS fiber, 0.4% of that delivered.

After installation in the detector, an unexpected level of single photoelectron spontaneous light emission was observed in the WLS fiber. Bench tests [21] confirmed the source of this light and also showed that clear fibers yield negligibly smaller noise rate. This WLS-induced light had an initial rate of several Hz/m (contributing about 1/3 of the single-photoelectron noise rate in the detector) and has decayed exponentially with a time constant of several months.

3.4 Scintillator modules

Integrating scintillator strips into modules provides several advantages. The details of scintillator module design and construction are contained in the following two sections.

3.4.1 Scintillator module design

The packaging of scintillator strips into modules provides the following functionalities:

(i) a mechanically strong structure that holds strips together and which is sufficiently robust for shipping and mounting to the steel plates,

(ii) a light-tight enclosure,

(iii) a package that mitigates the risk of the polystyrene contributing fuel for a fire in the vicinity of the detector,

(iv) a means of connecting of the WLS fibers to clear fibers for transmission of the light signal to the PMTs,

(v) a unit that allowed much assembly work to be done away from the detector sites and still fit into the vertical elevator shaft at the Soudan mine (Sec. 6.4). (The elevator shaft constraints ultimately determined both the length and width of scintillator modules.)

The last 20 cm of the active portion of a typical MINOS module, including a manifold assembly, is illustrated in Fig. 10. The function of each module component is explained below.

The foundations for a module are the aluminum covers, consisting of two flat sheets with formed perpendicular flanges on the left and right sides. The scintillator strips are laminated to the bottom cover by epoxy adhesive, as described in Section 3.4.5. Following lamination, the flanges of the top aluminum cover are nested within the flanges of the bottom cover and the two are then crimped together.

The lamination of the scintillator strips to the aluminum covers provides the basic structural strength of the modules. The crimped flanges complete a light-tight seal around the scintillator strips. Furthermore, the covers implement a fire seal around the strips.

The base manifolds serve to route the WLS fibers from the scintillator strips to the bulk optical connectors. Each fiber is channeled through an individual groove. This design feature eliminates registration errors between the scintillator strips and the optical connector and also protects the fiber ends. The grooves are designed to guarantee that the WLS fiber bend radius exceeds 12 cm despite tolerance stack-up on the extrusions.

The front and back manifold covers shield the WLS fibers in the manifold from ambient light, and fire-seals most of the manifold as well. The light injection module serves two purposes: It enables the implementation of a light injecting fiber calibration system described in Section 5.1 and provides a light seal over the somewhat complex geometry of the manifold in the region of the bulk optical connector. The light-tight washers (Fig. 10) provide alignment references during module construction and installation (Sec. 6.4.6).
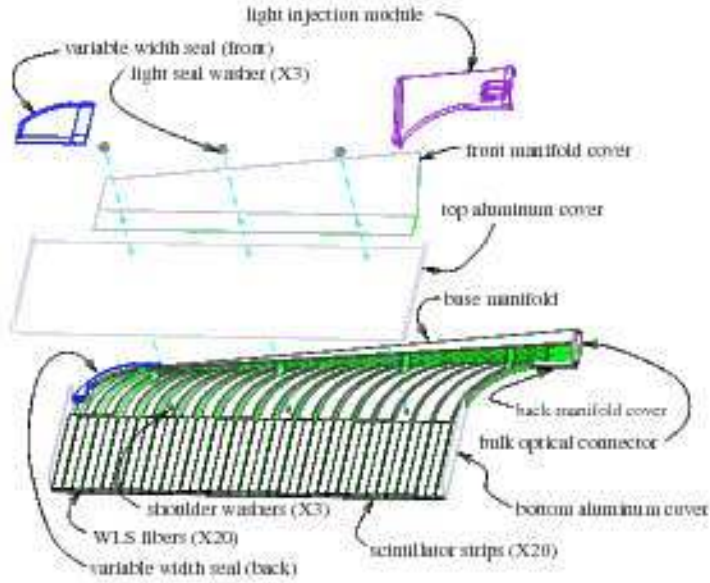
(a) Exploded view.
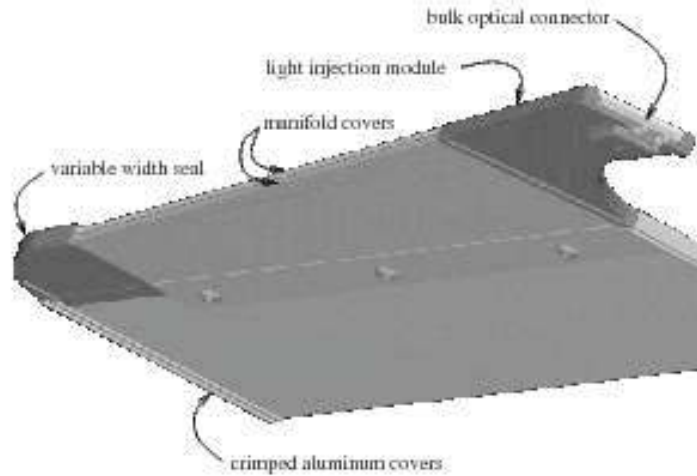
(b) Assembled view.

Fig. 10. A typical MINOS module manifold assembly wherein WLS fibers from the scintillator strips are routed to bulk optical connectors (a) and enclosed by protective light tight aluminum covers (b).

The scintillator strips in each module are close-packed to minimize inactive zones between strips. As a consequence the widths of the modules vary slightly, but by less than 0.5%. The aluminum covers are individually formed to exactly match the cumulative width of the extrusions which they enclose. The variable width seal serves to light seal the gap between the fixed-width manifold parts and the variable-width aluminum covers.

Some scintillator modules must provide clearance for the detectors' magnet coils (for example, see module types D and F in Fig. 11). A semi-circular hole of radius 197 mm is cut into the aluminum covers of the affected modules, and short lengths
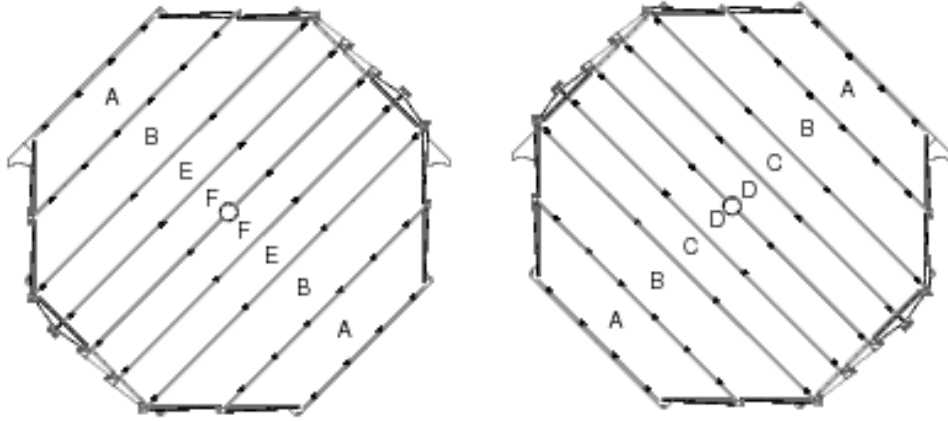
Fig. 11. Layout of U (top) and V (bottom) modules on far detector planes. U- and V-type planes are interleaved. "A" and "B" module types have 28 scintillator strips and the other types have 20 strips. The first (upstream) scintillator plane of each supermodule is of the V-type.

of scintillator strips passing through the hole are also cut away. Due to the rectangular nature of the strips, the region of missing scintillator is larger than the coil hole itself, as long as 598 mm for the most central strips, decreasing in stepwise fashion with each neighboring strip. However, the WLS fibers passing through the affected strips are not cut. Rather, a "bypass" channel routes them around the hole. This bypass protects the fibers from physical damage and ambient light.

Twenty-two variations of MINOS modules were built which all share the basic architecture described here. The layout of modules utilized on different planes of the far and near detectors is described below.

3.4.2 Design of the far detector planes

The far detector utilizes 484 active planes. The layout of eight modules on a far detector plane is illustrated in Fig. 11. Module widths were designed so that no module crossed a vertex of an octagon, thereby simplifying the module-end cuts to either both perpendicular or both 45°.

The far detector required six types of modules to configure the U and V scintillator planes, as shown in Fig. 11. The center four modules are different for the U and V plane types, whereas the outer modules are all the same. The center four modules contain twenty 8 m long strips. The outer modules contain 28 strips varying in length from 3.4 m to 8 m. The ends of all scintillator strips are cut perpendicular to the length of the strips. The strip-ends of the outer modules, whose aluminum covers have 45° ends, follow the edge of the steel plate like steps of a staircase. Each plane has 192 strips covering about 99% of the steel octagon surface.
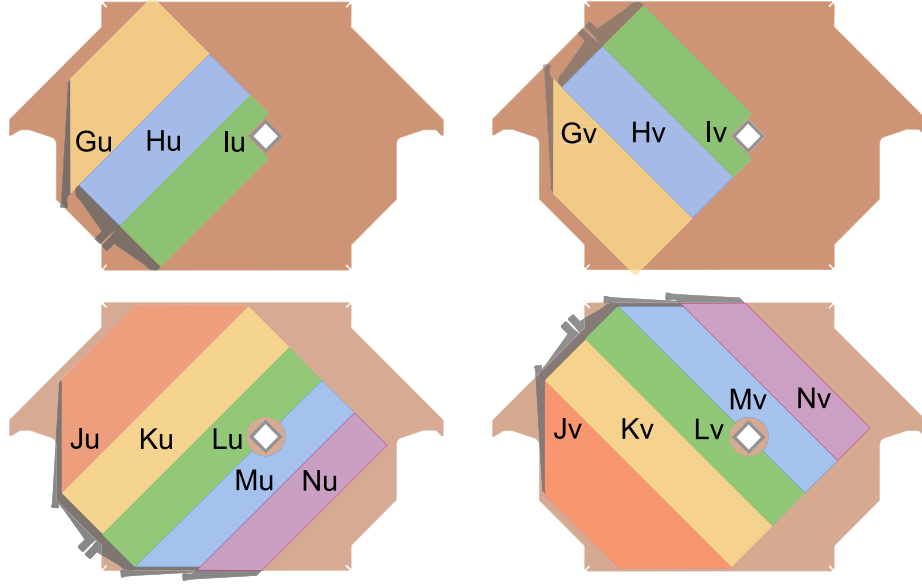
Fig. 12. The four different configurations of planes used in the near detector, showing the different layouts of the scintillator modules. The upper two figures show partially instrumented planes ("calorimeter region") while the lower two figures show the fully instrumented ones ("tracking region"). Strips oriented in the U direction are on the left, and V, on the right. These orientations alternate in the detector to provide stereo readout. The G-N notations denote the different shapes of the scintillator modules. The U and V planes require slight variations on each shape, leading to a total of 16 module types. The beam is centered midway between the coil hole and the left side of the plane, hence the scintillator need only cover that area in the target region.

3.4.3 Design of the near detector active planes

An important distinction exists between far detector and near detector modules. WLS fibers in far detector modules terminate in optical connectors at both ends. WLS fibers in near detector modules terminate in an optical connector on the near end and are mirrored at the far end. Therefore, the far ends of near detector modules are closed with simple plates.

Only 153 of the 282 planes comprising the near detector are active. Active planes are instrumented with four distinct scintillation module patterns: full U-view (FU), full V-view (FV), partial U-view (PU), and partial V-view (PV) (Fig. 12). This required 16 types of modules that contain either 14, 20 or 28 scintillator strips. The area of partial coverage is set to ensure the complete measurement of neutrino events occurring in the near detector fiducial volume. The beam centerline is located at the horizontal midpoint between the left edge of the steel plate and the coil hole, as shown in Fig. 12. The full-view coverage extends around the coil hole in order to track long range muons downstream of neutrino interactions.

The upstream 120 planes of the near detector comprise the calorimeter section and

are all instrumented in order to yield a high resolution view of the neutrino inter-actions. This section was assembled using a repetitive 10-plane pattern: FU-PV-PU-PV-PU-FV-PU-PV-PU-PV. For data analysis, the calorimeter section is divided into three longitudinal sections: planes 1-20 are the "veto" section, used to exclude tracks that originate upstream of the detector; planes 21-60 represent the "target" region, as all neutrino-induced showers which occur here are contained within the length of the detector; planes 61-120 complete the calorimeter section and are used to contain and measure the hadronic showers of neutrino events in the target region.

The spectrometer section of the near detector, planes 121-281, uses the same 10-plane pattern but with partial-view scintillator modules removed. That is, a full-view plane is included in every fifth plane only. This downstream section is used solely to track muons from neutrino interactions.

3.4.4 Scintillator module assembly facilities

The construction of scintillator modules was the single largest production job in the MINOS experiment. The modules were fabricated at three assembly facilities located at collaborating institutions and operated by staff members of those institutions. Twenty-strip wide rectangular modules, types C, D, E, and F in Fig. 11, were constructed at the California Institute of Technology while the 28 strip wide trapezoidal modules (types A and B in Fig. 11) were built at the University of Minnesota, Twin Cities. Each factory produced about four modules per day and each was staffed by a crew of nine technicians working 40 hours per week. Each factory produced a total of about 2,000 modules over a two-year period. At Caltech, the in-house staff was augmented by a number of temporary employees without previous experience building particle physics detectors. The Minnesota facility was mainly staffed by part-time undergraduate workers.

The near detector factory was located at Argonne National Laboratory and was staffed by three Argonne technicians. It produced about 600 modules at the rate of about eight modules per week over a two-year period.

Each module assembly facility was operated under a local manager with oversight by a local MINOS collaboration physicist. The local institution was responsible for worker health and safety but the MINOS construction project provided advice and oversight with the help of Fermilab Environment, Safety and Health (ES&H) professionals. The most significant health issue was the development of worker sensitivity to epoxy vapors during the production start-up phase, apparently initi-ated by skin contact with liquid epoxy, particularly during the gluing of fibers in strips. It was easily mitigated by improved ventilation and the use of gloves and other protective equipment to prevent skin contact with liquid.

The quality of modules produced by all three facilities was excellent. Only a very small number of constructed modules had to be discarded, most due to broken

fibers. After finished modules were delivered to the detector sites, a small fraction were found to have light leaks despite careful light tightness verification prior to shipping. Rapid feedback to the assembly facilities eliminated the causes of this problem, which were primarily transport related stresses at the long seam between the light injection modules and the aluminum module skins. These light leaks were remedied by applying a combination of tape, epoxy, and RTV at the junctions.

3.4.5   *Scintillator module construction steps*

Module components were purchased commercially or fabricated at special purpose facilities operated by the collaboration. The assembly process required a period of four days to complete each scintillator module. Most of this time was needed to cure structural and optical epoxies at different stages of the assembly process. Each module was built on a dedicated assembly support panel which was moved from one assembly station to another by means of roller tables. Assembly facilities were supplied with the following materials to build scintillator modules.

(i) **Aluminum covers.** Rolls of aluminum sheets (0.5 mm thick) were purchased cut to the proper nominal width for assembling the various types of modules. Aluminum sheets were unrolled and cut to length. Because the actual width of every module varied from the nominal due to scintillator strip width tolerances, the long edges of aluminum covers were trimmed with a slitting tool and then bent $90°$ by hand-operated forming tools to accommodate the crimp-sealing procedure.

(ii) **Scintillator strips.** The extruder supplied 8.18 m long strips for rectangular module types C, D, E and F (Fig. 11). They were trimmed to 8.00 m at the module factories. Precut 11.48 m long strips were supplied for the trapezoidal module types A and B. The strips were cut to length in a fixture designed to hold all 28 strips used in one module simultaneously. One end of the fixture had a stop positioned at an angle of $26.57°$ ($\tan^{-1}(0.5)$) relative to the length direction of a module. Positioning the ends of the stock extrusions against this stop enabled cutting all 28 strips to their correct length with a single perpendicular cut. The 11.48 m length was chosen so that the unused portions of the strips cut for a "B" module provided the raw stock for an "A" module, thereby minimizing scrap. Scintillator strips for the near detector were supplied in several lengths due to the larger number of near detector module types.

(iii) **WLS fiber spools**, described in Sec. 3.3.

(iv) **Manifold components**, described in Sec. 3.4.1.

(v) **Bulk optical connectors**, described in Sec. 3.6.

(vi) **Adhesives. Structural:** 3M 2216 translucent two-part epoxy was used to laminate the aluminum skins to scintillator strips. **Optical:** Epon 815C resin with Epicure 3234 teta hardener (in a six to one ratio by weight, respectively) was used to bond WLS fibers into scintillator strip grooves in all modules and to bond the reflective-tape mirrors to the far ends of WLS fibers in near detector

modules. **Manifolds:** 3M DP 810 epoxy was used as the adhesive for the assembly of manifold components, while black GE RTV 103 was used to create light seals at all joints.

(vii) **Tape.** 3M 850 aluminum-coated Mylar reflective tape, 1.27 cm wide, was used to cover fibers in scintillator grooves and as mirrors to terminate the far ends of WLS fibers in near detector modules. Black vinyl electrical tape (3M 33) was used to double-seal certain areas of each module against light leaks. The vinyl tape was covered with acrylic adhesive backed aluminum tape (McMaster-Carr 7631A32, 0.003 in thick) to prevent creeping.

Fig. 13. Scintillator strips and manifolds being vacuum bonded (laminated) to the bottom aluminum cover.

Special equipment, listed below, was used in each of the three assembly facilities. The equipment, designed and constructed at various MINOS institutions, allowed the semi-automatic fabrication and assembly of module components in an efficient and repeatable manner.

(i) **Assembly support trays.** Each module was assembled on a dedicated support tray that measured 1.2 m wide and 9.1 m long. The trays were moved to various stations throughout the four-day assembly process. Support trays were made by joining two 1.2 m × 4.6 m, commercially available, honeycomb sandwich panels, approximately 2.54 cm thick. Support trays were equipped with fixturing holes for aligning the modules and with vacuum ports for the lamination process. During lamination, a polyethylene sheet was placed over the assembly tray and sealed along the tray's perimeter with vacuum sealant tape as illustrated in Fig. 13.

(ii) **Fiber gluing machine.** A semi-automated gluing machine was developed to insert, glue and cover a WLS fiber into each scintillator strip. In one continuous operation, the machine injected optical epoxy to fill the 2.3×2.0 mm

31

groove, inserted the 1.2 mm diameter WLS fiber, pushed it to the bottom of the groove and applied reflective tape to cover the fiber and groove. The fiber gluing machine (Fig. 14) consisted of a head that traversed the length of a stationary table, upon which a partially assembled module was placed. The head carried a glue-mixing dispenser, a spool of WLS fiber and a roll of the reflective tape.

(iii) **Storage rack.** Assembly support trays were placed into storage racks during the (overnight) epoxy curing time. One storage rack could store five support panels, which were loaded by sliding the panels from an assembly station sideways onto a storage shelf. The shelves were raised and lowered by electric motors. The racks were mounted on casters that allowed them to be moved around the assembly facility.

(iv) **Crimping machine.** A manually-operated machine was used to bind the long edges of the lower and upper aluminum covers together. The bent edge of the upper cover was nestled just inside the bent edge of the lower cover. The crimping machine's roller system gradually folded both edges over each other to form a seal as the head, containing 10 crimping stations, traversed the length of the table. The function of each crimping station is shown in Fig. 15.

(v) **Fly cutter.** A custom-built cutting/polishing machine was used to shave the surface of the bulk optical connector and its embedded WLS fibers to produce an optically smooth surface for good light transmission. The machine consisted of an x-y table equipped with a rotating flywheel. The flywheel was driven by a motor with high-quality bearings. The cutting was done by a pair of diamond bits mounted to diametrically opposite sides of the flywheel. Motion along the face of the connector was controlled by a pneumatic drive. The depth of cut was precisely set by manual operator control prior to each pass. A clear shield covering the flywheel protected the operator from getting too close to the sharp, spinning bits when the machine was operating. Figure 16 shows the fly cutter without its clear protective shield.

(vi) **Module mapper.** An automated x-y scanning table was used to measure the response of each module to a 5 mCi ^{137}Cs source. The Cs source was encased in a lead pig that was attached to a traveling x-y scanning carriage with a range of 1.3 m in width and 8 m in length. Optical fiber cables were connected to the bulk optical connector(s) on every module and the transverse and longitudinal response of every scintillator strip was determined. This procedure is described in detail in Sec. 3.8.1

Assembly of scintillator modules was carried out as follows:

Day 1: Cut scintillator strips to proper length; cut and form the bottom aluminum cover; apply structural epoxy adhesive to the inside of aluminum cover. Install scintillator strips and fiber manifold(s) with optical connector(s) inside the epoxied cover. (Figure 10 shows the end of one particular type of module illustrating the details of the scintillator-manifold interface.) Apply sealing compound to the periphery of the assembly support tray and vacuum seal with a polyethylene sheet
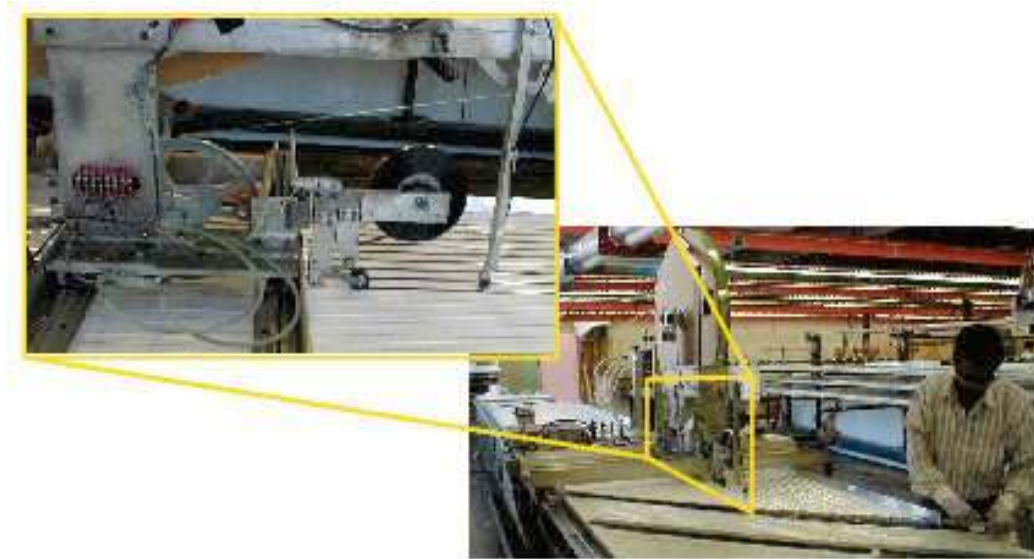
Fig. 14. The WLS fiber gluing machine. The operator threads a fiber through the manifold and into the optical connector while the head moves down the length of the module. The inset shows the moving head which dispenses optical epoxy in the U-shaped groove, inserts the WLS fiber and covers the groove with reflective tape.
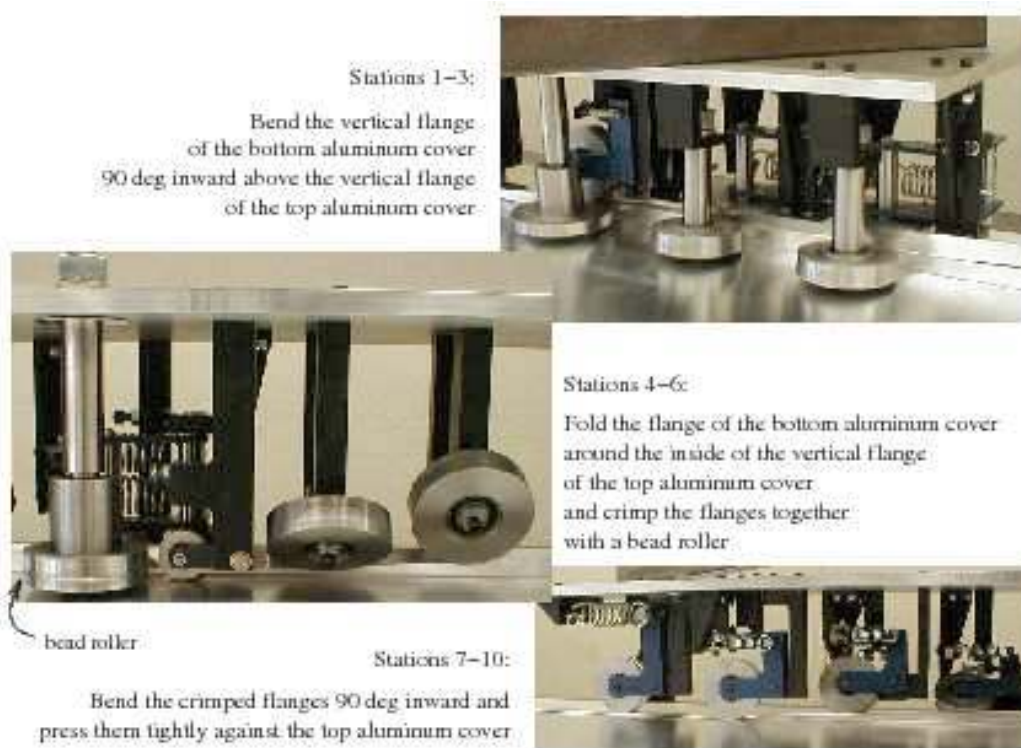

Fig. 15. The 10-station head of the crimping machine. The insets show the function of each set of rollers to form a light-tight seam between the top and bottom aluminum covers of each module. All sharp edges are concealed following completion of the crimp.

Fig. 16. The fly-cutting machine, shown with its safety shield removed for clarity. The flywheel with diamond bits can be seen behind an L-shaped clamping fixture used to hold the optical connector at a precise location. Smooth transverse motion across the optical face is provided by the pneumatic drive located at the lower right in this photograph.

to provide uniform pressure for lamination. (This is shown in Fig. 13.) Move the assembly tray to a storage rack, maintain the vacuum four hours and allow to cure overnight.

Day 2: Move the assembly support tray from the storage rack to the fiber-gluing machine. Remove the polyethylene lamination sheet to prepare the assembly for gluing WLS fibers to the scintillator. Use the fiber gluing machine to apply optical epoxy into the groove, insert fiber to the bottom of the groove, and cover the fiber with reflective aluminized Mylar tape. Extend the WLS fiber ends sufficiently beyond the scintillator strips to route fibers to the optical connector through the guides in the manifold tray.

For near detector modules, apply the aluminum tab to the far end of the scintillator strip and pull WLS fiber through the hole in the tab. Cut the fiber flush against the tab with a heated knife edge. Apply optical epoxy over the cut-fiber end and tab. Place reflective tape across the tab and fiber and secure the tape until epoxy cures. This process produced 1.71 ± 0.02 times the light output of simply polishing the cut end and covering it with a dab of optical grease and black paper. Figure 17 illustrates the mirroring process.

Remove the support tray from the fiber gluing machine and place it in a storage rack overnight to allow time for the epoxy to cure. At the end of each day, pot the fiber optic connectors with optical epoxy (Epon 815C with 2% carbon black additive to prevent light transmission to the fibers).

Day 3: Cut and form the top aluminum cover; apply structural epoxy to the inside of the top aluminum cover. Remove the assembly support tray from the storage rack and place the top aluminum cover over the assembly. Apply sealing compound to the periphery of the support tray for lamination, and vacuum-seal the assembly with a polyethylene sheet. Move the assembly support tray to a storage rack to cure overnight.

Day 4: Move the module from the assembly support tray onto the crimping table. (At this point the assembly tray is placed in a rack to begin assembly of another module.) Crimp the sides of the bottom and top aluminum covers together to form a light-tight enclosure. Flycut the fiber-embedded optical connector to a flat, polished finish. Assemble the manifold and variable-width end seals with 3M DP 810 epoxy and black RTV103 sealant. Cover any RTV with black vinyl tape and cover that with aluminum tape. Move the module to the mapper table. Attach optical fiber cables to the module's bulk optical connector(s) and check for light leaks with a bright hand-held lamp. Repair any leaks and verify that the module is light tight. Use the mapper to measure the response of the module to a series of transverse scans at predetermined longitudinal positions with a ^{137}Cs source to verify the module performs within specifications. Remove the module from the mapper and pack it in a shipping crate.
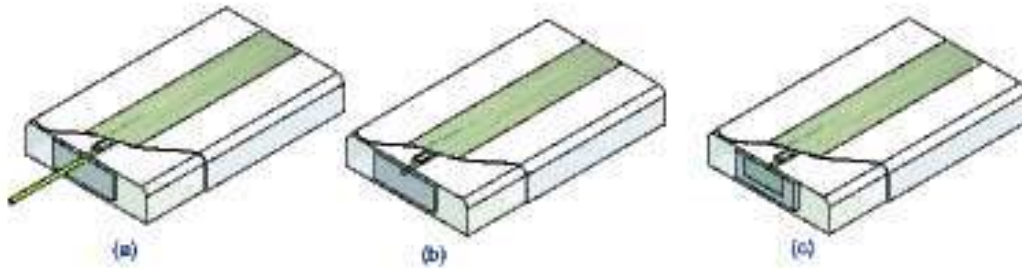

Fig. 17. Mirroring near detector fibers. The WLS fiber is pushed through a hole in the aluminum tab and the tab is glued to the end of the scintillator strip (a). A hot knife is used to cut the fiber flush to the plane of the tab (b). Optical epoxy is applied to the fiber and tab, which are then covered by reflective tape (c).

3.5 Photodetectors and enclosures

The MINOS detectors are read out by Hamamatsu 64-anode (M64) PMTs for the near detector and 16-anode (M16) PMTs for the far detector. The PMTs are housed in light-tight, steel enclosures containing clear fiber bundles which are interlaced from cable connectors to PMT pixels (Fig. 8). In the near detector each M64 resides in an individual enclosure. In the far detector each enclosure (called a "MUX box") houses three M16 PMTs. This box also implements the optical summing (multiplexing) of eight fibers onto each PMT pixel. The fibers are held in place on the PMT face with a precision of 25 μm relative to alignment marks etched by the manufacturer on the first dynode.

Inside a PMT enclosure, each clear fiber from the connector is terminated in a "cookie," a plastic part machined with a diamond-bit fly-cutter to attach fibers to the PMT. Figure 18 shows the mechanical assembly that mates the PMT to the cookie. In addition to keeping the PMTs dark, the MUX boxes shield the PMTs from stray magnetic fields and the base electronics from ambient electronic noise.
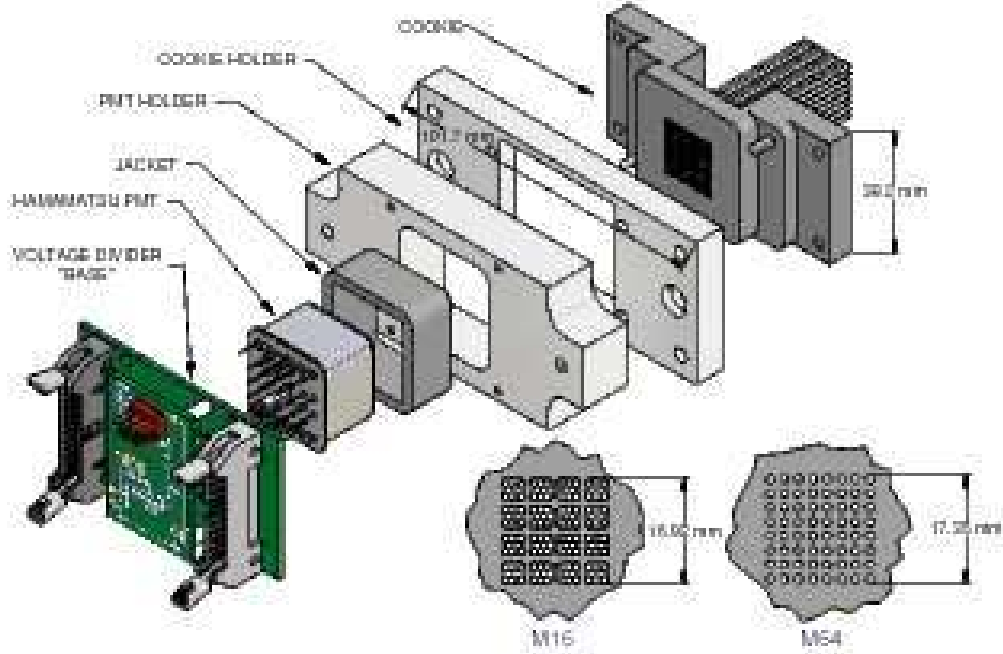

Fig. 18. The M16 PMT mounting assembly, one of three inside each far detector MUX box. The near detector M64 mounting assembly is identical except that only one fiber is placed on each pixel. The fiber "cookie" layouts used in the two cases are shown face-on in the lower right of the figure.

Each PMT has a divider network mounted on a printed-circuit board. This base is designed for a negative potential photocathode and contains the voltage divider recommended by Hamamatsu Photonics. Although the anodes are electrically isolated, only one dynode chain serves all anodes. The base provides a signal from the last dynode, a positive-polarity sum of the response from all the tube's pixels, which is used as a trigger for the PMT readout (Sec. 4.3). In the near detector, this dynode signal is ignored during the beam spill when all anodes are continuously read out (Sec. 4.2).

Each PMT, mounted in its base, was bench-tested before assembly to ensure that it met MINOS requirements for quantum efficiency, gain, crosstalk, linearity, and dark noise [22,23]. The tests showed that for both M16 and M64 PMTs, no crosstalk contribution came from sources external to that particular PMT. The tests demonstrated that the main sources of crosstalk in these PMTs are light sharing between pixels caused by refraction in PMT windows, imperfect photoelectron focusing,

36

Feature	M16	M64
Pixel Gain Variation	Max/min pixel gain <3 rms between pixels 23%	Max/min pixel gain <3 rms between pixels 25%
Quantum Efficiency	>12% at 520 nm	∼12% at 520 nm
Dark Noise (1 p.e.)	∼ 25 Hz per pixel	∼ 4 Hz per pixel
Linearity (typical at nominal gain)	< 5% below 100 p.e.	< 5% below 50 p.e.
PE Crosstalk: (pixels)		
nearest-neighbor	1.92%	2.58%
diagonal-neighbor	0.38%	0.47%
non-neighbor	0.90%	0.69%
total (all pixels)	3.20%	3.74%

Table 1
Main characteristics of the M16 PMTs used in the far detector and M64 PMTs used in the near detector. Further details can be found in Refs. [22,23].

and electromagnetic coupling of dynodes.

3.5.1 Near detector photodetection details

Strips in the upstream 120 scintillator planes of the near detector (the "calorimeter section") are read out individually. In the downstream muon spectrometer section, sets of four anode pads are connected in parallel to reduce the number of front-end electronics channels. The four summed strips are about 1 m apart so that muon tracking is unambiguous. The near detector uses a total of 194 PMTs.

Pre-installation tests of the M64s established the operating high voltage for each tube based upon the requirement of a gain of 0.8×10^6 averaged over all pixels. A typical PMT required ∼800 V to reach this gain.

3.5.2 Far detector photodetection details

In the far detector, there are a total of 484 MUX boxes housing the 1452 PMTs that read out signals from both ends of each scintillator strip. An additional 64 PMTs are used in the cosmic-ray veto shield covering the far detector (Sec. 3.7).

Calibrations established the operating high voltage for each PMT. The requirement was a gain of 1×10^6 for the highest gain pixel on each M16. A typical value of

this setting was $\sim 800\,\mathrm{V}$.

During the detector design phase of MINOS an investigation showed that the uniformity of response over the area of each pixel was sufficient to accommodate eight fibers in a close-packed arrangement and that fiber position shifts as large as $200\,\mu\mathrm{m}$ from nominal could be tolerated. A pixel's eight fibers come from scintillator plane strips separated by approximately 1 m. The fiber assignment on the opposite end of the strips was determined so as to provide an unambiguous 3-dimensional ("demultiplexing") reconstruction of charged particle tracks and showers.

The multiplexing pattern [24] is designed to minimize the effect of crosstalk in the M16s. The demultiplexing algorithm [24] is based on two assumptions: first, the approximate position of a hit along a strip is a function of the ratio of the signal amplitudes at its two ends, and second, on any plane in the detector, the width of an event spans 1 m or less. The algorithm uses information from neighboring planes to choose the overall best solution, including the effect of crosstalk.

3.6   Connectors and cables

Cables of clear fibers transport photons from the WLS fibers (Sec. 3.3) to the MUX boxes (Sec. 3.5.2). The clear fiber from Kuraray has attenuation lengths in the 11–15 m range for green LED light. Except for the 175 ppm fluor concentration in the WLS fibers, the clear and WLS fibers are geometrically and compositionally identical. As a result, at the fiber-to-fiber interface the directions of signal photons are preserved within the total internal reflection angle and none should escape. However losses do arise from mismatching of refractive indices in the coupling medium at the interface and from concentric misalignment of fiber ends. By using an optical couplant (Dow Corning Q2-3067), the transmission loss at each interface was improved from 10-15% to 5-10%.

A finished cable is made of four components, namely clear fiber, connectors, opaque cable conduit, and opaque shroud (injection molded clamshell) which allows conduit to be joined to connector. The various pieces are shown in Fig. 19. The injection-molded Noryl connectors at the ends of cables mate with nearly identical connectors on the module manifolds and MUX boxes. The optical surface of a connector is a linear array of 34 holes, starting and ending with pairs of holes for connecting screws and aligning dowel pins, with 30 fiber holes in between. The center-to-center alignment of fibers holes was measured on a few hundred connector pairs and found to be uniform to better than $30\,\mu\mathrm{m}$. The flexible corrugated black nylon conduit used for light-tightness was a commercial product (Kabelschlepp PRF16/BL). Rare pinholes discovered in the checkout procedure were covered with black vinyl tape. The shroud consists of identical mating custom injection molded clamshell pairs screwed together with the seams sealed with RTV103 (black) silicone rubber.

Fig. 19. Components of a clear fiber cable connector assembly.

Custom made black neoprene rubber bands covered the interface region between mating connectors to complete the light tightness.

3.7 Cosmic ray veto shield

In order to reduce the background in the measurement of atmospheric neutrinos [25] arising from cosmic rays entering the top and sides of the far detector, a veto shield covering these areas was installed. The surface area of the far detector's octagon sides is 40% air gaps, 40% steel plate edges and 20% scintillator edges. Although 80% of the surface area is uninstrumented, most cosmic ray tracks entering the detector through this area have large enough angles to the detector planes that they do not penetrate very far before passing through scintillator. The veto shield was designed to detect all cosmic ray tracks entering the detector, including those that penetrate deep inside before passing through a scintillator plane. It was assembled from 168 of the same C- and E-type scintillator modules used in the main detector (Sec. 3.4.1) and is read out using the same front-end electronics and data acquisition system described in Section 4. Unlike signals from the body of the far detector, however, the veto shield signals are not included in the trigger logic (Sec. 4.3).

The veto shield scintillator strips are aligned parallel to the long (Z) axis of the detector and read out at both ends. Each supermodule is covered by two shield sections, each 8 m long. Since a supermodule is approximately 15 m long, the two

sections overlap by about a meter at the center of the supermodule. Figure 20 shows a vertical cross section through the shield (in the XY plane). The horizontal and diagonal shield sections that cover the top of the detector have two layers of scintillator while the vertical shield modules along the east and west sides of the far detector (known as "walls") have just one. A Monte Carlo simulation [26] shows that more than 99.9% of the cosmic ray muons that deposit energy in eight or more far detector planes produce signals in the veto shield, excepting those which enter through the north and south faces where no veto shield is present.

The output signals from eight adjacent strips are summed together and read out by a single electronics channel on each end. The summing pattern is the same on both ends so it is not possible to demultiplex the hits in the shield in the same way as is done for the body of the far detector. Therefore the transverse hit location resolution of the shield is approximately 12 cm, as calculated by dividing the width of eight 4.1 cm wide strips by $\sqrt{(12)}$.

To reduce false cosmic ray muon tagging that could arise from single photoelectron noise, the dynode threshold is set between one and two photoelectrons. The singles rate in the shield is predominately due to background γ radiation from the cavern walls and noise from the wavelength shifting fibers [21].

A cosmic ray muon entering the detector is identified by a shield signal in time coincidence with an event observed in the main detector. Cosmic ray muons passing through the detector were used to measure the timing resolution of a single hit in the shield to be (4.2±0.3) ns [26]. The inefficiency for tagging cosmic ray muons is dominated by three factors: high singles rates in the shield causing readout deadtime, cosmic ray muons passing through small gaps in the shield, and muon signals falling below the 1–2 photoelectron threshold. The efficiency of the veto shield for cosmic ray muons that stop in the detector is measured to be 95-97%, depending on the the algorithm used [26,27].

3.8 Scintillator performance

The performance of the scintillator system components was optimized during the R&D period and monitored during construction and operation. Section 3.8.1 describes the measurement of strip response in every module prior to installation. The effects of aging in scintillator system components (Sec. 3.8.2) was also measured during the MINOS R&D program. Ongoing performance is monitored continuously during routine experiment operation using cosmic ray muon tracks (Sec. 3.8.3 and 3.8.4).
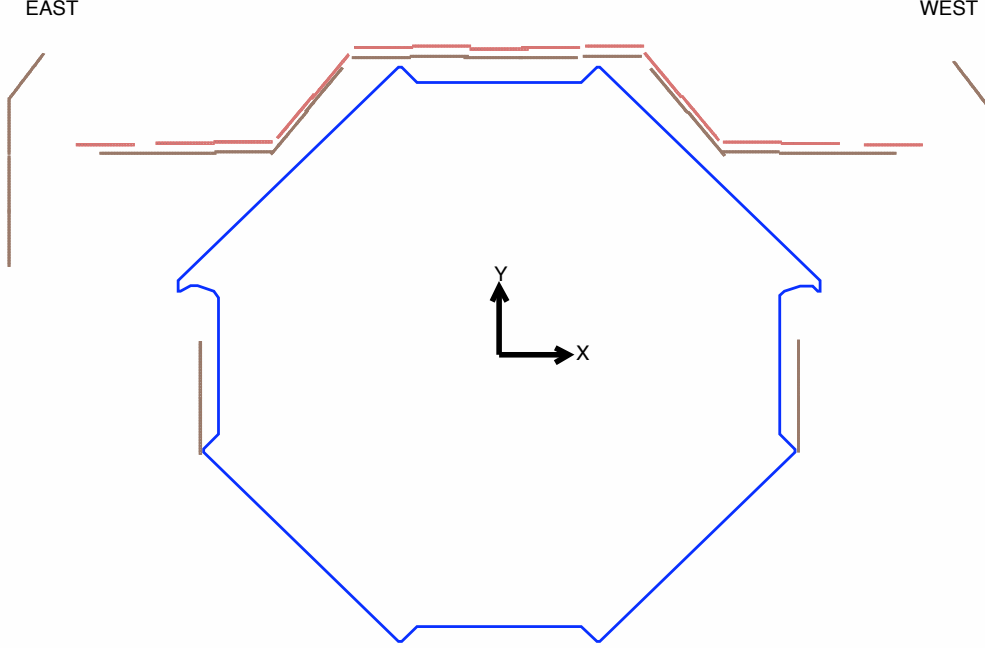
Fig. 20. Schematic of the MINOS far detector veto shield in the XY plane (not to scale). Individual scintillator modules that comprise the shield are shown, including the double layer above the detector.

3.8.1   Module maps

A module mapper was used at each module production facility and at Soudan for quality control and calibration. The mapper used a well-defined γ beam from a 5 mCi ^{137}Cs source (γ energy 662 keV) to illuminate a 4×4 cm^2 square on the scintillator module. A computer controlled x-y drive moved the source across the face of the module. The PMT signal from each strip was integrated for 10 ms once every 40 ms and recorded. This duty cycle was due to the integration of the RABBIT PMA card [28, 29] in current monitoring mode and the limit of reliable readout of the data through the Rabbit-CAMAC-GPIB system. Since the strip thickness is a small fraction of the γ absorption length, the scintillator is fully illuminated. These measurements provided a detailed map of the response of each scintillator module to ionizing radiation. Measurements were made every 8 cm along the length of each strip with a precision and reproducibility of $\sim$1%. Besides providing these pulse height performance calibrations, the locations of the edges of the scintillator strips were determined to a precision of 1 mm by the response curve as the source was scanned transversely across each strip.

Figure 21 shows the mapper's response for a typical strip in a production module. The small variations in the light output from a smooth exponential behavior are real and result from variations in scintillator, fiber depth, and gluing. Figure 22 shows the map for a strip with imperfect fiber gluing (the fiber was not completely

surrounded by the optical epoxy), resulting in local drops in light output due to poor optical coupling between scintillator and fiber. Figure 23 shows a rare example of a strip in which the WLS fiber has a defect within the module, causing poor transmission at one location and a discontinuity in both response curves.
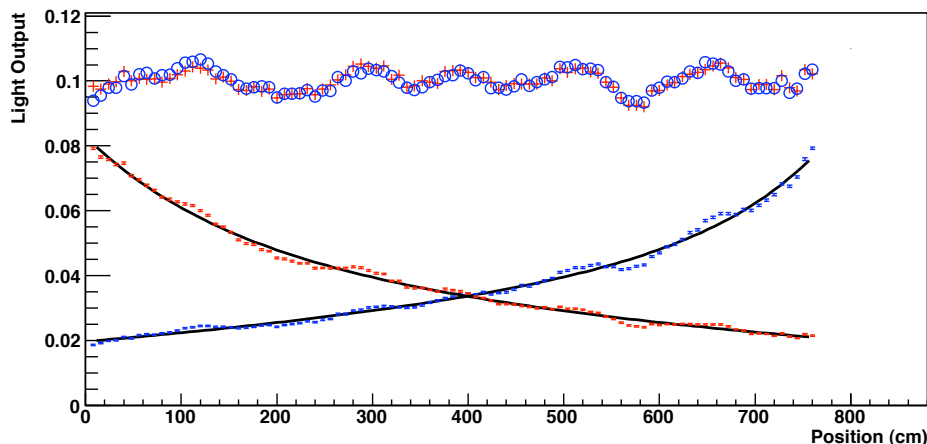

Fig. 21. Module mapping data from a typical far detector module. The lower graphs show responses from each end of a single scintillator strip and their least squares fits to the sum of two exponentials. The responses from the two ends are consistent. The vertical scale was used to compare the absolute light yield of different modules, and is approximately 1/100 of the number of photoelectrons at the PMT for a cosmic ray muon passing normally through the module plane. The top (wavy) series of datapoints shows the ratios of these data to their respective fits, normalized to 0.1 for display purposes.
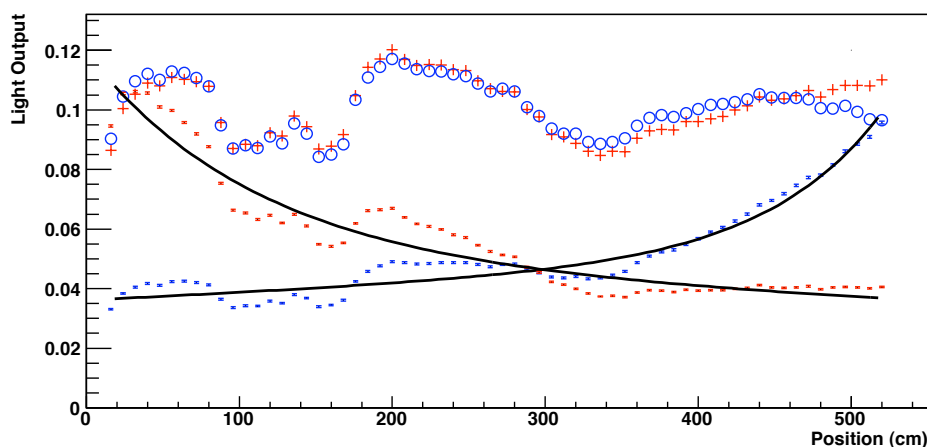

Fig. 22. Mapping data from a module with a badly glued fiber, to be compared to Fig. 21. Bubbles in the nozzle inhibited glue flow in the region of about 100–200 cm and 300–350 cm.

A subset of roughly 1000 modules was mapped at each of the production factories (Caltech and Minnesota) and again at Soudan. Typically the maps taken at the two factories using two different mappers vary by less than 2% at all locations. Larger
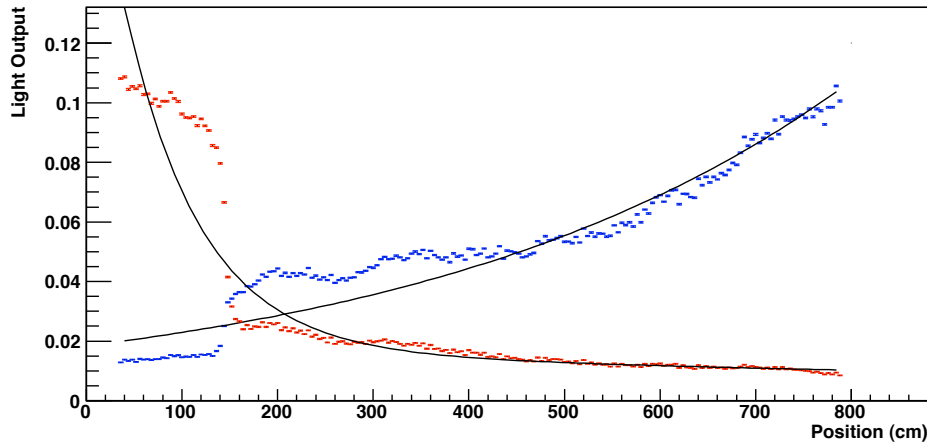
42

Fig. 23. Mapping data from a module containing a rare damaged fiber. The associated strip had a fiber that was damaged at about 150 cm from one end as seen by abrupt steps in the otherwise moderately sloping attenuation curves.

variations could be traced to shipping damage of the epoxy around fibers caused by improper operation of the fiber gluing machine. No properly built module was found to suffer a significant change in light output measured at Soudan compared to that measured at the production factory, with the exception of one shipment that was exposed to -30° C winter weather, which caused some fibers to separate from their strips. Even these few damaged modules were still within nominal acceptance tolerances for use in the detector.

3.8.2 Accelerated aging tests

In order to verify the long-term stability of scintillator light output, several accelerated aging studies were performed:

(i) Tests on small samples of module material were conducted in four different aging environments:
  (a) typical room conditions ($\sim$22° C, relative humidity $\sim$50%);
  (b) 50° C at 50% relative humidity;
  (c) varying temperature from -30° C to +50° C in a 1-hour cycle;
  (d) and 50° C with 100% relative humidity.
(ii) Mechanical stress tests were performed on scintillator strips with fibers glued in place.
(iii) Full-length scintillator modules and clear fiber cables were exposed to four different temperatures for six months: 20°, 28°, 38°, and 50° C.

The most significant results of these tests were:

(i) The scintillator showed a non-reversible reduction in light output with age, associated with yellowing. The change in light output is -1.2%/year at 20° C.

43

(ii) Although optical epoxies typically become visibly yellow with age, the impact on light collection was found to be negligible because there is only a thin epoxy layer between fiber and scintillator.

(iii) The scintillator showed a reversible loss in light output of -0.3%/° C as temperature was raised (but see item (v) below).

(iv) A non-reversible decrease in the attenuation length of the WLS fiber as a function of time was measured. The change in light output at the end of an 8 m fiber was found to be -1.2%/year at 20° C.

(v) Increased temperature resulted in faster aging of the scintillator and WLS fiber. The rate of aging is parametrized exponentially with temperature as $\exp(\Delta T/\tau)$ with $\tau = 10°$ C.

(vi) Temperature cycling (over $>10^4$ cycles) induced no measurable aging effect beyond that caused by the part of the cycle that was above room temperature.

(vii) High humidity combined with high temperature accelerates aging.

(viii) "Normal" mechanical stresses of production, assembly, shipping, and installation had no effect on light output. Extreme stresses can break fibers or strips and exposed fibers are susceptible to cracking (which can significantly reduce the light transmission), but handling with normal industrial practice did not damage fibers in any measurable way.

The overall conclusion is that after 10 years the light output of the MINOS scintillator system will be 65-75% of its initial value. One note of possible importance is that the aging tests were performed on scintillator that had been extruded about six months prior to the aging measurements. Subsequently, other measurements have suggested that the scintillator undergoes an initial drop in light output on the order of 10-15% in the first few months before stabilizing to the behavior reported above.

3.8.3 Variation in light output from module to module

Differences in module light output result from a convolution of variations in several components and in the quality of the construction. Factors include the light output from the scintillator strips, the quality of the WLS fiber, the quality of gluing the WLS fiber into the modules, damage to the fibers, and the quality of finishing the fibers at the connector ends. Figure 24 shows the variation in light output at the center of all far detector scintillator modules as measured by the module mappers. The Gaussian fit has a width of 11% and only 0.16% (317 out of 191,444) have light output less than 50% of the average. Typically the fiber in these abnormal strips had suffered damage during construction.

After correcting for known systematic effects, average photoelectron yields for minimum ionizing particles (MIPs) of installed modules also vary because of differences in transmission at the two connector interfaces, variation in transmission at the PMT interface, and pixel to pixel quantum efficiency variations in the PMT. In addition, different gains of PMT pixels produce further variation in average MIP
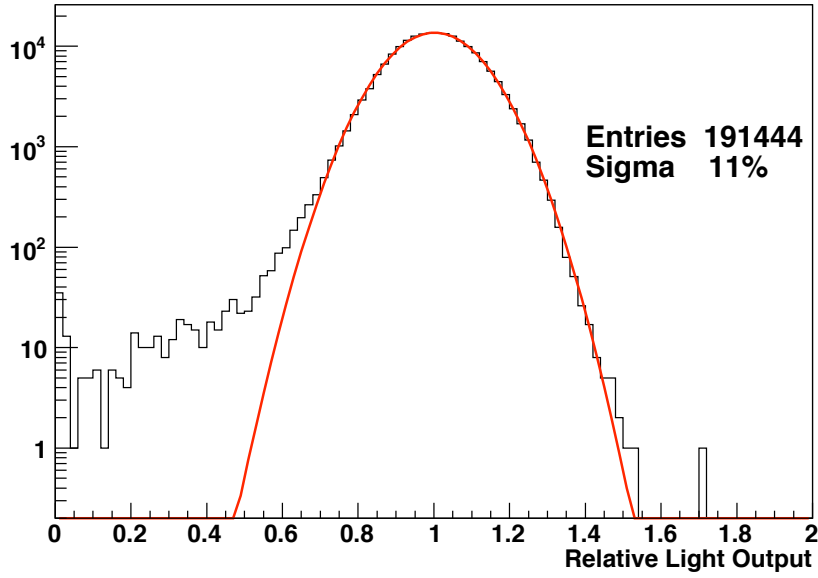
Fig. 24. Distribution of light output from all far detector strips for a 662 keV γ source at the strip center as measured by the module mappers.
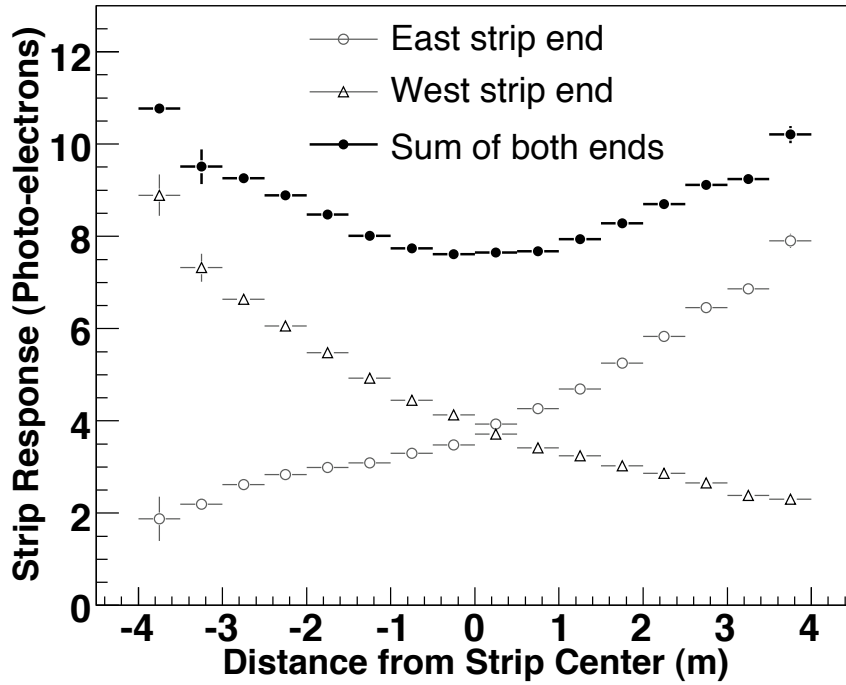

Fig. 25. Average light output from in-situ far detector strips as a function of distance-from–center for normally incident MIPs. The data are from stopping cosmic ray muons, for which containment criteria cause lower statistical precision at the ends of the strips.

45

signal size. The average light yields at strip center for normally incident MIPs in the near and far detectors are about seven and six photoelectrons per plane respectively, summed over both ends. Stopping cosmic ray muons are used as the MIP so their location on the Bethe-Bloch curve in relation to the minimum-ionizing point can be accounted for (Sec. 5.3.2). However, it should be noted that the variation across the face of the detector, both with strip number and along the strip length, is significant. Figure 25 shows the average light output for both ends of the readout for muons crossing at different positions along the strips in the far detector. The data shown are an average from a subset of strips that are all 8 m long and in the U-view planes. The light output varies across the face of the detector because of differing strip and clear fiber lengths. While the signal from one end of a strip varies by a factor of 4-5 along the length of the strip, the sum of both strip ends varies by only $\sim$25%. In the near detector, the relatively short strip length and far end mirrors provide some compensation for the single-ended readout.

3.8.4   Time resolution

The time resolution of the scintillator system was measured using cosmic ray muons at the far detector. The time offsets between readout channels were first calibrated as described in Sec. 5.2.4. The times and positions of the hits on each muon track were then compared and a linear timing fit performed under the assumption that the muons travel at the speed of light. The rms deviation of the measured times from the fitted times was calculated for each muon track. Figure 26 shows the distribution of these rms deviations and a Gaussian fit giving a mean resolution of 2.3 ns.

4   Electronics and Data Acquisition

While considerable care was taken to make the near and far detectors as similar as possible, the same electronics could not be used for the two detectors. The far detector is 700 m underground and the rate of cosmic muons and neutrino interactions is around 0.5 Hz. The data volume is therefore entirely dominated by detector noise of $\sim$ 10 kHz per plane side [21]. In contrast, there are several neutrino interactions per 8–10 μs long spill in the near detector (3.5 reconstructed events per 10^{13} protons on target [4]) . Consequently different requirements led to the design of different electronics systems. To minimize the systematic uncertainties associated with these differences, the response of the calibration detector was measured separately with both near and far detector front-end electronics (Sec. 5.3.3).

The design goals of the electronics and data acquisition systems ("DAQ") are summarized below. The near detector and far detector front end electronics are described separately followed by a section describing the DAQ common to both. Note that the relatively high electrical power used by the near detector front-end
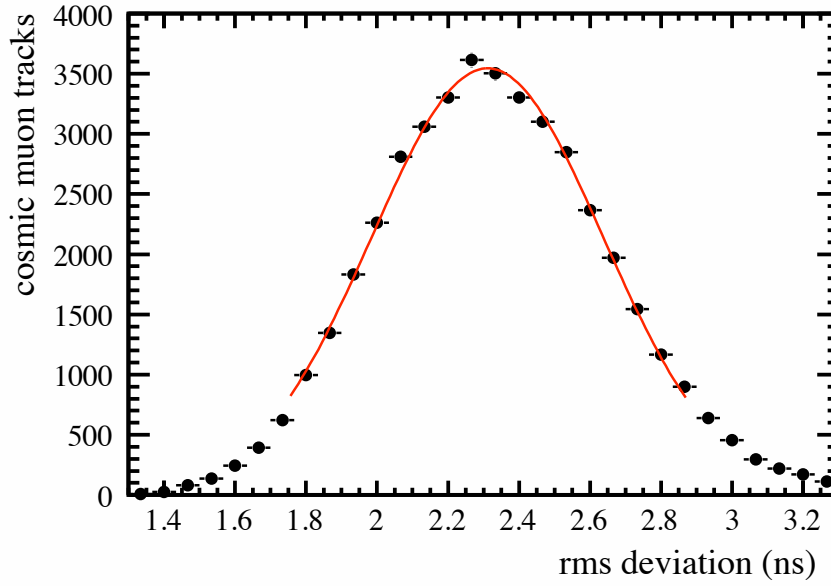
Fig. 26. Distribution of rms deviations from linear timing fits to cosmic ray muon tracks. The data (solid circles) are well-described by a Gaussian distribution (curve) with 2.3 ns standard deviation.

electronics (Sec. 4.2) requires a chilled water cooling system for the racks housing this system (Sec. 6.1). The low-power far detector front-end electronics racks (Sec. 4.3) require only air cooling by rack-mounted muffin fans, as do the DAQ racks (Sec. 4.4) at both detectors.

4.1 Electronics design goals

The primary goals of the electronics are to provide adequate information for the separation of neutral and charged current neutrino interactions and to enable the measurement of the energies of accelerator-neutrino and cosmic ray particle interactions with minimal bias. These goals led to the following specifications:

(i) The electronics should digitize the charge and the time of each pulse from the photodetectors with a (programmable) threshold of 0.3 photoelectrons. The lowest gain pixels in a PMT should have a gain of 3×10^5, requiring the electronics to have a readout threshold of 16 fC.

(ii) A minimum ionizing particle should produce 2–10 photoelectrons at each side of the scintillator strips. This signal has to be measured with a 1–2% accuracy, which requires the least significant bit to correspond to 2 fC.

(iii) Signals can be as large as 25 pC for a high-gain (10^6) PMT pixel. The dynamic range of the system therefore has to be around 12–13 bits.

(iv) The near detector has to separate signals coming from different interactions during the 8–10 μs beam spill. A timing accuracy of around 20 ns is sufficient,

47

given the maximum instantaneous event rate of 20 events per spill, and is coincident with the 53.1 MHz RF structure of the beam. The far detector, however, is also used to study atmospheric neutrino interactions. A timing resolution on the order of 3–5 ns is needed to separate upward from downward going muons or neutrinos.

(v) There should be negligible dead time during the neutrino spill and at least an 80% live time out of spill to record atmospheric neutrino and cosmic ray muon interactions.

4.2 Near detector front-end electronics

In the near detector front-end electronics [30], each PMT pixel is digitized continuously at the frequency of the beam RF structure of 53.103 MHz (18.83 ns). This is achieved with an individual front-end channel unit consisting of a small mezzanine printed circuit board (PCB) called a "MENU". The principal MENU components are an ASIC named the *Charge Integration Encoder* (abbreviated "QIE") [31], a commercial flash analog-to-digital converter ("FADC"), and a data buffer. Sixteen MENUs reside on a VME type-6U PCB (called a "MINDER"), with four MINDERs required for each fully used M64 PMT. An overview of the near detector electronics system is shown in Fig. 27.

The QIE input signal current, I, is split into eight binary-weighted "ranges" with values $I/2, I/4, I/8, \ldots$, and integrated onto a capacitor for each range. A bias current is added to ensure that the capacitor voltage on one and only one range is within the predetermined input limits of the FADC. The QIE selects that voltage for output to the FADC, and also outputs a 3-bit number representing the range value. Four independent copies of the current splitter, integration, and output circuits in the QIE permit continuous dead-timeless operation. The combined information of an 8-bit FADC value and 3-bit range value provide an effective dynamic range of sixteen bits. For the purpose of calibration, an additional 2-bit code allows the identification of the current splitter and capacitor circuit (known as the "CapID") used for each RF cycle.

Data are stored locally on each MENU during a trigger gate and subsequently read out. A beam-spill gate of up to 1000 RF periods (18.83 μs maximum, 13 μs typical) is formed from a signal provided by the Fermilab Accelerator Control Network (ACNET). Outside of beam spills, cosmic ray and PMT singles-rate data are acquired individually for each PMT for 8 RF periods (150 ns) whenever the charge on the dynode exceeds the equivalent of approximately $\frac{1}{3}$ of a photoelectron with a 10 ns shaping time. Charge injection calibration data are acquired using a calibration trigger gate of 256 RF periods.

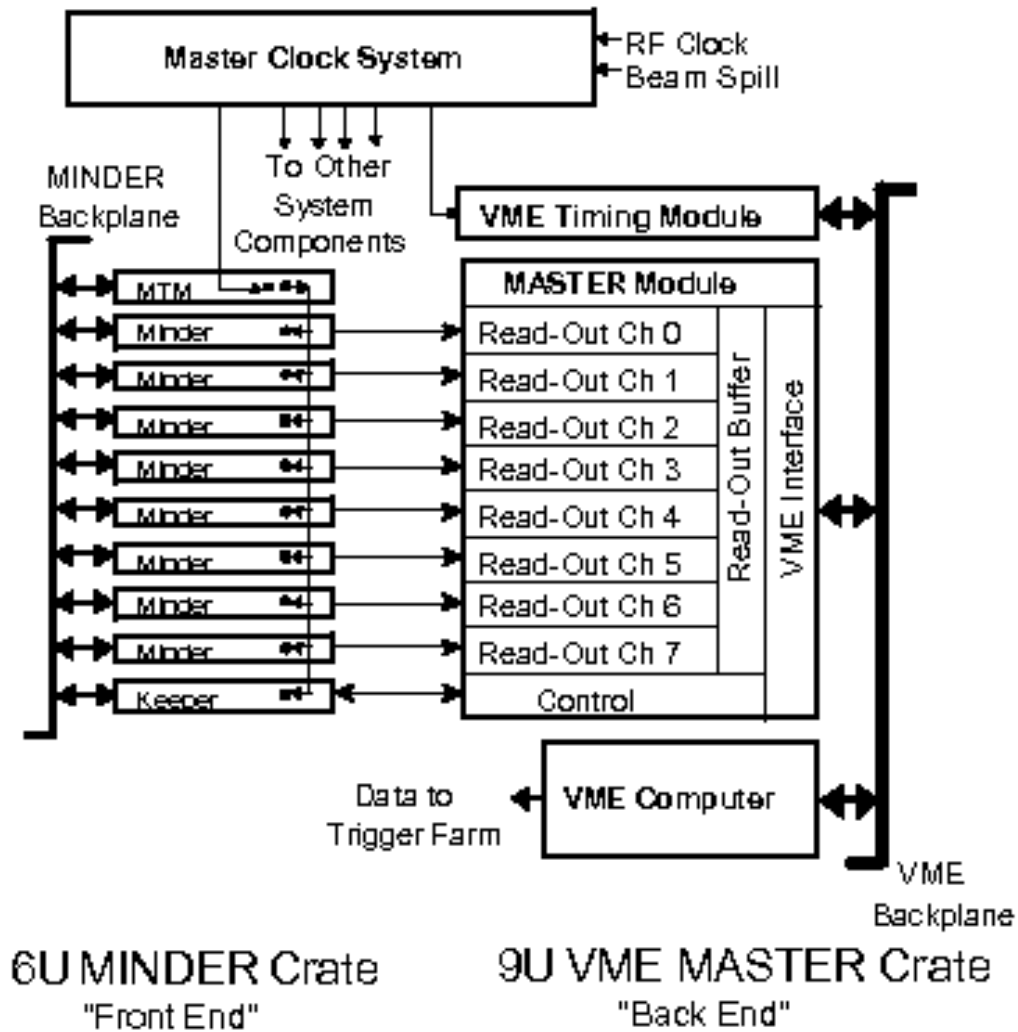At the end of a trigger gate, data are transfered from the front-end to VME type-

Fig. 27. Schematic overview of the MINOS near detector readout electronics. One 64-pixel PMT is read out by four "MINDER" cards. At the end of a trigger, a "MASTER" card in a different VME crate reads out eight MINDERS, applies low-level calibrations, and transfers the resulting data across the backplane to a VME computer, where it is then passed on to a trigger farm for futher processing. The "Keeper" card in the MINDER VME crate distributes trigger signals to the MINDERs, and a clock system keeps all components in sync.

9U modules called "MASTERS", which read out up to eight MINDERS each. A dead-time of ~600 ns is imposed on the front-end for each integration cycle of data read out per MINDER. Given the roughly 1 kHz of dark noise from the PMTs, this yields a typical dead-time of 0.5% in cosmic ray data on a PMT-by-PMT basis. Beam-spill gates supersede the storage and readout of dynode triggered data and therefore suffer no dead-time.

Each data word from the front-end, consisting of range, FADC value, and CapID, is linearized in the MASTER using a lookup table which represents the results of a charge injection calibration of each MENU. The resulting linearity is better

255

ADC
Response
(Cnts)

0

Qin

$\frac{Qmax}{256}$ $\frac{3\,Qmax}{256}$ $\frac{7\,Qmax}{256}$ $\frac{15\,Qmax}{256}$ $\frac{31\,Qmax}{256}$

RANGE 1/2 1/4   1/8   1/16   1/32

Number 0   1   2   3   4

$\frac{2\,Qmax}{256}$ $\frac{4\,Qmax}{256}$ $\frac{8\,Qmax}{256}$ $\frac{16\,Qmax}{256}$
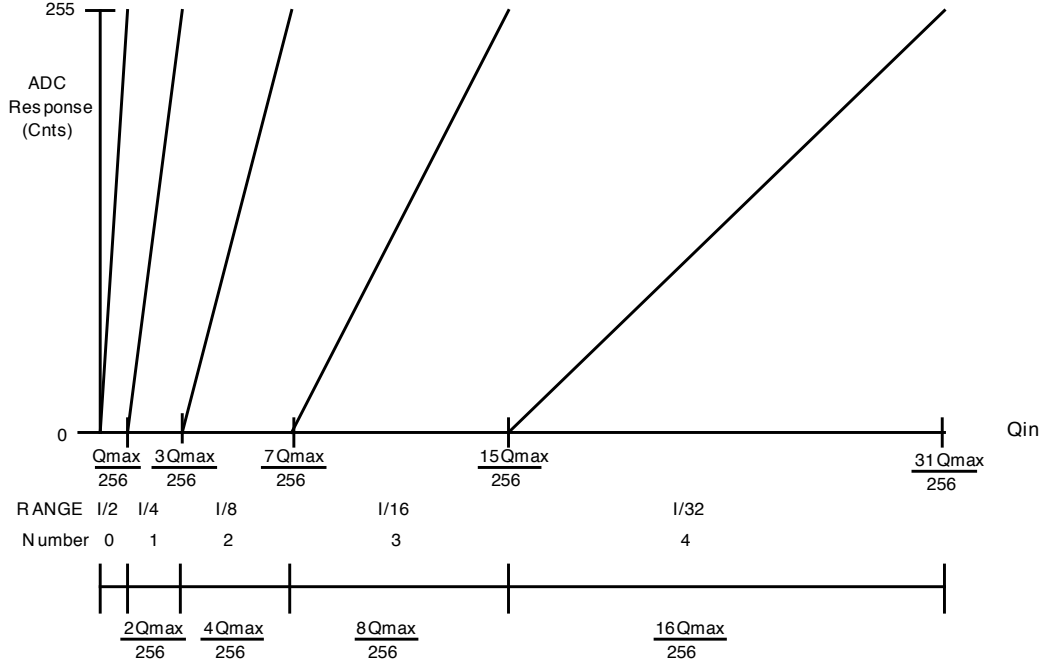
Fig. 28. Response of the QIE-chip based electronics: The x-axis shows the amount of charge injected into the chip, while the y-axis shows the ADC response for the different ranges. Only the first five out of the eight ranges are shown.

than 0.5% over the entire dynamic range. The linearized digitizations exceeding a pedestal suppression threshold of ~20% of a photoelectron are attached to channel-identification and time-stamp data and stored as 64-bit words in a dual-port readout buffer. The buffers are read out every 50 ms in a single DMA block transfer performed by the local VME processor.

To provide uniformity, a centralized near detector clock system is used to distribute a continuous 53 MHz reference, spill signals, and other control signals to all front-end modules. Clock signals are also used to synchronize the readout of data by the VME processors and the DAQ system. The near detector clock is synchronized to the Fermilab accelerator but the phase of timing signals relative to an independent GPS system is used to allow accurate reconstruction of the absolute UTC event time.

4.3 Far detector front-end electronics

The far detector electronics [32] were specifically designed for the low rate underground environment. The neutrino beam generates only a handful of events per day and the cosmic muon rate 700 m underground (2070 m water-equivalent depth) is 0.5 Hz. The signal rate is therefore dominated by detector noise and is 3–6 kHz per PMT. Given this low rate, commercial 10 MHz digitizers operated at less than 5 MHz are able to serve many channels at once and still operate with very low dead

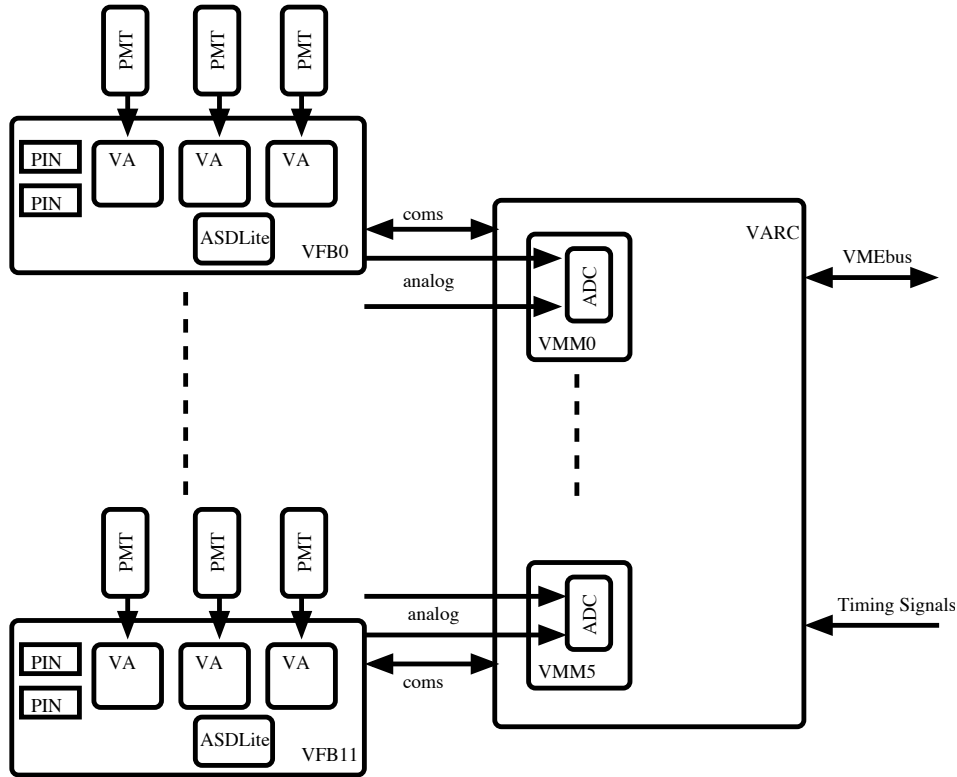time. A block diagram of the readout structure is shown in Fig. 29.

Fig. 29. Schematic overview of the MINOS far detector readout electronics. Three PMTs are connected with short flat ribbon cables to the VFB, which also houses two PIN diodes to monitor the light level of the light injection system. The VA ASIC amplifies and holds the PMT signals, which are multiplexed via an analog link onto an ADC on the VARC. The VFB is controlled through a digital link (coms) by the VARC.

The readout is based on the front-end ASIC VA32_HDR11 (short VA chip), developed in collaboration with the Norwegian company IDEA ASA [33]. Three VA chips are mounted onto the VA front-end board (VFB). There are 32 channels on the chip of which only 17 are used, each channel consisting of a charge sensitive preamplifier, a shaper, a track and hold stage, and an output switch. The output from a selected channel can be switched to a differential output buffer which drives a ∼6 m long cable to a remote ADC. There is a second multiplexer that can route charge to a selected channel for test and calibration.

Three VA chips are mounted on the VFB, located on the outside of the PMT MUX box (Sec. 3.5.2). The VFB provides support circuitry for power distribution and biasing of the VA chips. It also houses the ASDLite [34] ASIC, which compares the dynode signals from the PMTs with a common programmable threshold to provide a discriminated signal for time-stamping and readout initiation.

A serial slow control interface is provided to adjust VA bias levels, enable critical voltage regulators, and monitor voltages and temperature. The VFB is operated in

slave mode and fully controlled by the VA readout controller (VARC) described below.

The MINOS light injection system (Sec. 5.1) monitors the stability and linearity of the PMTs. The light injected into the detector is monitored by PIN (Positive Intrinsic Negative) photodiodes mounted on the VFB. This signal undergoes a pre-amplification and shaping before being fed into a spare channel on the VA chip. The PIN diode signals are read out in coincidence with the PMT signals.

The analog signals from the VA chip are multiplexed onto an ADC, which is located on a VA Mezzanine Module (VMM). Two VFBs are connected to each VMM. The VARC houses 6 VMMs and controls the signal digitization, triggering, time-stamping and bias of the VA chips. Each VARC can thus service up to 36 PMTs of 16 channels each.

The VARC is implemented as a 9U VME card. Three VARCs, a timing card (see below), and a Motorola VME processor share a single VME crate. There are a total of 16 VME crates to read out the 22,000 electronics channels of the detector. The VARC receives the discriminated dynode signal of each PMT. It time-stamps these signals with an effective 640 MHz TDC, implemented in a Xilinx [35] 80 MHz field programmable gate array, and then generates the hold signal for the VA ASIC. The delay time is programmable and is around 500 ns after the trigger signal is received. The signals held in the VA ASIC are then multiplexed to a commercial 14-bit 10 MHz ADC [36], which is operated at 5×10^6 samples/s. The resulting dead time is 5 μs per dynode trigger. The digitization sequence is started if the VARC receives at least two discriminated dynode signals from different PMTs in a 400 ns window. This so-called 2-out-of-36 trigger reduces the dead time due to dark noise in the PMTs and fiber noise in the scintillator, without compromising the recording of physics events.

The system has been tuned such that 1 ADC count corresponds to 2 fC. The electronic noise in the fully installed system is typically around 2.5 ADC counts (5 fC) and changes less than one ADC count over 24 hours. The entire detector readout is synchronized by a 40 MHz optical timing distribution signal slaved to a GPS clock from TrueTime [37].

Once the data are digitized they are transmitted to a local FIFO and stored there for further processing. The pedestal is subtracted and data above an individually set-table sparsification threshold are written to an on-board VME memory. The VARC also controls pedestal and charge injection calibration runs. This memory is read out by the DAQ system described in Sec. 4.4.

The near and far detector data acquisition systems are functionally identical, with appropriate front-end software accommodating the differences of the front-end electronics of the two detectors. The main requirements for the DAQ systems are (*i*) to continuously read out the front-end electronics in an untriggered, dead time free manner and (*ii*) to transfer the data from all front-end modules to a small farm of PCs where software algorithms build and select events of interest and perform monitoring and calibration tasks. The DAQ system allows for diagnostic and calibration data taking runs and can be operated remotely and unmanned. Figure 30 shows the layout of the DAQ system, using the far detector as an example. The system is constructed entirely from commercially available components. A detailed description of the DAQ system architecture and components can be found in [38].

The digitized data in the front-end electronics buffers (time blocks) are read out with single block DMA transfer by a VME computer in each crate, the readout processor (ROP). The ROP is a PowerPC running VxWorks that encapsulates all the readout specific software for the different front-end electronics systems of the detectors. There are 16 ROPs serving the far detector and 8 serving the near detector. The interrupt-driven readout of each ROP (typically 50 Hz) is synchronized by the timing system through local timing system cards in each crate. Each ROP assembles consecutive time blocks in memory into convenient units, called time frames, which are nominally one second in length. The time frames are overlapped by one time block to circumvent processing problems at the time frame boundaries. Each time frame carries a header containing a full self description. Data blocks from monitoring tasks or real-time electronics calibrations carried out in the ROPs are appended to the time frame as necessary.

The transfer of data from the multiple ROPs along the detector uses PCI Vertical Interconnection (PVIC) buses [39] which allow transfer rates of up to 40 MB/s. Groups of ROPs are interconnected with differential PVIC cables to form a chain which is connected by an optical PVIC cable to an off-detector DAQ PC, the Branch Readout Processor (BRP). The near detector is configured with four such chains (termed *input branches*) and the far detector with six. All PCs in the MINOS DAQ system are Intel Pentium-based and run the GNU/Linux operating system.

Time frames are buffered by the ROPs until requested by their BRP. They are then transferred into the memory of the BRP by DMA across the PVIC. One BRP acts as the master, coordinating the transfer of data by issuing transfer instructions to the BRPs. Each BRP is also connected to an output branch, a differential PVIC bus which connects the BRPs to a small farm of trigger processors (the TPs). When a time frame has been successfully transferred to the BRPs, the master BRP selects a TP and instructs each BRP to send (by DMA) its time frame to an address in the TP memory via the PVIC output branch. In this way a full time frame of data from the
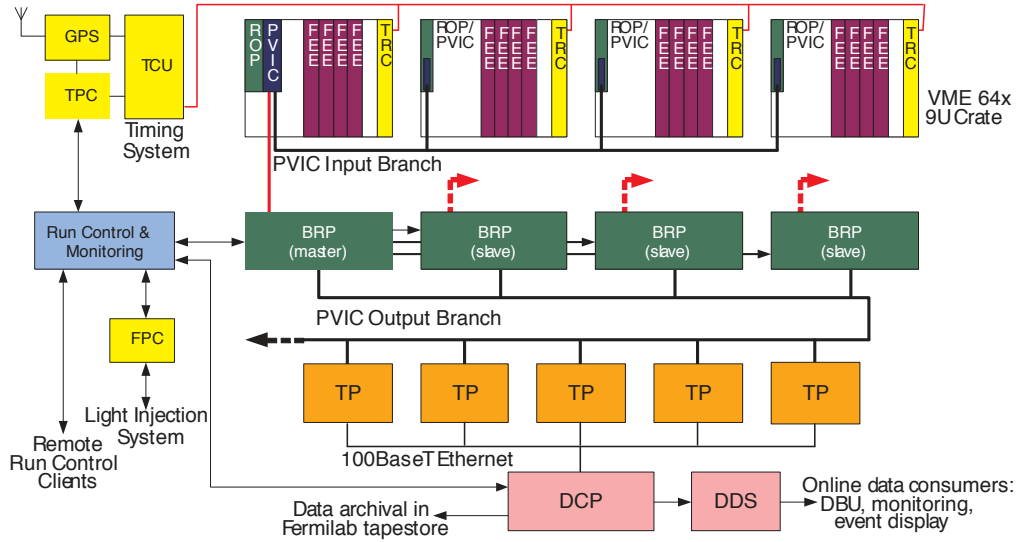
Fig. 30. The architecture of the MINOS DAQ system. The far detector front-end electronics and clock system are shown as an example. For clarity, only one of the six PVIC input branches is completely illustrated, with three more shown in summary.

entire detector is available in a single TP for processing. The TPs, BRPs and ROPs are all able to buffer and queue multiple time frames. Typically, in a physics run the raw data rate into the trigger farm is 8 MB/s at the far detector and 5 MB/s at the near detector. A farm of five 3.2 GHz Pentium4 PCs at each detector comfortably copes with these rates.

After various data integrity checks the TP performs a number of processing tasks on the time frame data. Monitoring statistics, such as data flow rates, are accumulated. Data from the interspersed pulsing of the Light Injection (LI) system (Section 5.1) are identified as LI events and analyzed. Summaries of the detector response to the pulses are generated and output for offline detector calibration.

In parallel with the LI processing, the TP applies software triggering algorithms to the time frame to locate events of physics interest. The primary triggers are summarized below. Since each of these triggers can, in principle, gather multiple events (notably the spill triggers), the output from the trigger is termed a *snarl*. The triggers fall into three categories: special triggers for debugging and calibration, bias-free triggers based on spill signals or spill times to gather beam events, and triggers based on the clustering of hits in the detector to gather out-of-spill events. In this last case, a candidate snarl is first identified as a temporal cluster of hits bounded by 150 ns gaps of detector inactivity. The non-spill-based trigger algorithms are applied to these candidates.

(i) **Spill trigger:** At the near detector, each digitization that occurs within the spill gate is tagged by the front-end electronics (Sec. 4.2). These are identified, extracted from the time frame and output as a single spill event with no further

selection.

(ii) **Remote spill trigger:** At the far detector a direct spill signal is not available so a remote spill trigger is applied. The near detector GPS system is used to generate time-stamps of the spill signals. These are transmitted to the far detector over the internet where they are stored and served to the TPs on request. All readout within a configurable time window around each spill is extracted and written out as a spill-event. Since the DAQ has considerable buffering capability there is ample time to wait for spill information to arrive.

(iii) **Fake remote spill trigger:** Fake spill times are generated randomly between spills to provide random sampling of detector activity.

(iv) **Plane trigger:** M detector planes in any set of N contiguous planes must contain at least 1 hit. Nominally $M=4$, $N=5$.

(v) **Energy trigger:** M contiguous planes of the detector have a summed raw pulse height greater than E and a total of at least N hits in those planes. Nominally $M=4$, E=1500 ADC counts, $N=6$. This trigger is not normally used at the near detector.

(vi) **Activity trigger:** There must be activity in any N planes of the detector. Nominally $N=20$.

(vii) **Special triggers:** A variety of special runs are available to perform detector and electronics calibration or debugging.

The integrated trigger rates at the near and far detectors are typically 4 Hz and 30 Hz, respectively, and are dominated by cosmic rays and noise. The output rate to disk from all sources, including LI and monitoring summaries, is approximately 20 kB/s and 10 kB/s for the near and far detectors, respectively.

All data output by the TP are transmitted via TCP/IP to the Data Collection Process which collects and merges the output streams from all the TPs. The output stream is ordered and formatted as a ROOT tree [40] before being written to disk. The active output file is shared with a Data Distribution System (DDS) which serves the data to various online consumers such as online monitoring and event displays. A data archival task transfers completed data files to the Fermilab mass storage facility by Kerberized FTP over the internet.

Overall control of the DAQ is provided by the Run Control system through a well defined state model implemented by all DAQ components. The system employs a client-server model with a single server controlling the DAQ. Multiple graphical user interface (GUI) clients are used to connect to the server over TCP/IP allowing remote operation. A system of control exchange avoids contention between clients. The GUI client is based on the ROOT framework. This displays the current state and performance of the DAQ as well as allowing the operator to modify the system configuration and control data taking. Automated run sequences are used to facilitate unmanned operation.

4.5   Inter-detector timing

Each of the near and far detectors incorporates a GPS receiver [37] used as a clock for the front-end electronics and DAQ computers. The GPS receivers are located underground and connected by optical fiber to surface antennas. The worst-case resolution of each receiver is approximately 200 ns during normal operation.

The near detector uses the GPS unit to record the time at which Main Injector protons arrive at the target. The far detector similarly records the GPS time of each DAQ trigger. During offline data analysis, after correcting for antenna delays, hardware offsets, and the 2.449 ms time of flight from FNAL to Soudan, these two GPS measurements identify far detector events consistent with beam neutrino arrival times. There is a 64 ns uncertainty on the time offset between the near and far detectors due to uncertainties in hardware delays [41].

Because the far detector does not have a hardware trigger but instead uses software to find events, a system was developed to use the timing information to promptly tag in-spill data. The beam spill is time-stamped at the near detector. The time-stamp is transmitted via internet to Soudan, where this information is served to the event-building software described in Sec. 4.4. A several second buffer of the far detector data makes possible this efficient online time-stamping.

The prompt-time correlation allows for a relaxation of the usual event-building conditions, capturing very small energy events ($\sim$300 MeV). During routine operation the system works reliably to capture 99% of all spills. The dominant sources of inefficiency are temporary network outages and transient network latencies between Fermilab and Soudan.

4.6   Monitoring and control systems

The MINOS Detector Control System (DCS) monitors and controls the experimental hardware and environment. There is a separate but similar DCS system at each detector, each composed of many smaller subsystems.

LeCroy 1440 high voltage mainframes are used to supply the PMTs (Sec. 3.5) with high voltage. Each PMT has its own voltage channel. These mainframes are controlled via a serial link using EDAS brand Ethernet to serial devices, with detector operators using a menu-driven Linux program to manipulate the voltages. A monitoring program reads back both the supply and demand voltage for each channel every 10 minutes and sets off alarms if channels are out of tolerance by more than 10 V (1%).

The currents, voltages and imbalance voltages of the far detector magnet coils

(Sec. 2.3) are monitored and controlled via a National Instruments (NI) "Field-point" unit, using a Windows XP machine and NI's "Measurement Studio" Visual Basic libraries. The near detector magnet is controlled via Fermilab's ACNET control and monitoring system; the DCS merely reads its ACNET status and passes on the information. At both detectors, thermocouples (type FF-T-20) monitor the temperature of the coils and the steel, providing an additional software thermal cutoff.

A number of different environmental parameters are monitored by the NI Field-point system: barometric pressure (Omega PX2760-20A5V transducers), temperature and humidity (NovaLynx 220-050Y probes), radon levels (Aware RM-80 monitors), and thermocouples (also used to monitor the coil heat dissipation as discussed in Sec. 2.3) located in all the high-power near detector front-end electronics racks and in several key locations within the cavern (Sec. 4.2). At the far detector, the control panel for the cavern chiller supplies information on its components, as does ACNET for the near detector cavern pumps.

The status of the electronics racks is monitored and controlled by BiRa RPS-8884 Rack Protection Systems (RPSs). Each rack has an RPS, which gets inputs from in-rack smoke detectors, temperature and air flow sensors, fan pack failure status transistors, coolant drip sensors, and DC low-voltage monitoring. If any of these parameters is out of tolerance, the RPS sets a warning bit, read out via a Linux daemon over Ethernet to allow preemptive maintenance. If any parameter exceeds an upper tolerance level, or the RPS detects a serious hardware problem like smoke or a water leak, the RPS drops the AC voltage permit signal, power to the rack is cut and alarm bits are set on the network. Additionally, the VME crate power supplies have a CANbus interface, allowing the monitoring of the voltage and currents supplied to the VME-based electronics. This interface also allows power supplies to be shut down by operators or the monitoring software.

All DCS data sources send their information to a MySQL database at each detector. Status web pages are generated from these databases and alert shift-workers when something is out of tolerance. The contents of these databases are archived as ROOT files as well as copied to the master MINOS database for offline use in later data analysis and calibration.

5 Calibration

The MINOS detectors measure hadronic and electromagnetic shower energy by calorimetry. The relative detector energy calibration is critical for neutrino oscillation studies that rely on comparisons of energy spectra and event characteristics in the near and far detectors. A calibration system is used to determine the calorimetric energy scale and to ensure that it is the same in the near and far detectors. Because MINOS is intended to measure Δm_{32}^2 to an accuracy of better than 10%,

shower energy scale calibration goals were set at 2% relative systematic uncertainty and 5% absolute uncertainty.

This section describes the calibration of the responses of the near, far and calibration detectors. This calibration corrects for scintillator light output variations as well as nonuniformities of light transmission and collection in the fibers, PMTs, and readout electronics. Section 5.1 details how the optical light-injection system is used to measure the linearity and time variation of the readout response in all three detectors. Section 5.2 outlines the use of cosmic ray muon tracks to measure scintillator strip light output variations with time and position, specifically to record interstrip and intrastrip nonuniformities. In addition, Sec. 5.2.4 describes the use of cosmic ray muon data to measure the fast time response of far detector scintillator strips, used to distinguish up-going from down-going cosmic ray muon tracks. Section 5.3 provides a detailed description of how the relative and absolute energy scales of the near and far detectors are determined using cosmic ray muons and calibration-detector data from charged particle test beams.

The calibration uses both the optical light-injection system, which measures the behavior of the readout instrumentation, and cosmic ray muon tracks, which measure the response of the scintillator. This calibration is a multi-stage procedure that converts the raw pulse height $Q_{\mathrm{raw}}(s, x, t, d)$ in strip s, position x, time t and detector d into a fully-corrected signal Q_{corr}. Each stage applies a multiplicative calibration constant:

$$Q_{\mathrm{corr}} = Q_{\mathrm{raw}} \times D(d, t) \times L(d, s, Q_{\mathrm{raw}}) \times S(d, s, t) \times A(d, s, x) \times M(d) \quad (1)$$

where

D is the drift correction to account for PMT, electronics, and scintillator response changing with temperature and age.

L is the function that linearizes the response of each channel with pulse-height.

S is the strip-to-strip correction that removes differences in response, strip-to-strip and channel-to-channel.

A is the attenuation correction, which describes the attenuation of light depending on event position along each strip.

M is an overall scale factor that converts corrected pulse height into the same absolute energy unit for all detectors.

The data collected with the calibration detector at CERN [5] are used to determine the absolute calibration of the detector energy response by comparing the calibrated shower energy to the known energies of the particle beams.

Two additional calibrations are required. First, a strip-by-strip timing calibration is performed on the far detector data, primarily to aid in reconstructing the directionality of cosmic ray muons and atmospheric neutrino events. Second, the PMT

single-photoelectron response is determined in order to adjust for PMT thresholds and cross-talk.

5.1 Light injection system

The light-injection system [42, 43] is used to map the linearity of the instrumentation, to monitor the stability of the PMTs and electronics over time, to evaluate the single-photoelectron gain, and to monitor the integrity of the optical path and readout system. Nearly identical systems are used for the near, far and calibration detectors.

The light-injection systems use pulsed UV LEDs to illuminate the WLS fibers of scintillator modules. The LEDs are housed in rack-mounted "pulser boxes," each containing a set of 20 or 40 LEDs. Optical-fiber fan-outs allow each LED to illuminate multiple fibers through a set of optical connectors on the back panel of each pulser box.

From the pulser boxes, optical fibers carry the light to scintillator module manifolds on the outer surface of the detector. Highly-reflective cavities in the manifolds, called light-injection modules (LIMs), allow the LED light to illuminate the WLS fibers, as shown in Fig. 31. The light injection pulses mimic scintillation-light signals from scintillator strips. The intensity of this injected light is monitored by PIN photodiodes that are read out simultaneously with the detector PMTs.
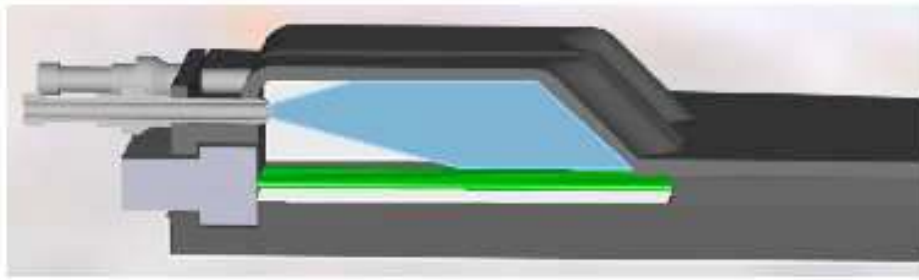

Fig. 31. A cutaway view of the light-injection module. A curtain of up to ten green WLS fibers runs across the bottom of the LIM cavity, and the injected light illuminates them from above. The T-shaped component at the lower left is the bulk optical connector into which the WLS fibers are glued. In the upper left foreground is a cutaway of one of the connectors terminating the light-injection fibers; another connector is visible behind it.

5.1.1 Gains and instrumentation drift

During data taking, the light injection system periodically pulses the fiber at every strip end to monitor the stability and gain of every channel. Each far-detector strip end is pulsed about 300 times per hour and every near-detector strip end is pulsed

1000 times per hour. The pulse intensity is tuned such that a PMT pixel receives approximately 50 photoelectrons per pulse. Variance in injection fibers, readout fibers, and PMT efficiencies are such that some pixels receive up to a factor of two more or less illumination than the average. LED pulses are monitored by PIN diodes to correct for drift in LED intensity over time.

These light injection data provide corrections for changes in gains of PMTs and electronics as well as for other transient instabilities. Experience has shown that good environmental control eliminates most short-term variations in the instrumentation response, but long-term studies reveal slow drifts in the response, perhaps caused by seasonal environmental changes and aging effects, equivalent to changes in detector gain of $\lesssim 4\%$ per year.

To track these variations, the data from each month are collated and used to compute the average response per photoelectron per channel. This is done using photon statistics [5,22]. By comparing the rms widths of many pulses to the mean, the number of ADC counts per photoelectron is found for each channel. Figure 32 shows the results from one such calibration. The offline software uses these "gains" for Monte Carlo simulations, cross-talk identification, strip counting efficiency, and other reconstruction tasks.
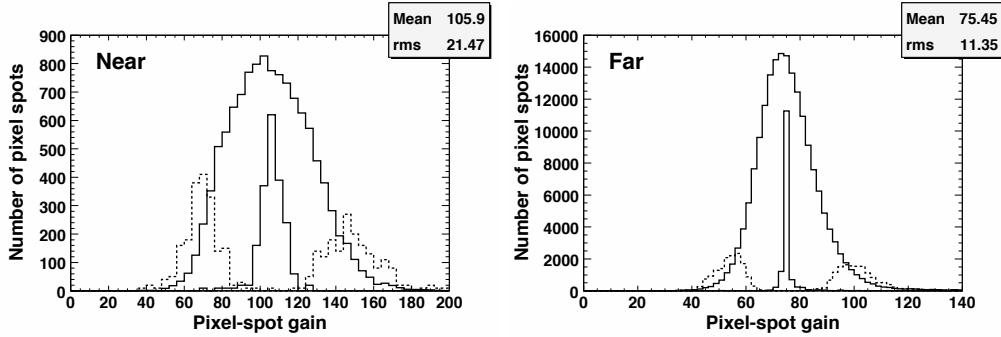

Fig. 32. Gains measured by the light injection system for the near (left plot) and far (right plot) detectors. The solid line histograms show the gains for all channels (broad distribution) and the mean gain per PMT (narrow distribution). The dashed-line histograms are distributions of the minimum and maximum pixel gains for all PMTs.

5.1.2 *Linearity calibration*

The light injection system is also used to map the nonlinearity of PMT response. The PMTs become ~5–10% nonlinear at light levels of approximately 100 photoelectrons [22,23]. In addition, the far detector electronics have a nonlinear response of similar scale, so it is convenient to linearize both components with a single correction. To this end, light is injected into the scintillator modules in steps that cover the range from a few to hundreds of photoelectrons.

During experiment operation, gain data are collected once a month at both near

and far detectors, interspersed with normal physics data taking. Each scintillator strip-end fiber is pulsed 1000 times at many different light levels. The pulse height settings for each LED are tuned so that the average response of the strips connected to it covers the full dynamic range of interest. Two PIN diodes, one amplified with high gain and one with low gain, monitor the stability of the light output of each LED. Low-gain PIN diodes are better suited for large light levels where saturation of the PIN readout electronics might occur. At lower light levels, the high-gain PIN diodes provide a better signal. Extensive test stand studies have shown the response of the PIN diodes used in MINOS to be linear to 1% [42] over a dynamic range roughly corresponding to 5-100 PMT photoelectrons.

These data are used to parametrize PMT response as a function of true illumination. The linearity correction, applied offline, is determined by extrapolating PMT response in the linear region to the nonlinear region. This is accomplished by mapping PMT response as a function of either of two PIN diodes or a combination of both. For the far detector, both ends of each strip are read out, but light is injected into only one end at a time. Light on the distant end is substantially attenuated and therefore in the linear region of the response curve, giving an independent measurement of the true illumination.

Although the PIN diodes themselves are measured to be quite linear, it is difficult to verify the linearity of the PIN diode readout electronics. Nonlinearities on the order of 1-2% are apparent in the data from both detectors. In the near detector, noise from the PIN amplifier was exacerbated by the characteristics of the sampling readout. In the far detector, problems were suspected in the analog electronics where cross-talk from PMT signals may have contaminated the PIN signals.

Figure 33 shows the results of the nonlinearity calibration. The far detector nonlinearity is measured with the distant-end technique, while the near detector nonlinearity is measured by the PIN diodes. The near detector PMTs become nonlinear at low pulse height, while the far detector readout electronics saturate at high pulse height. Low pulse-height data from the near detector (not shown) are unreliable due to PIN readout difficulties.

The flexibility of the system provides additional information for detector debugging. High- and low-gain PIN diodes have independent light paths to the LED and are used to diagnose problems related to the LED. The near and far strip-end readouts at the far detector provide an independent way to identify problems with the PMT and front-end electronics.

5.2 *Cosmic ray muon calibrations*

Cosmic ray muons are used at each detector to measure scintillator related quantities. Throughgoing cosmic ray muons have an average energy of $\sim 200\,\mathrm{GeV}$ at
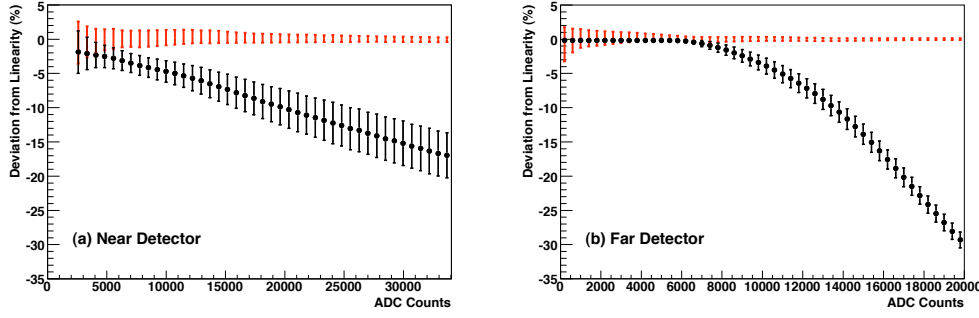
Fig. 33. Nonlinearity calibration of near and far detector instrumentation. The intrinsic nonlinearity of PMT response (circles) and its residual after calibration (error bars only) are shown for the near (a) and far (b) detectors. The error bars depict the rms spread of channels in each detector. For scale, a minimum ionizing particle normal to the plane will generate roughly 500-600 ADCs of charge each detector. A single photoelectron is roughly 75 ADCs (Far) or 100 ADCs (Near).

the far detector and a rate of $\sim$0.5 Hz. At the near detector, the mean energy is $\sim$55 GeV and the rate is $\sim$10 Hz.

Stopping cosmic ray muons, clean examples of which which constitute 0.3% of the total cosmic ray events recorded at the far detector [44], are used for absolute energy calibration.

5.2.1 Measurement of time variations

Although the light-injection system measures the time variations of PMT and electronics responses, the scintillator and WLS fiber cannot be monitored in this way. The changes in scintillator and WLS fibers caused by temperature variations and aging are described in Sec. 3.8.2. These are monitored with cosmic ray muons to correct for small changes in the detector response over time.

Cosmic ray muons are used to track the response of each detector on a daily basis. This "drift" calibration is performed by measuring the total pulse height per plane of through-going cosmic ray muons. Although the energy deposition of these muons is not the same at each detector and also depends on zenith angle, the average energy deposited at each detector site is expected to be constant with time. The daily median of the pulse height per plane is computed, and the relative change in this quantity is used to compute the drift, $D(d, t)$:

$$D(d, t) = \frac{\text{Median response}(d, t_0)}{\text{Median response}(d, t)}.$$

(2)

This measured drift encompasses changes due to the scintillator, WLS fiber, PMTs and electronics.

Figure 34 shows the results of detector drift measurements over several years of operation. The data show that the far detector drifts at a level of $\sim 2\%$ per year. The near detector appears more stable initially, later showing a downward drift. While the long-term decrease in detector response can be attributed to aging of the detector components, the short-term response changes are well correlated with temperature variations. During the summer 2006 shutdown the high voltages supplied to the far detector PMTs were retuned, causing a rise in the detector response.
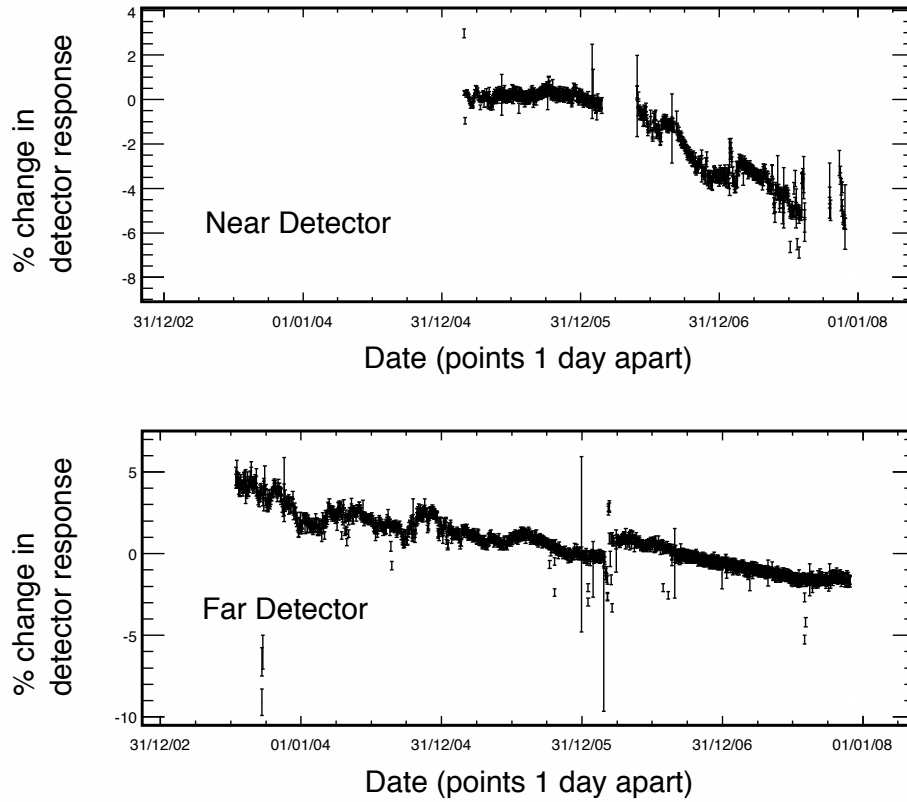

Fig. 34. Drifts in the responses of the near (top) and far (bottom) detectors. Each point is the percentage drift of one day's data from an arbitrary zero point of the daily median pulse height per plane of through-going cosmic ray muons. The errors bars show the rms spreads of the daily pulse heights per plane. The gap in the data corresponds to the summer 2006 shutdown.

5.2.2 Strip-to-strip nonuniformity calibration

Throughgoing cosmic ray muon data are used to measure the strip-to-strip (channel-by-channel) time dependent response of the detector, $S(s, d, t)$. This calibration relates the mean response of each strip end to the detector average:

$$S(s, d, t) = \frac{\text{Mean Response of Detector}(d, t)}{\text{Mean Response of the Strip End}(s, d, t)} \tag{3}$$

63

The normalization incorporates several detector effects that vary channel-by-channel, including scintillator light yield, WLS collection efficiency, readout fiber attenuation, PMT quantum efficiency and PMT gain. Although some of these effects can be measured and corrected for independently, it is convenient to include them in a single correction.

Cosmic ray muon tracks are used to measure the post-linearization mean light level at each strip end. To remove known spatial and angular dependencies, attenuation and path-length corrections are applied to each hit such that the calibration constant is calculated to be the mean response of a muon of normal incidence traveling through the center of the strip. A statistical approach is used to estimate the frequency that a track may clip the corner of a scintillating strip [45]. Due to the low light level at the PMT face, ~2–10 photoelectrons, the mean-light level calculation must account for the Poisson probability of producing zero photoelectrons. The spatial resolution of the detectors is not sufficient to predict missed strips from event topology, so an iterative technique is used to estimate the most probable light yield of a strip. This is used to calculate the zero contribution probability [46].

The stability of this technique has been verified through the comparison of two separate data sets spanning the same time period. Specifically a one month period in the near detector (two weeks equivalent per data set or ~2400 hits per strip end) was compared to a four-month period in the far detector (two months equivalent per data set or ~760 hits per strip-end). Figure 35 shows the relative response of each strip end ($1/S(s, d, t)$) in the near detector. The mean responses of the strip ends vary by approximately 29% from the detector average. The statistical variation in the calibration values determined with each data set is on the order of 2.1%. The mean responses of individual strip ends in the far detector also vary by 30%, with the calibration values stable to within 4.8%.

5.2.3 Wavelength shifting fiber attenuation correction

Cosmic ray muon data could be used to correct the variation in light caused by attenuation along the WLS fiber in a scintillator strip. However, it is more accurate to calculate calibration constants from the module mapper measurements described in Sec. 3.8.1. These data are fit to a double exponential:

$$A(x) = A_1 e^{-x/L_1} + A_2 e^{-x/L_2} \qquad (4)$$

where x is the length along the strip and L_1, L_2 stand for two attenuation lengths. A fit is performed for each strip and the resulting parameters are used to correct the data.

The attenuation constants were subsequently checked using through-going cosmic ray muons. The pulse height from a strip hit by a track is plotted as a function of the
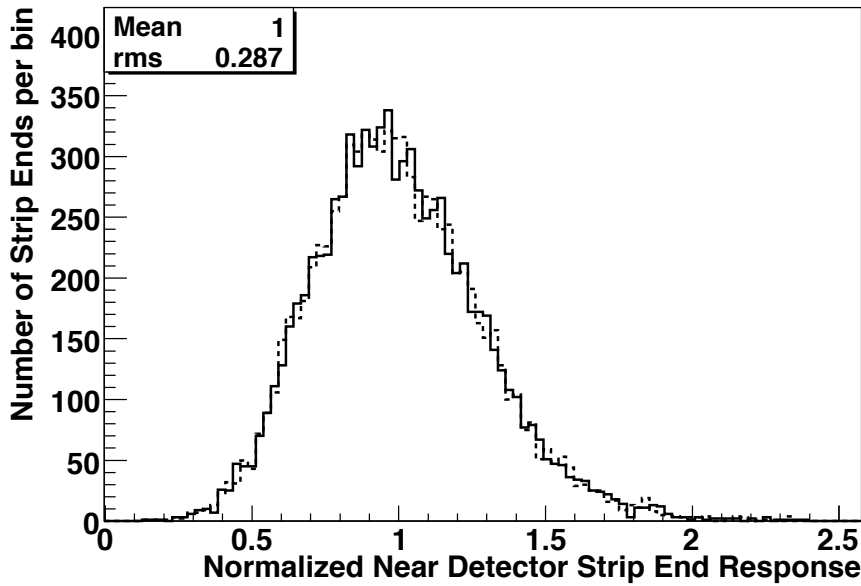
Fig. 35. Mean value of the strip-end responses normalized to the detector average. The mean response of the strip ends varies by approximately 29%. The solid and dashed lines are the calculated responses of two separate data sets from June 2005. The statistical variation in the individual calibration constants from these two data sets is on the order of 2.1%.

longitudinal track position (as measured by the orthogonal plane view). Figure 36 shows an example of a double exponential fit from module mapper data (Sec. 3.8.1), compared with cosmic ray muon data curve for one of the strips.

These studies show that in the near detector, the difference between the cosmic ray muon data and the fit curve of the mapper data is about 4%. Thus the muon measurements are consistent with the test-stand data. However, since fits to the mapper measurements were sensitive to fine granularity variations, they are the primary source of data for the far detector attenuation correction, while the high cosmic ray statistics available at the shallow near detector allow the use of muon data for the attenuation fits.

5.2.4 Timing calibration

A timing calibration has been performed for the far detector [27]. Although the readout electronics are found to be stable to within 1 ns, the detector readout as a whole is synchronized only to within 30 ns due to differing cable lengths and channel-to-channel electronics variations. The timing system is calibrated by measuring the size of the time offsets between readout channels with through-going cosmic ray muons. The calibration also tracks shifts in these offsets over time, which are largely due to hardware replacements in the detector readout.
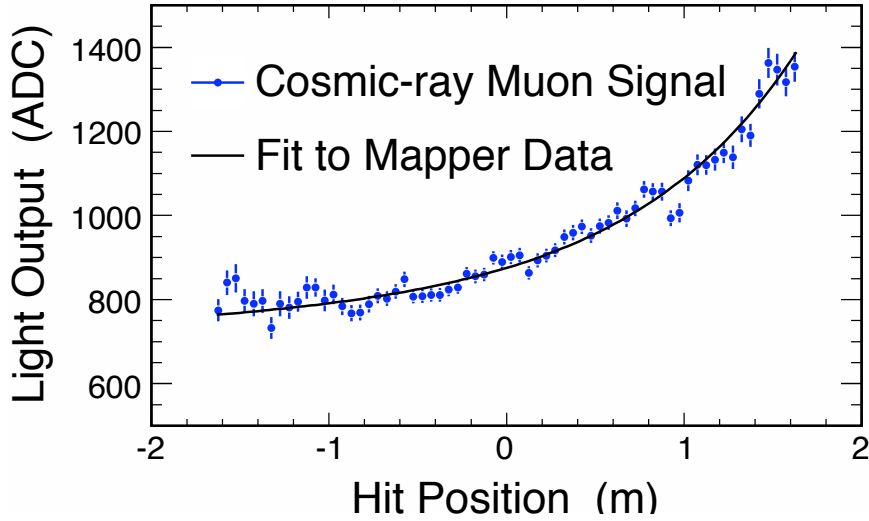
Fig. 36. Comparison of cosmic ray muon data (points) with module mapper fitting results (solid curve) for a typical strip in the near detector.

The times and positions of the reconstructed hits on each track are compared and a linear timing fit is applied, assuming that the muons travel at the speed of light. The mean offset between the measured and fitted times is calculated for each strip end. These offsets are then tuned using an iterative procedure to obtain the final calibration constants. The measured times must be corrected to account for shifts in the timing system caused by changes in readout components. Since the far detector readout is double-ended, the size of these shifts can be calculated from the corresponding shifts in the relative times of muon hits recorded at opposite strip ends.

This calibration is performed independently for each side of the far detector. The accuracy of the calibration is then calculated from the relative times of muon hits on opposite sides of the detector. Figure 37 shows the distribution of the mean time difference between opposite strip ends for each strip in the detector. The data have been divided into eight sub-samples to account for any long-term drift in the timing system. A Gaussian fit to this distribution gives an rms of $0.40\,\text{ns}$. The mean timing calibration error for a single strip end is therefore estimated to be: $\sigma = 0.40\,\text{ns}/\sqrt{2} = 0.28\,\text{ns}$.

5.3 Energy calibration

5.3.1 Absolute calibration

MINOS physics analyses require a good understanding of the detectors' response to muons, electrons and hadrons with energies below $10\,\text{GeV}$. The detector response
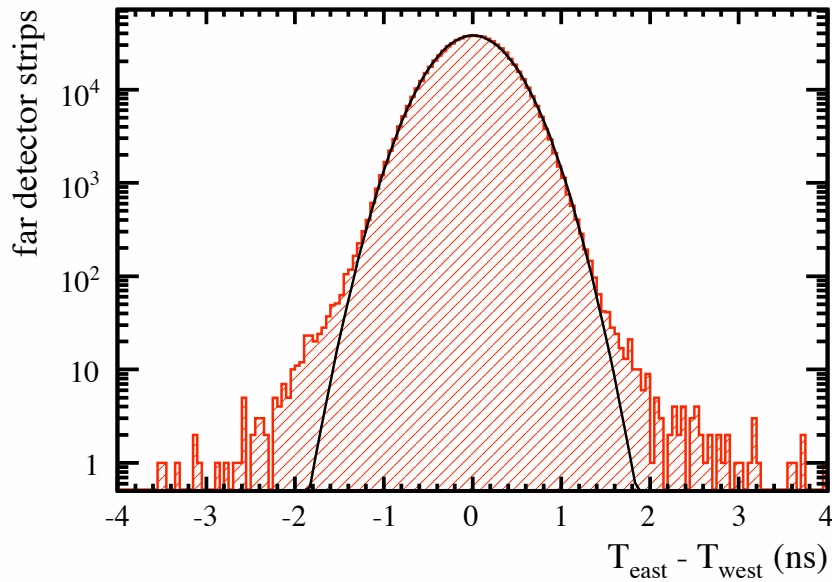
Fig. 37. Distribution of mean time differences between muon hits recorded at opposite ends of each of the 92,928 strips in the far detector. The data are represented by the hatched histogram. A Gaussian fit with a width of $\sigma = 0.4$ ns is also shown.

includes event shape characteristics in addition to the overall energy scale and resolution. The calibration detector [5] was exposed to test beams at CERN to establish the response to hadrons, electrons and muons with momenta in the range 0.2–10 GeV/c. The measurements were used to normalize Monte Carlo simulations and to establish the uncertainty on the hadronic and electromagnetic energy scales.

The calibration detector data were corrected to remove systematic effects at a level of 2% or better. Data were collected at fixed beam momentum settings of both positive and negative polarities, starting at 200 MeV/c and proceeding in 200 MeV/c steps up to 3.6 GeV/c and 1 GeV/c steps from 4 GeV/c to 10 GeV/c. Time-of-flight and threshold Čerenkov detectors were used to identify electrons, pions or muons, and protons. Muon/pion separation was accomplished by considering the event topology. Data were collected in two distinct beamlines, and several momentum settings were repeated multiple times to establish a run-to-run stability of better than 1%. Details are given in Ref. [5].

The data from the calibration detector were compared with events simulated using the same GEANT3 [47] based Monte Carlo used for the near and far detectors. Beam optics were modeled with the TURTLE [48,49] code. Upstream energy loss and particle decays were modeled with a standalone GEANT3 program. The range of stopping muons ($p <2.2$ GeV/c) was modeled to better than 3%, thereby benchmarking the combined accuracy of the muon energy loss treatment, beam simulation and absolute scale of the beam momentum. Figure 38 shows the measured detector response to pions and electrons compared with the simulation result.
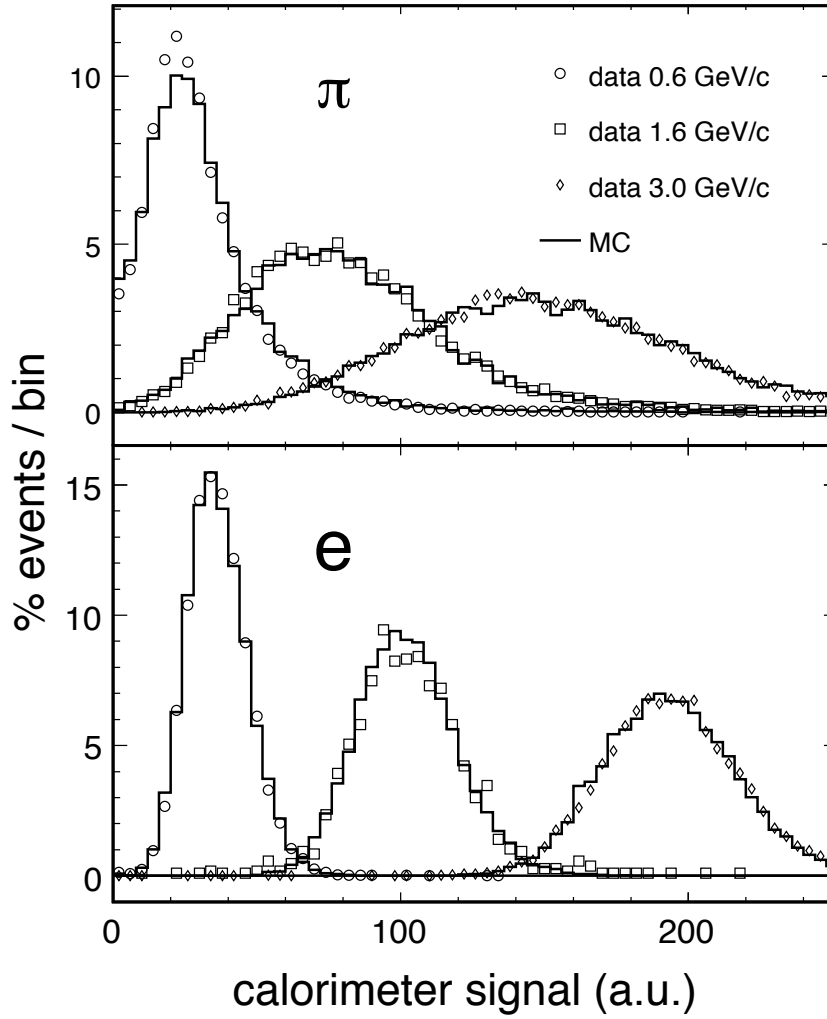
Fig. 38. MINOS calorimetric response to pions and electrons at three momenta. The calorimeter-signal scale is in arbitrary units. The data (open symbols), obtained from the calibration detector exposure to CERN test beams, are compared to distributions from Monte Carlo simulations.

The simulated detector response to electrons agreed with the data to better than 2% [50]. Pion and proton induced showers were compared with events simulated using the GHEISHA, GEANT-FLUKA [51] and GCALOR [52] shower codes. The GCALOR-based simulation was in best agreement with the data and was adopted as the default shower code. The Monte Carlo reproduces the response to pion and proton induced showers to better than 6% at all momentum settings [53]. The energy resolution was adequately reproduced by the simulation and may be parametrized as $56\%/\sqrt{E} \oplus 2\%$ for hadron showers and $21.4\%/\sqrt{E} \oplus 4\%/E$ for electrons, where E is expressed in GeV.

5.3.2 Inter-detector calibration

The 6% accuracy of the calibration detector hadronic energy measurement approaches the experiment's design goal of establishing the absolute energy scale to within 5%. The purpose of this section is to describe the transfer of this absolute energy scale calibration to the near and far detectors.

The calibration procedures outlined in Sections 5.1 and 5.2 are designed to produce temporally and spatially uniform detector responses. A relative calibration is then necessary to normalize the energy scales at the near, far and calibration detectors to be the same to within the 2% goal. Stopping muons are used for this task because they are abundant enough at all detectors and their energy depositions in each plane can be accurately determined from range measurements.

The energy loss of a muon by ionization is described by the Bethe-Bloch equation, which determines changes with muon momentum as shown in Fig. 39. To measure the responses of the detectors it is necessary to know the momentum of the muons used in the calibration. The momentum-range relations provide the simplest and most accurate technique to determine the momentum of stopping muons, with momentum from muon curvature in the detectors' magnetic fields serving as a secondary measurement (see Sec. 2.4.1).
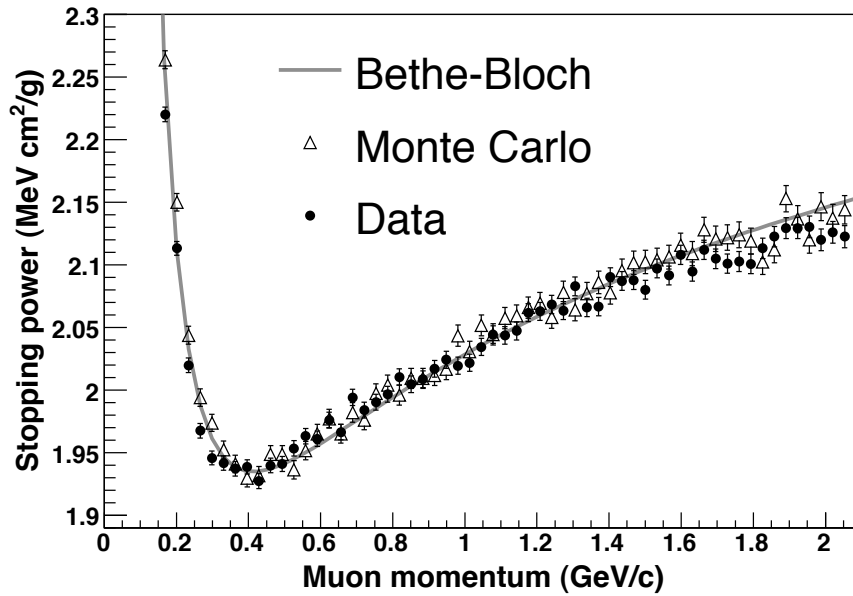

Fig. 39. Stopping power for muons. The gray line shows the Bethe-Bloch calculation of the stopping power for muons in polystyrene scintillator. The solid circles and open triangles show the response of stopping muons in the far detector data and GEANT3 Monte Carlo simulations respectively. Both data and Monte Carlo points have been normalized to the Bethe-Bloch calculation to give the expected stopping power at the minimum ionizing point.

To improve the accuracy of the inter-detector calibration, a "track window technique" [44] was developed. The technique hinges upon the particular way in which energy loss varies with momentum for muons. The dE/dx of a 1.5 GeV/c muon increases by approximately 100% in the last 10% of its range, whereas in the other 90% of its track the dE/dx changes by about 8%. The track-window technique measures the response of muons only when their momenta are between 0.5 and 1.1 GeV. This avoids using data from the end of the track where the rapid increase in ionization occurs, as shown in Fig. 39. Since the dE/dx varies so slowly in the 0.5–1.1 GeV region, a 2% error on knowing where the muon stopped gives an error of approximately 0.2% in the energy deposition.

The calorimetric responses of the three detectors, quantified as $1/M(d)$ in Eq. 1 in Sec. 5 above, are determined by the track-window technique and used to normalize the detectors' energy scales to within the 2% target, thus performing the inter-detector calibration.

The transfer of the absolute hadronic energy-scale to the near and far detectors is dominated by the 6% accuracy of the calibration detector measurement. There are smaller, detector-specific uncertainties such as the scintillator response uncertainties of 0.9% for the far detector, 1.7% for the near detector and 1.4% for the calibration detector [44] (already included in the 6% energy scale accuracy) and contributions from steel thickness variations at the ∼1% level. After adding all these uncertainty components in quadrature, the uncertainty in the absolute energy scale of each detector is determined to be approximately 6%.

5.3.3 *Comparison of near and far detector electronics response*

The above procedure normalizes the responses of the detectors for the energy deposition of a minimum ionizing particle. The test beam study of calibration detector response was used to verify that there are no energy-dependent differences introduced by the use of different types of multi-anode PMTs and electronics in the near and far detectors [54].

A series of special runs was taken with the calibration detector in which one end of each strip was read out with near detector PMTs and electronics while the other end was read out with far detector PMTs and electronics [55]. Figure 40 shows the relative response asymmetry in a strip

$$A_{N/F} = \frac{N - F}{0.5(N + F)},$$

(5)

measured with positrons between 0.5 and 6 GeV. This study shows that $A_{N/F}$ is close to 0 at an average energy deposition of around 1 MIP. Energy-dependent differences of up to 2% in the relative calibration of the readout systems are introduced

by the different nonlinearities and thresholds of the two systems. However, these are well modeled by the MC simulation that provide energy corrections for physics analyses. Subsequent data were taken with the far detector electronics removed from that side of the fibers and replaced with reflector connectors, to evaluate the effect of the single-ended readout of mirrored fibers in the near detector (Fig.17). These data were in agreement with the FD electronics data after the resulting calibration factors were applied.
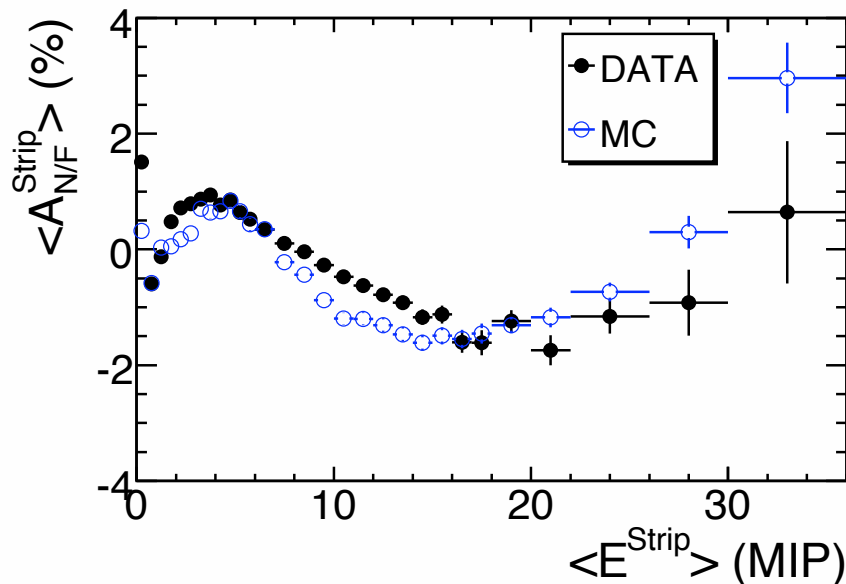

Fig. 40. Near-to-far asymmetry, Eq. 5, in the relative energy response as a function of the deposited energy, before linearity correction.

6 Detector Laboratory Facilities and Installation

This section describes the underground facilities constructed to house the near and far detectors (Sec. 6.1 and 6.3), and the installation procedures used to assemble the detectors (Sec. 6.2 and 6.4). The far detector is located underground in order to reduce counting rates due to low energy cosmic rays. The underground location of the near detector resulted from the $3.3°$ dip angle of the NuMI beamline. Detector installation was somewhat challenging because components had to be moved into the underground halls through restricted access shafts and assembled in relatively tight quarters. Sections 6.5 and 6.6 describe the survey procedures used to align the detector planes and to determine the precise direction in which the neutrino beam should be aimed.

The near detector hall is located at the Fermi National Accelerator Laboratory, 105 m below the surface. The near detector is 1040 m from the primary target and 330 m from the hadron absorber at the end of the decay pipe. The neutrino beam exits the rock 40 m upstream of the first detector plane. Underground construction of the near detector hall, including the detector support structure, was completed in March 2004.

The MINOS Service Building (MSB) is the primary entry point to the underground complex for material, personnel, and services. A 6.7 m diameter vertical shaft connecting the MSB to the underground complex is divided into two sections, one containing two elevators for personnel and the other housing conduits for electrical power, computer networks, ventilation ducts, pipes for the removal of ground water, and a hole large enough to lower complete MINOS near detector planes into the experimental hall. A 13.6 ton capacity overhead crane with a 5.6 m hook height is used to move equipment up and down this section of the shaft. Parts of the MSB roof can be removed to allow over-sized objects, such as the near detector magnet coil components, to be maneuvered into and out of the shaft.

Two transformers provide electrical service to the downstream portions of the complex, the detector and absorber halls. In addition to 1500 kVA of general-purpose electrical power, 750 kVA of "quiet" power is provided for noise-sensitive uses, such as the near detector front-end electronics.

The underground complex is ventilated with air forced into it at the base of the shaft and expelled at the hadron absorber hall and the downstream end of the detector hall. An air temperature of $24\pm1°$ C and dew point of $\leq13°$ C are maintained in the near detector hall at all times.

Ground water is collected from the entire underground tunnel system and pumped to the surface through the MSB shaft. The average collection rate, which has decreased slowly since construction was completed, was 650 liters per minute in 2006. Several backup pumps with independent electrical power are used to achieve a high level of reliability. Before being discharged to surface ponds, a portion of the cool ground water is directed into primary circulation loops for air conditioning, beam absorber cooling, and heat exchanging with a secondary low conductivity water loop (LCW) for near detector electronics and magnet power supply systems.

The LCW loop removes most of the heat generated in the magnet power supply (4 kW), the magnet coil (47 kW), and the front-end electronics racks (60 kW). A Proportional Integral Derivative (PID) controller sets the fraction of primary cooling water bypassing a heat exchanger in order to maintain the LCW output temperature at 21.1° C. Temperatures measured in the electronics racks are stable to better than 0.1° C in steady-state operation.

The access shaft to the underground detector hall at Fermilab is large enough to accommodate the near detector planes and their transport fixture, eliminating the need to construct planes during the underground detector assembly process. The near detector plane assembly process consisted of attaching scintillation modules and alignment fixtures to the steel planes. This was performed in the New Muon Lab at Fermilab while the underground detector hall was still under construction. The steel planes were inspected for flatness and sorted into stacks. A plane thickness profile was measured and recorded using an ultrasound system for the planes in the target and calorimeter sections, where detailed knowledge of the mass of the detector was desired (Sec. 2.2.4). Scintillation module maps (Sec. 3.8.1) were used to select the best modules for use on the target and calorimeter section planes.

Planes were assembled flat on the floor of the New Muon Lab, supported on the transport fixture. After assembly they were lifted and stored vertically on "hanging file" support structures until needed for final construction of the near detector in the underground hall. The scintillator modules were positioned on each plane using a template with reference to the magnet-coil hole and were attached to the plane by spot welded steel clips. The modules were checked for light tightness immediately prior to attachment. Small gaps between scintillation modules caused by uneven module edges were measured and recorded. Alignment fixtures for use during installation were tack-welded to each plane. The assembled planes were hung for storage in the order they would be retrieved for underground installation.

The near detector electronics racks are positioned to the west of the detector on two levels (Fig. 2) to accommodate U and V readout (Fig. 12). Fiber-optic readout cables from the scintillation modules enter the rear (detector side) of the "front-end" electronics racks, connecting to the phototube boxes. Inside the racks, cables connect the phototube bases to the digitizing electronics described in Sec. 4.2. On the front of the racks, cables carry digitized signals to the data acquisition system, housed in "master" racks (described in Sec. 4.2).

Installation of the detector planes began in April 2004 with the furthest downstream plane (number 281) and was completed five months later with the installation of plane 0 (a blank steel plane to cover plane 1 and necessary to match the far detector's beam-view ordering of steel-air-scintillator). Single planes were transported horizontally from the New Muon Lab to the MINOS Service Building on a flatbed truck, already attached to the transport fixture to minimize flexing of the plane. The plane was lowered vertically down the access shaft (still attached to the transport fixture), then transferred to a similar fixture located on a large steel frame cart. The cart was pulled about 80 m from the base of the shaft into the near detector hall where an overhead crane removed the plane from the cart and placed it into position on the detector support structure using the transfer fixture. The plane was then

bolted into place at the corners and at the coil hole collar fixture. A spacing alignment fixture was used to ensure uniform plane-to-plane distance (Sec. 2.2). A crew of physicists immediately inspected and tested each plane for light tightness and installed optical readout and light-injection cables. Alignment fiducials, located on the scintillation modules and on the steel plane and coil collar, were measured and recorded using the Vulcan system [12] (Sec. 6.6).

6.3 Far detector laboratory

The far detector laboratory is located 710 m (2070 meters-water-equivalent) below the surface, 735 km from Fermilab, in Soudan, Minnesota. The facility provides the electrical power, communications, fresh air and temperature control required to operate the detector. Power is supplied by a 450 kVA substation drawing from a 2400 kVA station on the surface. A fiber optics system provides high-speed DS3 (45 Mb/s) internet service to the underground laboratory.

The Soudan Mine is naturally ventilated, with a flow averaging approximately 130 l/s from the mine tunnels to the main shaft. About half of this flow is intercepted, before being exhausted up the shaft, and directed through the MINOS detector hall and the neighboring Soudan laboratory. The Cryogenic Dark Matter Search (CDMS II) experiment in the Soudan laboratory uses significant amounts of helium. As such, the hall air feeds are in parallel to prevent exposing any MINOS PMTs to this gas, which can penetrate the glass envelope and ruin the ultrahigh vacuum within.

An active cooling system removes heat from the laboratory generated by lighting, electronics and the detector magnet. A 3-stage chilled water loop provides cooling for both the magnet coil system and the laboratory as a whole. It includes both a conventional compressor-driven air-conditioning system (for the summer) and a simple fan-coil system (for winter) on the surface and provides a flow of $13°\,$C water to both systems.

6.4 Far detector installation

Installation of the MINOS far detector at Soudan began in July 2001 and continued through September 2003. A total of 486 planes (484 instrumented) were installed, tested, and integrated into the detector during this two year period.

6.4.1 Logistics

The logistics of bringing equipment, personnel and materials to build the MINOS detector to the underground detector hall at Soudan presented a significant challenge. It was especially important to mesh the delivery schedules of the steel and the scintillator modules, as these materials comprise the bulk of the detector and presented most stringent demands for storage and handling. Generally, about 55 planes worth of these materials could be stored in a facility on the surface at Soudan. Everything going into the Soudan Underground Laboratory must be transported down a relatively small shaft dating to the days of iron mining. Equipment and personnel are transported in cages that run on rails down the mine shaft, which is inclined by 12° with respect to the vertical. The length of objects that can be moved underground is limited by the size of the cages and by the dimensions of the shaft stations on the surface and underground. The shaft size limits transverse dimensions to slightly over 2 m, while the lift capacity of the hoist system limits cage loads to no more than 5.5 metric tons.

Steel was lowered in bundles of four plates. Each bundle was 8 m long and contained all the pieces for either a top or bottom layer of a double layer single plane. Upon reaching the shaft bottom, the steel bundle was transferred to a monorail for transport to storage racks adjacent to the plane assembly area. The scintillator modules, still housed in their 9 m long shipping crates (the length limit of the hoist system), were transported down the shaft in a manner similar to the steel. Once underground the crates were transferred to specially-designed carts and moved to a storage area near the module mapping table. In total, the detector comprises 5,400 metric tons of steel and 4,040 scintillator modules.

6.4.2 Scintillator module tests

Although the modules were tested and mapped with a radioactive source at the factory, additional tests were done at Soudan to ensure that they had incurred no damage in shipping, e.g. light leaks or broken fibers. The modules were found to be very robust. In the initial stages of detector construction, all modules were tested for light leaks and re-mapped (Sec. 3.8.1) at Soudan. As very few modules showed any significant change in response from their factory mapping, eventually shipments were checked by re-mapping only a few randomly-selected modules. An exception to this shortened testing occurred when there was reason to believe that damage may have been incurred. Before being installed on a plane, each module was checked for light tightness and repaired in the rare event of light leaks being found.

6.4.3 Steel plane assembly

Each plane was constructed on a strongback, in two layers of four plates each as described in Sec. 2.2.2. The assembly crew cleaned and de-burred each plate to minimize gaps between steel layers. During assembly of a plane it was important to ensure proper alignment of the top and bottom layers, especially on the support ears and in the central hole through which the coil passes. Any protrusions were ground away. As the steel plane was being assembled, the cable support brackets were affixed with a stud gun and the spacers and survey targets were welded into place.

6.4.4 Magnetic induction cables

Magnetic induction cables for the calibration (Sec. 2.4.1) were installed on each steel plane. Each plane had at least one 50-turn cable wrapped around the steel through the central hole to be connected to the calibration system. During plane construction, only the cables were attached; the circuit boards were connected after the plane was erected. The upper portion of the cable was laid out prior to the attachment of the scintillator modules. The lower side of the plane was inaccessible while on the strongback, so this side was uncoiled by a worker in a man-lift after the plane was erected. Six cables were installed on every twenty-fifth plane, as well as the first ten and last ten planes of each supermodule.

6.4.5 Scintillator mounting and cabling

The alternating U-V alignment of the scintillator planes stipulated that each of the two workstations build only planes of one orientation, completing planes in alternation. Because of minor differences in the configuration of the inner scintillator modules, a pre-sorted storage box of modules for the appropriate type of plane was brought adjacent to the strongback. There the modules were unloaded using a gantry crane with a vacuum lifting fixture. The scintillator layer for each plane was built from the center outward, i. e., beginning with the bypass modules straddling the coil hole and working toward the edges. As each module was positioned its retaining clips were welded into place.

After all of the modules of a plane were installed, the crew checked for gaps between them and recorded any that were found. They then connected the optical cables for scintillator readout (described in Sec. 3.6) and the optical fibers that supplied the light injection calibration pulses (Sec. 5.1). All cables were checked for correct length, orientation, light tightness and light transmission before being coiled for the transport of the plane to the detector.

6.4.6 Plane installation and survey

After a plane was assembled and tested it was ready to be rigged for lifting and transport to the detector support rails. The strongback clamps were engaged and a spreader bar attached to the strongback. For safety, the assembly area and the area through which the plane would travel were cleared of all personnel. The plane and strongback were lifted with an overhead bridge crane and transported to the face of the detector. There the crew positioned it and balanced the strongback with lead bricks to ensure that both ears sat down on the rails at the same time. Although a set of steel spacers was welded to the ears of the plane, it was important to avoid jolting the scintillator face into the detector as the plane was eased into position. Once the plane was resting on the rails, 6 of the 8 axial rod bolts were installed and the plane was shimmed if necessary. Then the strongback was released and returned to the assembly area. With the strongback out of the way, the crew used a man-lift to install the remaining axial bolts, unroll and affix the "bottom-side" magnetic induction cable, install the collar, and survey the installation (Sec. 6.6).

6.4.7 Optical connections and testing

Cabling for the newly-installed plane included connecting the readout cables to the MUX boxes (Sec. 3.5.2), routing the light-injection fibers to their distribution box, and connecting the circuit board(s) to the magnetic induction cable(s). The electronics installation proceeded in phase with the plane installation. This timely commissioning led to cosmic-ray data being routinely used for plane diagnostic purposes within a few days of plane installation. In no case was a scintillator module damaged during installation, although occasional light leaks were found and repaired. All 92,928 WLS fibers in the completed detector are in operation, although a very small number have only single-ended readout.

6.5 Far detector location

The success of the MINOS experiment depends on the accurate aiming of the neutrino beam at the far detector. The origin of the detector coordinate system is the upstream edge of the far detector. This lies 15.631 m upstream from the midpoint between the detector's two supermodules. That midpoint was surveyed and determined to be located at latitude 47.820267 degrees north, longitude 92.241412 degrees west, and ellipsoid height -248.4 m in North American Datum 1983 (NAD 83). This survey point is 705 m below the surface and 735.3380 km from the upstream end of the first horn of the neutrino beamline, which is very close to the (variable) target longitudinal position. The physics of the MINOS experiment requires that the transverse position of the neutrino beam center at the far detector be known to within 100 m. Over a dozen possible misalignments of neutrino beam elements

(e.g., target, focusing horns, decay pipe) must be contained within this tolerance, including the transverse position of the far detector relative to the line of sight from Fermilab. The alignment goal of 12 m was established for this portion of the total tolerance; most of this tolerance window comes from the uncertainty in specifying the angles of the neutrino beam leaving Fermilab.

The relative positions of Fermilab and Soudan on the surface are determined by making simultaneous measurements using the GPS satellites. Simultaneous GPS data at both Fermilab and Soudan were recorded for a total of 26 hours in April 1999. These data plus data from several Continuously Observed Reference Station (CORS) positions were analyzed by Fermilab personnel and independently by the National Geodetic Survey (NGS) [56,57]. The agreement between the NGS result and two methods of analysis at Fermilab was excellent. The Fermilab to Soudan vector, averaged over the period of the observations used, is known to better than 1 cm horizontally and 6 cm vertically at 95% confidence level, well within requirements. The differential earth tide effect between Fermilab and Soudan is approximately the same as this uncertainty.

The position of the far detector on the 27th level at the bottom of the Soudan Mine, relative to the surface, was determined using inertial survey by the University of Calgary in April 1999. The inertial survey unit used (Honeywell Laseref III IMU) contains a triad of accelerometers and optical gyroscopes to measure force and angular velocity. The accelerometers are double-integrated to yield position change along each of the three axes [58]. Independent calibration measurements with the inertial survey unit and the internal consistency of several inertial survey runs indicated a precision of 0.7 m per coordinate for the surface to bottom of the mine measurement, only a small part of the 12 m goal. Interestingly, these measurements agreed to better than 4 m per coordinate with the miners' 1962 (and thought to be less precise) values for the 27th level relative to the surface.

A partial check of the critical beam angles at Fermilab was made during commissioning before the target was installed [59]. The proton beam was sent 723 m past the target position and measured to be within 0.02 m transverse of the specified beam axis at the downstream end of the decay pipe. This check depends on optical survey measurements. At 735.3379 km, this beam line would then be within 20 m transverse of the far detector, confirming that the beam pointing was within a factor of two of the desired precision of 12 m and considerably less than the 100 m requirement.

The far detector and cavern axes are level and at an azimuth of 333.4452° (26.5548° west of true north). These angles were measured with optical levels (better than 5 microradian accuracy) and a gyro-theodolite (15 microradians accuracy). The latter is a precision theodolite combined with an accurate gyrocompass. The neutrino beam axis at the far detector is at an azimuth of 333.2870° and is sloped up at an angle of 3.2765° above the horizontal as the beam travels approximately NNW.

The large size of the far detector planes and the potential for mechanical instability made its survey particularly important. The alignment of the collars on every plane was also essential to allow the insertion of the magnet coil sleeve, a copper tube which passes through 249 (237) planes in the first (second) supermodule. The measurements on each plane had to be made quickly so as not to delay installation of the next plane. Furthermore, the retention of a professional survey crew in the Soudan underground mine would have been cost-prohibitive. These criteria motivated the selection of the Vulcan Spatial Measurement System [12], which was capable of millimeter-level precision. The system allowed an experienced technician to survey an entire plane within 30 minutes and could be operated effectively with only a few hours training. Under these field conditions, the Vulcan system achieved a spatial measurement accuracy of about 3 mm.

During construction, after every plane was installed but before the installation of the next plane, Vulcan measurements were made on its eight axial bolts and eight collar bolts. In addition, on every fifth plane, similar survey measurements were made on the eight steel lugs welded to points on the perimeter of the plane. These lugs are visible after the erection of subsequent planes. These measurements helped to prevent "creeping" of the detector plane positions and also established the average plane-to-plane pitch of 5.95 cm with a standard deviation of 0.35 cm.

The scintillator modules were also surveyed, using built in alignment pins as reference points. The Vulcan measurements for scintillator modules over the full supermodule showed that, to within the resolution of the Vulcan, the modules were aligned with each other and with the true U and V axes within approximately 1 mrad. This translates to a deviation of the end of the module from the true axis of 2–3 mm, eliminating the need for software rotation corrections during event analysis.

The far detector coil comprises loops of cable running through a copper sleeve inserted through a series of circular collars, so any rotation of the collar from plane to plane does not matter. The near detector, however, employs an aluminum coil comprising rectangular "planks," which are inserted through a series of square collars. The square shape of the near detector collars places limits not only on the allowable plane-to-plane translation of the collar, but on the rotation as well. While the Vulcan was employed for measurements of scintillator modules and axial bolts, it did not have sufficient precision for the collar alignment. For this task, a team of Fermilab surveyors set up a laser tracker in the near detector hall. Final laser tracker measurements showed the transverse alignment of collars along the entire length of the detector to be within 3 mm, which was sufficient for coil insertion.

The near detector plane spacing was set to the same 5.95 cm pitch as in the far de-

tector, using an alignment fixture that was attached to each plane during the installation process. Survey measurements during plane installation found the average plane-to-plane pitch to be 5.97 cm with a standard deviation of 0.37 cm.

Cosmic-ray muons were used to determine the precise alignment of the far detector scintillator modules along the U and V axes [60]. This was a one-dimensional software alignment procedure in which the positions of the U- and V-modules were adjusted along the V and U axes, respectively. At the underground location of the far detector, the cosmic-ray flux is insufficient to do a strip-by-strip alignment in a reasonable time. Instead, the relative strip positions are taken from the module mapper data (Sec. 3.8.1) and combined with the aligned module position to put the strip positions into the software geometry. A straight line is fitted to a muon track using all the hits except those in the module to be aligned. The difference between that module's hit position and the projected position from the fit is the residual. The alignment program then adjusts the position and proceeds to the next module in the track. After multiple iterations, the residuals are minimized and those positions are the accepted ones for the modules. The final far detector alignment fits had residuals of 0.75–0.85 mm. The near detector modules were aligned using a similar procedure, which resulted in residuals of approximately 0.3 mm for the modules and 1.0 mm for the strips [61].

7   Detector Operation and Performance

As the result of several years of routine data-taking, extensive operational experience has been obtained with the MINOS detector systems. Representative observations are presented here. Section 7.1 summarizes detector performance and reliability information. Section 7.2 describes the systems and procedures used to ensure data quality and to monitor detector system performance in real time. Finally, Sec. 7.3 gives an overview of the offline software used for detector performance measurements and data analysis.

Since the NuMI beam and near detector are located at Fermilab while the far detector is 735 km north in Soudan, MN, the coordination of experimental operations is non-trivial. This challenge has been addressed by making as much of the experiment as possible controllable remotely over computer networks. Physicist shift workers are present 24 hours/day, 7 days/week in the main MINOS control room on the 12th floor of Wilson Hall at Fermilab, where both near and far detectors are monitored and controlled. In addition, the NuMI beam is monitored by the MINOS shift workers but is controlled from the Fermilab accelerator control room. Weekdays between the hours of 7:30 and 17:30 US Central Time, four to five full-time technicians are present in the MINOS cavern of the Soudan Underground Laboratory, monitoring and controlling the far detector, and, as needed, repairing the detector subsystems. Both sites have technical support on call for after-hours in-

tervention when necessary. Close coordination among the three control rooms has provided high detector live times for periods when the beam is in operation (see Sec. 7.1.2).

7.1 Detector reliability and live-time fractions

7.1.1 Near detector

The near detector was commissioned in January 2005. Since then the detector has been kept in an operational state except during extended periods when the beam was not in operation. The near detector data taking is usually organized into an approximately 24 hour run sequence, consisting of 210 seconds of calibration runs followed by a 24 hour physics run. Excluding periods when the beam has been off, the fraction of time during which the near detector has been in physics data taking mode has averaged above 98.5%. Typically more than 99.95% of the detector channels are operational. The small fraction of the lost beam time is due to the daily calibration runs and infrequent detector maintenance.

Most downtime with beam on is due to maintenance, usually for the replacement of failed front-end electronics cards. A mean number of 3.5 cards (out of 9,360 total) failed per week before a mass replacement of unreliable on-board fuses was done in the summer of 2007. After that, the failure rate dropped to less than a board per week. The typical intervention to replace a few front-end cards requires approximately one hour of downtime, including the calibration of the replacement channels.

7.1.2 Far detector

The far detector installation was completed in July 2003 and the detector has been recording cosmic ray and atmospheric-neutrino data since then. By the time the beam arrived in the spring of 2005, reliable detector operation had become routine. Similar to near detector data taking, a 24 hour run sequence for physics data and calibrations is also the operational mode at the far detector. The overall live-time fraction in 2005 was 96.7% and has risen to the high 90%'s since. Typically all channels in the detector are functional, with isolated failures being fixed during beam downtime, usually within hours to days of the appearance of the problem.

After the neutrino beam turned on in March 2005 the important metric for evaluating experimental performance was the fraction of protons-on-target ("POT") while the far detector was taking good data. The MINOS experiment's sensitivity is driven by the statistics of neutrinos observed at the far detector, making it crucial to keep the far detector operating as much as possible. Since the end of beam commissioning in March 2005, the detector has run very smoothly, taking physics data for

>98.7% of all delivered NuMI protons for the first year's beam operations [4] and better than 99% thereafter.

7.2   Data quality and real-time monitoring

A combination of real-time monitoring and offline or post-processing monitoring is performed on a daily basis by physicists on shift to ensure data quality. The systems developed for these tasks keep track of similar parameters for both near and far detectors.

The MINOS Online Monitoring (OM) system is designed to provide real-time monitoring of data quality in the near and far detectors. It is based on the system used for the CDF experiment's Run II operations [62] and consists of three main processes. i) The *Producer* process receives raw data records from the DAQ via the MINOS Data Dispatcher, which are then processed to fill monitoring histograms. ii) The *Server* process receives monitoring histograms from the Producer, handles connections from external GUI processes, and serves histogram data to these processes on request. iii) The *GUI* process allows browsing and plotting of any of these monitoring histograms.

The monitor histograms are grouped into sections, e.g., those relating to digitized hits from the detector (channel occupancies, ADC distributions, etc.), singles rates, and distributions relating to electronics calibration and light injection data. A representative subset of these histograms is checked once every six hours by the shift crews at the detector sites and any problems are entered into the MINOS electronic logbook via a checklist template. All monitoring histograms are archived to tape for future reference.

The raw event data are moved to storage at Fermilab and copied over to the Farm Batch System for offline processing. From there the reconstruction is completed with a stable software release. Offline reconstruction is performed on data taken the previous day and used for the offline monitoring and subsequent data quality checks. The data are divided into separate streams in-time and out-of-time with the beam spills to facilitate monitoring as well as analysis.

The Offline Monitoring system serves two main purposes. It allows monitoring of the detector systems using reconstructed event data quantities such as event rates per POT, demultiplexing and scintillator strip efficiencies. Additionally the system provides the ability to verify that the offline production is proceeding normally so that unexpected changes can be tracked down quickly. The Offline Monitoring system has a histogram making process which runs once per day, reading in all the reconstructed data from the near and far detectors processed in the previous day and producing a set of histograms for monitoring. It also runs the *OMhistory* package, a process for viewing how these histograms change over time.

Other tasks performed during shifts include completing a checklist of the DCS systems described in Sec. 4.6, monitoring quasi-real-time event displays for both near and far detectors, and monitoring the NuMI beam performance [63]. These checks are performed during each shift to ensure that problems are noticed promptly and flagged for repair.

7.2.1 Near detector

In order to detect anomalies and trends in both the performance and data quality of the MINOS near detector, several quantities are verified weekly, including the total uncalibrated digitized response of the detector activity per POT during the $\sim 10\,\mu s$ spill as a function of time (Fig. 41a), the number of reconstructed events per POT as a function of time (Fig. 41b), and the reconstructed event time (Fig. 41c). Instabilities in these quantities may indicate a detector and/or reconstruction problem. The data used for these quantities come from the in-time spill stream, taking advantage of the large flux of beam neutrino events at the near site.
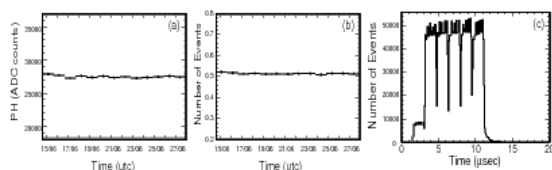
Fig. 41. Distributions examined in near detector data quality monitoring include: (a) the average spill pulse height, (b) the average number of reconstructed events per 1×10^{12} POT in a 13 day period, and (c) reconstructed event times in the $20\,\mu s$ gate.)

7.2.2 Far detector

The far detector data are checked weekly for anomalies in the reconstruction and data quality by comparing distributions of several reconstructed quantities to a baseline data set. Examples of distributions monitored are the number of planes crossed by muons in the detector (Fig. 42a), the incoming directions of the tracks and showers (Fig. 42b), and track entry locations (Fig. 42c). Other quantities that help ensure the detector calibration remains stable are the reconstructed velocity for cosmic ray muons for timing calibration and pulse heights of tracks and showers for energy calibration. Cosmic ray muons are most useful for these checks as they are the most abundant data source in the far detector.
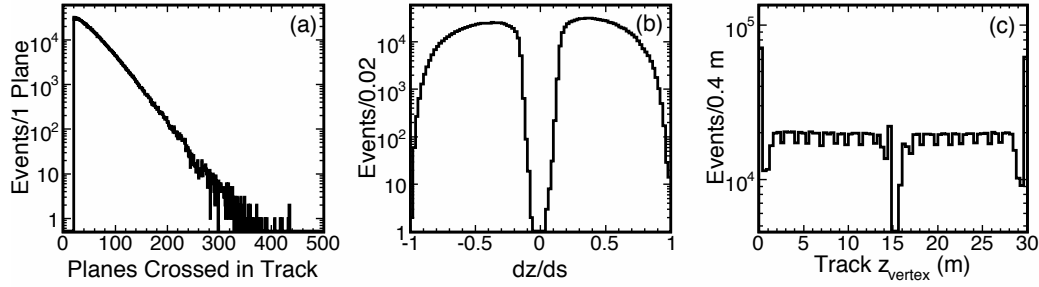
83

Fig. 42. Distributions examined during far detector data quality monitoring include: (a) the number of planes crossed by cosmic ray muon tracks, (b) the incoming direction of the cosmic ray muons with respect to the beam direction and (c) the entry location for cosmic ray muons along the length of the detector.

7.3 Offline software overview

Although MINOS comprises three detectors (the near, far and calibration detectors) at different depths and latitudes and with different sizes, physical configurations, beam characteristics and electronic readout schemes, the simplicity of the active detector technology has allowed a single framework of offline analysis software to be constructed for all detectors. The object oriented characteristics of the C++ language [64] have enabled the modularity required for this task. MINOS software is made available to collaborators using the Concurrent Versioning System (CVS) [21] embedded in the SLAC-Fermilab Software Release Tools (SRT) code management system [22]. The system uses software libraries from the CERN ROOT project [40], including ROOT tools for I/O, graphical display, analysis, geometric detector representation, database access and networking.

Raw data from different data acquisition processes at the MINOS detectors are written to disk as separate ROOT TTree "streams." These include physics event data, pulser calibration data, beam monitoring data and detector control data. This information immediately becomes available for monitoring, calibration and event display processes through an online data "dispatcher" service. This utility can access the online ROOT files while they are still open for writing by the MINOS DAQ systems. Subsequent offline processing produces additional TTree streams for event reconstruction results and analysis ntuples.

The need to correlate these streams of MINOS data with each other has motivated a key element in the MINOS software strategy called *VldContext* ("Validity Context"). VldContext is a C++ class that encapsulates information needed to locate a data record in time and space. Separate streams of data from different sources can be synchronized by comparing their VldContext objects. When MINOS offline

---

[21] http://www.nongnu.org/cvs/

[22] http://www.fnal.gov/docs/products/srt/

84

software opens files containing these streams, it indexes each stream according to the VldContext of each record. The indexing information can then be used to put VldContext-matched records into computer memory simultaneously. The GPS timestamps attached to raw data records enable this matching for far and near detector data in the same offline job. These features are illustrated in Fig. 43.

All MINOS record types derive from a common record base class with a header that derives from a common header base class. The minimum data content of the record header is the VldContext, used to associate records on input. The small record header is stored on a separate ROOT TTree Branch from the much larger data blocks. A MINOS stream is an ordered sequence of records stored in a ROOT TTree containing objects of a single record type extending over one or more sequential files. On input, records stored in different streams are associated with each other by VldContext and not by Tree index. The default mode is that records of a common VldContext form an input record set. Alternative input sequencing modes by VldContext are also supported.
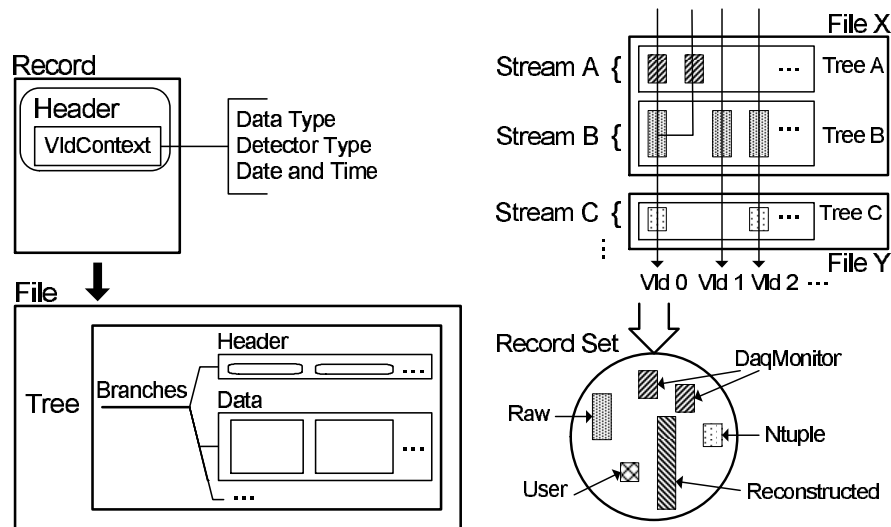

Fig. 43. MINOS data structure. The schematic on the left shows a MINOS record type derivation and header structure. The schematic on the right shows a MINOS stream as an ordered sequence of records stored in a ROOT TTree. On input, records stored in different streams are associated with each other by VldContext and not by Tree index.

The MINOS offline database contains calibration and survey data, including component locations and connection maps from the construction phase of the detector. These relational tables are keyed with a notion of "Validity Range" or scope of VldContext values to which a database record applies. For physics data of a particular VldContext, the offline database interface enables retrieval of matching database records whose Validity Ranges encompass the VldContext of the physics data in question.

The offline software accesses the offline database through a low-level ROOT [40]

85

interface, which allows data to be saved to and retrieved from compliant database products. The central database warehouse is served by MySQL [23] and is about 100 GB in size. Local distributed databases are in MySQL installations and can be substantially smaller depending on the local needs. Data in the distributed MySQL servers are automatically synchronized with the MySQL warehouse through a multiple-master replication scheme.

8 Conclusions

The MINOS far detector has been in continuous operation since July 2003 and the near detector has been operating since January 2005. Both detectors and their magnet coils routinely operate nearly 99% of the time when the neutrino beam is on, with close to 100% of their readout channels working properly.

Cosmic ray muons are used to calibrate the MINOS detectors, correcting for drifts over time, for variation of response over position within a detector, and for differences between detectors. The light injection system monitors the PMT nonlinearities and gains. Together, these calibration methods have established the relative near-far shower energy scale to 2%. The calibration detector test-beam measurements have established the shower energy scale to a precision of 6%. With units of E expressed in GeV, the measured calorimetric energy resolutions of $21.4\%/\sqrt{E} \oplus 4\%/E$ for electromagnetic showers and $56\%/\sqrt{E} \oplus 2\%$ for hadronic showers are in excellent agreement with predictions.

The far detector time resolution of 2.3 ns is sufficient to give useful time-of-flight information for cosmic-ray events, and allows a clean sample of upward-going muons (from atmospheric-neutrino interactions in the rock beneath the detector) to be identified. The near detector time resolution of approximately 5 ns provides a clean separation of neutrino events from different RF buckets within the same 8–10 μs Main Injector spill. The experiment routinely transmits spill-time information over the internet from Fermilab to Soudan, allowing a real-time spill gate to be applied (in the trigger software) to far detector neutrino beam data with an uncertainty of $< 1\,\mu$s.

As of early 2008, the far detector has measured neutrino oscillation parameters from atmospheric-neutrino events recorded during its first two years of data taking [25] and higher-energy upward-going muons [65] as charge-seperated samples. The experiment has also accumulated data from more than 4×10^{20} Main Injector protons on target, less than half of its total expected data sample, and has made its first measurements of Δm^2 and $\sin^2 2\theta$ [3,4]. Thus it has been demonstrated that the performance and calibrations of the near and far detectors provide a suitable

---

[23] http://www.mysql.com/

foundation for achieving the neutrino physics goals of the MINOS experiment.

Acknowledgments

References

[1] K. Anderson, et al., NuMI facility technical design report, Tech. Rep. FERMILAB-DESIGN-1998-01, Fermilab (1998).

[2] Y. Ashie, et al., A measurement of atmospheric neutrino oscillation parameters by Super-Kamiokande I, Phys. Rev. D71 (2005) 112005.

[3] D. G. Michael, et al., Observation of muon neutrino disappearance with the MINOS detectors and the NuMI neutrino beam, Phys. Rev. Lett. 97 (2006) 191801.

[4] P. Adamson, et al., A Study of Muon Neutrino Disappearance Using the Fermilab Main Injector Neutrino Beam, Phys. Rev. D77 (2008) 072002.

[5] P. Adamson, et al., The MINOS calibration detector, Nucl. Instrum. Meth. A566 (2006) 119–133.

[6] The MINOS Collaboration, P-875: A long baseline neutrino oscillation experiment at Fermilab, Tech. Rep. FERMILAB-PROPOSAL-0875, Fermilab (1996).

[7] The MINOS Collaboration, MINOS experiment R&D plan: FY 1996-1998, Tech. Rep. FERMILAB-TM-2414-E, Fermilab (1996).

[8] I. Ambats, et al., The MINOS detectors technical design report, Tech. Rep. FERMILAB-DESIGN-1998-02, Fermilab (1998).

[9] Y. Fukuda, et al., Atmospheric muon-neutrino / electron-neutrino ratio in the multigev energy range, Phys. Lett. B335 (1994) 237–245.

[10] Y. Fukuda, et al., Evidence for oscillation of atmospheric neutrinos, Phys. Rev. Lett. 81 (1998) 1562–1567.

[11] J. K. Nelson, The MINOS magnets, Int. J. Mod. Phys. A16S1C (2001) 1181–1184.

[12] V. Bocean, Status Report on the Geodetic and Alignment Efforts for the NuMI project at FermilabContributed to 8th International Workshop On Accelerator Alignment (IWAA 2004), Geneva, Switzerland, 4-7 Oct 2004.

[13] American Society for Testing and Materials (ASTM), General requirements for rolled structural steel bars, plates, shapes, sheet piling, ASTM A-6.

[14] J. Kilmer, J. Nelson, MINOS far detector coil design, Tech. Rep. FERMILAB-TM-2408-E, Fermilab (1999).

[15] J. Kilmer, J. Nelson, MINOS near detector coil design, Tech. Rep. FERMILAB-TM-2407-E, Fermilab (1999).

[16] ANSYS Inc., Engineering commercial software, Southpointe 275 Technology Drive, Canonsburg, PA 15317.

[17] R. Ospanov, A measurement of muon neutrino disappearance rate, Ph.D. thesis, University of Texas at Austin, Fermilab-Thesis-2008-04 (2008).

[18] A. Pla-Dalmau, et al., Extruded plastic scintillators for the MINOS calorimeters, Frascati Phys. Ser. 21 (2001) 513–522.

[19] P. Border, et al., A large liquid scintillator detector for a long baseline neutrino oscillation experiment, Nucl. Instrum. Meth. A463 (2001) 194–204.

[20] J.-C. Yun, A. Para, Scintillator reflective layer coextrusion, U.S. Patent 6,218,670 (2001).

[21] S. Avvakumov, et al., Spontaneous light emission from fibers in MINOS, Nucl. Instrum. Meth. A545 (2005) 145–155.

[22] N. Tagg, et al., Performance of Hamamatsu 64-anode photomultipliers for use with wavelength-shifting optical fibres, Nucl. Instrum. Meth. A539 (2005) 668–678.

[23] K. Lang, et al., Characterization of 1600 Hamamatsu 16-anode photomultipliers for the MINOS far detector, Nucl. Instrum. Meth. A545 (2005) 852–871.

[24] B. J. Rebel, Neutrino-induced muons in the MINOS far detector, Ph.D. thesis, Indiana University, Fermilab-Thesis-2004-33 (2004).

[25] P. Adamson, et al., First observations of separated atmospheric ν_μ and $\bar{\nu}_\mu$ events in the MINOS detector, Phys. Rev. D73 (2006) 072002.

[26] C. L. F. Howcroft, Atmospheric neutrinos in the MINOS far detector, Ph.D. thesis, University of Cambridge, Fermilab-Thesis-2004-71 (2004).

[27] A. S. T. Blake, A study of atmospheric neutrino oscillations in the MINOS far detector., Ph.D. thesis, University of Cambridge, Fermilab-Thesis-2005-77 (2005).

[28] G. Drake, et al., CDF Front End Electronics: The Rabbit System, Nucl. Instrum. Meth. A269 (1988) 68.

[29] G. Drake, T. F. Droege, J. Nelson, C. A., K. J. Turner, T. K. Ohska, The Rabbit System: Low Cost, High Reliability Front End Electronics Featuring 16-Bit Dynamic Range, IEEE Trans. Nucl. Sci. 33 (1986) 92–97.

[30] T. Cundiff, et al., The MINOS near detector front end electronics, IEEE Trans. Nucl. Sci. 53 (2006) 1347–1355.

[31] R. J. Yarema, G. W. Foster, J. Hoff, M. Sarraj, T. Zimmerman, A Fast, wide range charge integrator and encoder ASIC for photomultiplier tubes, IEEE Trans. Nucl. Sci. 40 (1993) 750–752.

[32] J. Oliver, N. Felt, G. Feldman, A. Lebedev, R. Lee, Design and performance of the readout system of the MINOS far detector, IEEE Trans. Nucl. Sci. 51 (2004) 2193–2195.

[33] Ideas ASA, PO Box 1, 1330 Fornebu, NORWAY.

[34] ASDLite is a prototype ASIC originally developed for the ATLAS muon chamber readout.

[35] Xilinx, 2100 Logic Drive, San Jose, CA 95124-3400, U.S.A.

[36] AD9240 from Analog Device Inc., http://www.analog.com/.

[37] GPS Timing Receiver XL-AK by Symetricon (formerly TrueTime), 3750 Westwind Blvd., Santa Rosa, CA 95403, U.S.A.).

[38] A. Belias, et al., The MINOS data acquisition system, IEEE Trans. Nucl. Sci. 51 (2004) 451–455.

[39] Creative Electronic Systems (CES) Corp., The PVIC and VIC Family Data Sheet, October 2004.

[40] R. Brun, F. Rademakers, Root: An object oriented data analysis framework, Nucl. Instrum. Meth. A389 (1997) 81–86.

[41] P. Adamson, et al., Measurement of neutrino velocity with the MINOS detectors and NuMI neutrino beam, Phys. Rev. D76 (2007) 072005.

[42] P. Adamson, et al., The MINOS light injection calibration system, Nucl. Instrum. Meth. A492 (2002) 325–343.

[43] P. Adamson, et al., On the linearity of the MINOS light-injection calibration system, Nucl. Instrum. Meth. A521 (2004) 361–366.

[44] J. J. Hartnell, Measurement of the calorimetric energy scale in MINOS, Ph.D. thesis, University of Oxford, Fermilab-Thesis-2005-51 (2005).

[45] C. B. Smith, Calibration of the MINOS detectors and extraction of neutrino oscillation parameters, Ph.D. thesis, University College London, Fermilab-Thesis-2002-58 (2002).

[46] P. A. Symes, Preliminary measurement of neutrino oscillation parameters by NuMI/MINOS and calibration studies for improving this measurement, Ph.D. thesis, University of Sussex, Fermilab-Thesis-2005-76 (2005).

[47] R. Brun, F. Carminati, GEANT detector description and simulation tool, CERN Programming Library Long Writeup W5013 (1993).

[48] D. C. Carey, K. L. Brown, F. C. Iselin, Decay TURTLE (Trace Unlimited Rays Through Lumped Elements): A computer program for simulating charged particle beam transport systems, including decay calculations, Tech. rep., SLAC, SLAC-0246 (1982).

[49] U. Rohrer, PSI Graphic Turtle Framework by U. Rohrer based on a CERN-SLAC-FERMILAB version by K.L. Brown et al. (2003).
URL http://people.web.psi.ch/rohrer_u/turtle.htm

[50] P. L. Vahle, Electromagnetic interactions in the MINOS detectors, Ph.D. thesis, University of Texas at Austin, Fermilab-Thesis-2004-35 (2004).

[51] A. Ferrari, P. R. Sala, A. Fasso, J. Ranft, FLUKA: A multi-particle transport code (program version 2005), CERN-2005-010, INFN/TC_05/11, SLAC-R-773.

[52] C. Zeitnitz, T. A. Gabriel, The GEANT - CALOR interface and benchmark calculations of ZEUS test calorimeters, Nucl. Instrum. Meth. A349 (1994) 106–111.

[53] M. A. Kordosky, Hadronic interactions in the MINOS detectors, Ph.D. thesis, University of Texas at Austin, Fermilab-Thesis-2004-34 (2004).

[54] A. Cabrera, et al., Test beam comparisons of the minos near and far detector readout systems, Nucl. Instrum. Meth. A (2008) to be published.

[55] A. Cabrera, Systematic comparison of the MINOS near and far detector readout systems, Ph.D. thesis, University of Oxford, Fermilab-Thesis-2005-50 (2005).

[56] V. Bocean, Geodetic determinations for the NuMI Project at FermilabPrepared for 6th International Workshop on Accelerator Alignment (IWAA 99), Grenoble, France, 18-21 Oct 1999.

[57] T. Soler, R. H. Foote, D. Hoyle, V. Bocean, Accurate GPS orientation of a long baseline for neutrino oscillation experiments at Fermilab, Geophysical Research Letters 27 (2000) 3921–3924.

[58] J. Skaloud, P. Schwarz, Application of inertial technology to underground positioning: the Soudan mine shaft survey, Zeitschrift für Vermessungswesen 125 (2000) 292–299.

[59] R. Zwaska, et al., Beam-based alignment of the NuMI target station components at FNAL, Nucl. Instrum. Meth. A568 (2006) 548–560.

[60] B. Becker, D. Boehnlein, Alignment of the MINOS far detector, Tech. Rep. FERMILAB-TM-2410-E, Fermilab (2004).

[61] R. Ospanov, K. Lang, Alignment of the near detector scintillator modules using cosmic ray muons, Tech. Rep. FERMILAB-TM-2411-E, Fermilab (2005).

[62] W. Wagner, et al., Online monitoring in the CDF II experiment, Prepared for International Europhysics Conference on High-Energy Physics (HEP 2001), Budapest, Hungary, 12-18 Jul 2001.

[63] S. Kopp, et al., Secondary beam monitors for the NuMI facility at FNAL, Nucl. Instrum. Meth. A568 (2006) 503–519.

[64] B. Stroustrup, The C++ Programming Language, 3rd Edition, Addison-Wesley, 1997.

[65] P. Adamson, et al., Charge-separated atmospheric neutrino-induced muons in the MINOS far detector, Phys. Rev. D75 (2007) 092003.